2016

# Frequency-domain method for measuring alpha factor by self-mixing interferometry

Zhenghao Liu
*University of Wollongong*, zl460@uowmail.edu.au

UNIVERSITY OF WOLLONGONG

# Frequency-domain method for measuring alpha factor by self-mixing interferometry

A thesis submitted in partial fulfilment of the requirements

for the award of the degree

**Master of Philosophy**

from

**UNIVERSITY OF WOLLONGONG**

by

**Zhenghao Liu**

School of Electrical, Computer and Telecommunications Engineering

March 2016

*Dedicated to my family*

# *Declaration*

This is to certify the work reported in this thesis was carried out by the author, unless specified otherwise, and that no part of it has been submitted in a thesis to any other university or similar institution.

Zhenghao Liu

March 2016

# *Abstract*

Linewidth enhancement factor, also known as the alpha factor, is a fundamental characteristic parameter of a laser diode (LD). It characterises the broadening of the laser linewidth, the frequency chirp, the injection lock range and the response to external optical feedback. In the past few decades, extensive researches have been dedicated to the measurement of alpha. Among all the existing approaches, the methods based on self-mixing interferometry (SMI) are considered the most simple and effective. The core components of a SMI consist of an LD, a lens and a moving target. When a portion of laser light backscattered or reflected by the external target and re-enters the laser cavity, a modulated lasing field will be generated. The modulated laser power is also called SMI signal, which carries the information of target movement and LD related parameters, including alpha.

The frequency-domain method is one of the SMI based alpha measurement techniques, which has the merits of high accuracy, feasible over a wide range of optical feedback level and low computational complexity. However, the measurement performance can be easily degraded by the noises contained in SMI signals. This thesis addresses such issue from two aspects: noise filtering and process optimization. A new filtering technique is proposed specially for eliminating the transient oscillation (which is treated as impulsive noise) and reducing white noise in SMI signals simultaneously. Then, by analysing the errors introduced at each stage of the frequency-domain based method, a series of optimization methods are proposed that can effectively prevent error propagation during the calculation.

Additionally, an FPGA based real-time alpha measurement system using the frequency-domain method is presented. Both simulation and experimental tests show the system works well for alpha measurement. The system developed in this thesis can be employed for the further in-depth study on the character of alpha factor.

# *Acronyms*

| | |
|---|---|
| **SMI** | self-mixing interferometry |
| **LD** | laser diode |
| **FPGA** | field-programmable gate array |
| **L-K** | Lang-Kobayashi |
| **MSE** | mean square error |
| **FFT** | fast Fourier transform |
| **SL** | semiconductor laser |
| **PD** | photodiode |
| **LC** | laser controller |
| **TC** | temperature controller |
| **PZT** | piezoelectric ceramic transducer |
| **SNR** | signal noise ratio |

# *Acknowledgement*

I would like to extend thanks to the many people who generously contributed to the work presented in this thesis.

First and foremost, I would like to express my sincere gratitude and respect to my supervisors, Associate Professor Yanguang Yu and Dr Qinghua Guo, for their encouragement and guidance. Without their instructive suggestions, patient instructions, insightful criticism and expert guidance, this thesis cannot reach its present form. Their academic attitude and enlightenment not only help me with this thesis but also in my future study and career.

Secondly, I feel grateful to all the staff in School of Electrical, Computer and Telecommunications Engineering (SECTE) and Information and Communication Technology Research (ICTR) Institute who have helped me to build up an academic ability.

Last but not least, my special gratitude goes to my beloved parents for their loving support. Without their loving consideration and great confidence in me, I would have not been able to accomplish this work.

# *Publications*

Much of the work in this thesis has been published or has been submitted for publication. These papers are:

1) **Z. Liu**, Y. Yu, Q. Guo, J. Xi, J. Tong, and S. Tong, "FPGA based design for real-time measurement of alpha," in *SPIE/COS Photonics Asia*, 2014, pp. 92670S-92670S-10.
2) **Z. Liu**, B. Liu, Y. Fan, Y. Yu, J. Xi, Q. Guo*, et al.*, "A novel normalization method for improving the sensing performance of a self-mixing interferometry," in *TENCON 2015-2015 IEEE Region 10 Conference*, 2015, pp. 1-4.
3) **Z. Liu**, Y. Yu, Y. Fan, J. Xi, Q. Guo, and J. Tong, "Eliminating influence of transient oscillations on a self-mixing interferometry," submitted to Optical Engineering.

During my master's studies, I also did some work on self-mixing interferometry based measurement on Young's modulus. This research does not appear in this thesis, but is in the following publication:

4) K. Lin, Y. Yu, **Z. Liu**, J. Xi, H. Li, and C. Liu, "System implementation of self-mixing interferometry technique-based measurement on Young's modulus," in *SPIE/COS Photonics Asia*, 2014, pp. 92760K-92760K-8.

**Table of contents**

**LIST OF FIGURES**

**LIST OF TABLES**

# Chapter 1. Introduction

## 1.1 Introduction to alpha factor

Laser linewidth is defined as the width of the power spectral density of the emitted electric field in terms of frequency, or more experimentally, the full-width half-maximum (FWHM) of the optical field power spectrum [1,2]. The linewidth is associated to the fluctuations in the phase of the optical field, which arise from two basic sources: spontaneous emission and carrier density fluctuations (unique to semiconductor).

To explain the observed linewidth broadening which is much greater than expected by conventional theories of laser linewidth, the concept of linewidth enhancement factor (also known as alpha factor, denoted as $\alpha$) was introduced by Henry [2]. He found that linewidth broadening results from the coupling between phase and intensity, which is caused by the change of refractive index with carrier density in the semiconductor [2]. Thus, $\alpha$ is introduced to quantify the amplitude-phase coupling mechanism, expressed as [2,3]:

$$\alpha = 2 \cdot \frac{\Delta\phi}{\Delta g} \tag{1.1}$$

where $\Delta\phi$ is the change in phase; the factor 2 converts the change of power gain $\Delta g$ to the change of amplitude gain. Meanwhile, in terms of the change in refractive index with carrier density, $\alpha$ also can be expressed as [2,3]:

$$\alpha = \frac{\Delta n_r}{\Delta n_i} = \frac{\partial n_r / \partial N}{\partial n_i / \partial N} \tag{1.2}$$

where $n_r$ and $n_i$ are the real and imaginary parts of reflective index $n$; $N$ is carrier density. This suggests a change in $\Delta n_r$ will result in phase shift and line broadening.

According to the derivation of Henry on the linewidth of a single-mode laser diode, the laser linewidth should be increased by a factor of (1+$\alpha^2$) [2], which has been confirmed to be in reasonable agreement with experimental data.

Since phase fluctuations lead to linewidth broadening as a consequence, the value of $\alpha$ is useful for analyses of any phenomena where variations of phase are important, which include the phase noise [4-7], field spectra [8-10] and FM noise [10-12]. Besides, $\alpha$ is also responsible for injection locking phenomena and the response to external optical feedback [13-16]. Considering the significant influence of $\alpha$ on these properties, it is of significant interest to understand this parameter and knowing its value. In the past few decades, researchers have devoted their efforts to exploring measuring techniques and improving measurement accuracy. In the following sections, various $\alpha$ measuring methods for laser diodes are reviewed.

## 1.2 Literature review on alpha measurement

As mentioned in the previous section, $\alpha$ has significant influence on several properties of laser diodes, such as spectral effects, modulation response, injection locking and the response to external optical feedback. In the past few decades, the connection between $\alpha$ and those effects has been investigated extensively, thereby different measurement techniques were developed accordingly. Generally, they are classified as: FM/AM method [17,18], optical injection method [19-21], optical feedback method [22-25] and linewidth measurement [2,26,27].

- **FM/AM method**

The FM/AM modulation method [17] is based on current modulation of a high frequency SL, which will in turn result in both amplitude modulation (AM) and frequency (FM) modulation in the laser. The ratio of the FM over AM components allows a direct measurement of the linewidth enhancement factor. The amplitude modulation term can be directly detected by means of a high speed photodiode, whereas the frequency modulation term is measured using a high resolution Fabry-Perot filter as it is related to laser sidebands intensity. This

method is based on the hypothesis that the susceptibility is linear and the carrier density is longitudinally uniform.

Based on the same principle as the FM/AM modulation, the FM/AM noise method [18] relies on the measurement of the phase correlation and the ratio between the spectral dependence of semiconductor laser FM noise and AM excess noise [18]. The AM noise can be measured by direct detection and RF spectrum analysis, while the FM noise is measured by Fabry-Perot filters or other techniques. All the FM and AM noises are measured in a frequency range where the spontaneous emission noise is dominant. This method requires complex experimental implementation, but is relaxed from active current modulation.

- **Optical injection method**

The principle of injection locking is that the injection of light from a master LD into a slave LD causes locking of the slave LD's lasing frequency to be that of the master's [19-21]. The locking region is typically characterized by the injection level and the asymmetrical frequency detuning, due to the non-zero $\alpha$ factor. This category of methods are based on the complex theory of injection locking dynamics, however, simplified analytical dependence of the measured the quantities such as asymmetric detuning range can be established on $\alpha$ factor. These techniques are of complicated experimental implementation, and the accuracy of measurement is dependent on the availability of knowledge about the injection level whose measurement is generally very difficult.

- **Optical feedback method**

There are generally two categories of optical feedback method for alpha measurement: one is retrieving alpha from self-mixing signals [23-25], which will be introduced in detail in Section 1.3; another is based on the functional relationship associated with alpha between the emission wavelength and effective reflectivity of laser compound cavity [22].

In [22], two simple alpha measuring methods are proposed, a current scanning method and a reflectivity scanning method, to measure alpha with an external cavity semiconductor laser

(SL). The functional relationship related to alpha between the emission wavelength and effective reflectivity of the compound cavity of the SL is the key to both of the two methods. Both of these two methods do not require modifying the laser configuration of traditional external cavity. The current scanning method uses the frequency tuning curve as a function of injection current to estimate the value of alpha. A simple model which yields a linear relationship between the injection current and the phase shift of the incident wave after one round trip in the external cavity is introduced in the first method. On the other hand, in the reflectivity scanning method, the external feedback intensity is scanned to control the effective reflectivity of SL which leads to the determination of the value of alpha. In this paper, the modification of the external feedback intensity is implemented by adjusting the rotation angle of a half wave plate inserted in the external cavity.

- **Linewidth measurement**

Although in [2,27], the approximate value of $\alpha$ was deduced from analysis of spontaneous emission in buried hetero-structure lasers by measuring the refractive index and gain change within the active layer. This approach relies on an accurate knowledge of the carrier concentration in the active layer, which is not easily determined due to the uncertainties in the layer thickness, lifetime etc.

In [26], Toffano et al. proposed an easier method for measuring the alpha factor based on linewidth measurements. The laser linewidth then injection current below and above threshold can be written as $\Delta v_b = R_{th}/2\pi P$ and $\Delta v_a = (1+\alpha^2)R_{th}/4\pi P$, where $R_{th}$ is the total spontaneous emission rate above threshold and $P$ is the photon number in the mode. Thus $\alpha$ can be obtained by comparing the laser linewidth below threshold to its value above threshold, i.e. $\alpha = \sqrt{2\Delta v_a/\Delta v_b - 1}$.

In summary, based on the methods reviewed above, a wide range of $\alpha$ values were obtained respect to different laser diode structures, different measuring techniques and different

operating conditions. In some early researches, $\alpha$ was studied and measured as a constant parameter for a certain type of semiconductor material used in LD, for instance the methods based on sub-threshold gain and refractive index measurements [27,28]. Later, as the dependence between $\alpha$ and other LD associated parameters were investigated [3,25,28-30], e.g. LD structure, system operating conditions, they provided explanations that how inconsistent values of $\alpha$ were obtained from the same type of LD. According to the existing researches, LD operating conditions including operating temperature, output power and optical feedback level have been found can affect the value of $\alpha$ [3,25,29,30]. Since $\alpha$ is no longer a constant parameter in operation based on this context, it is important to pay attention to the measuring condition before using the value of alpha for analysis or applications.

## 1.3 SMI based alpha measurement

Self-mixing interferometry (SMI) has been an active and promising technique for non-contact sensing, which is based on the self-mixing effect. The self-mixing interference happens when a part of laser light reflected or backscattered from a distant target ahead of the laser, re-enters the laser cavity, resulting in modulations on both intensity and frequency of the lasing field. The modulated laser power, called SMI signal, is detected by a photodiode (PD). The self-mixing interferometry inherently possesses the superiority of self-alignment, mechanical stability and exemption from necessitating costly high precision optical apparatus. Generally, there are two classes of applications based on SMI technique: one is external target related metrological quantities measurement; another is estimation of parameters associated with laser diode. External target (solid targets and fluids) related detections include displacement, vibration, velocity, etc. [31-33]. Measurements of LD parameters mainly focus on the alpha factor and the optical feedback strength [32].

The primary objective of this section is to introduce SMI system and the alpha measuring methods based on SMI system. Firstly, the fundamental concepts of the system are described, including system structure, theoretical model and the behaviour of SMI signal. Then, the alpha measurement methods based on SMI are reviewed, which are classified into two categories: time-domain based and frequency-domain based. The comparison on those methods is given at the end of this section.

### 1.3.1 Introduction to SMI

Self-mixing interferometry (SMI) is developed based on self-mixing effect in lasers. Self-mixing happens when the emitted laser light reflected by a remote target, re-enters the laser active cavity and causes modulation of both laser output frequency and intensity. If the external target is subject to a movement, the laser output power fluctuates for each half-wavelength movement of the target along the laser emitting axis. The self-mixing effect was first observed on gas lasers such as He-Ne and CO2 lasers [34,35] and then on semiconductor lasers [36-39].

#### 1.3.1.1 System description

Compared to conventional interferometers, the interference in a SMI system occurs in the laser cavity between the internal optical field and a beam backscattered by an external target. The system can be very compact that a laser diode and a focusing lens are the only components for the laser head. Moreover, since the interference happens in the active cavity of laser diode, the reflected light is amplified in the cavity thus leads to stronger modulation.

The typical schematic of an SMI system is given in Figure 1-1. The core part of the system consists of a laser source and an external target. When the target moves, the light phase at external cavity will be varied, and thus results a modulation of the emitted laser power.

Usually, the modulated laser power is detected by the photodiode (PD) packed in the rear of the laser diode (LD). But for some special applications, the bandwidth of the build-in PD can be insufficient. In this case, an external PD will be used for signal detection through a beam splitter. The signal acquisition device includes a DC-coupled trans-impedance amplifier which amplifies and converts the current passing through PD into voltage, and an AD convertor which digitises and feeds the SMI signal into the signal processing unit for further processing. The laser controller and the temperature controller (LC and TC) stabilize the injection current and the operating temperature of the SL during the operation. The lens is used to focus the light beam onto the target. The attenuator is used to adjust the optical feedback strength.

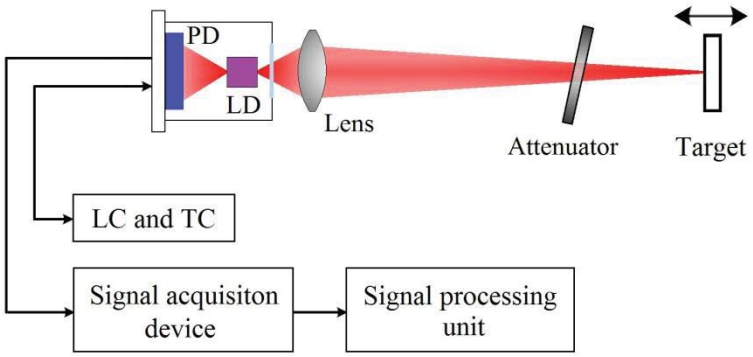


Figure 1-1: SMI system schematic.

### 1.3.1.2 Mathematical model

The widely accepted theory about the dynamics and stability of laser diode with optical feedback was conducted by Lang and Kobayashi yielding a set of fundamental rate equations to simulate the system [40]. The Lang-Kobayashi equations depicted the modulation of laser output intensity resulted from the variations in the external cavity length. The equations are listed as follows:

$$\frac{dE(t)}{dt}=\frac{1}{2}\left\{G_N\left[N(t),E(t)\right]-\frac{1}{\tau_p}\right\}E(t)+\frac{\kappa}{\tau_{in}}\cdot E(t-\tau)\cdot\cos\left[\omega_0\tau+\phi(t)-\phi(t-\tau)\right] \qquad (1.3)$$

$$\frac{d\phi(t)}{dt}=\frac{1}{2}\alpha\left\{G_N\left[N(t),E(t)\right]-\frac{1}{\tau_p}\right\}-\frac{\kappa}{\tau_{in}}\cdot\frac{E(t-\tau)}{E(t)}\cdot\sin\left[\omega_0\tau+\phi(t)-\phi(t-\tau)\right] \tag{1.4}$$

$$\frac{dN(t)}{dt}=\frac{J}{eV}-\frac{N(t)}{\tau_s}-G_N\left[N(t),E(t)\right]E^2(t) \tag{1.5}$$

where the contribution of the nonlinear gain suppression, the spontaneous emission and multiple reflections are neglected. The physical meanings of the symbols in Equations 1.3-1.5 are summarised in Table 1-1.

Table 1-1: Physical meanings for of symbols in L-K equations.

| *Symbol* | *Physical meaning* |
|---|---|
| $E(t)$ | electric field amplitude |
| $\phi(t)$ | electric field phase |
| $E^2(t)$ | Photon density in laser cavity |
| $N(t)$ | carrier density |
| $\omega_0$ | angular frequency for an LD without optical feedback |
| $G_N$ | modal gain coefficient |
| $\tau_p$ | photon life time |
| $\tau_{in}$ | LD internal cavity round-trip time |
| $\tau$ | external cavity round-trip time |
| $\tau_s$ | carrier life time |
| $J$ | injection current |
| $\kappa$ | reflectivity coupling parameter |
| $e$ | elementary charge |
| $V$ | volume of the active region |
| $\alpha$ | the alpha factor |

When the system described by above equations enters into a stationary state, we have $dE(t)/dt=0$, $d\phi(t)/dt=\omega_s-\omega_0$ and $dN(t)/dt=0$, where $\omega_s$ is the stabled angular frequency. By substituting $E(t)$ and $N(t)$ with constants $E_s$ and $N_s$, $\phi(t)$ with $(\omega_s-\omega_0)t$, $\phi(t-\tau)$ with $(\omega_s-\omega_0)(t-\tau)$, Equations 1.1-1.3 become [1-3]:

$$\omega_0\tau = \omega_s\tau + \frac{\kappa}{\tau_{in}}\tau\sqrt{1+\alpha^2}\sin(\omega_s\tau + \arctan\alpha) \tag{1.6}$$

$$N_s = N_0 + \frac{1}{\tau_p G_N} - \frac{2\kappa\cos(\omega_s\tau)}{\tau_{in} G_N} \tag{1.7}$$

$$E_s{}^2 = \frac{J/(eV) - N_s/\tau_s}{G_N\left(N_s - N_0\right)} \tag{1.8}$$

Considering the external cavity length is time varying, $\omega\tau$ can be replaced by $\phi$. For convenience, $\kappa\tau\sqrt{1+\alpha^2}/\tau_{in}$ is replaced by parameter $C$, which indicates the intensity of the reflected light, thus referred to as the optical feedback factor. Then Equation 1.4 becomes:

$$\phi_0 = \phi_F + C\cdot\sin(\phi_F + \arctan\alpha) \tag{1.9}$$

Equation (1.9) is called the phase condition equation, where $\phi_0$ and $\phi_F$ are the light phase without and with feedback respectively. By substituting Equation 1.5 into 1.6, the variation of the LD output power is expressed as:

$$P = P_0(1 + m\cdot g) \tag{1.10}$$

$$g = \cos(\phi_F) \tag{1.11}$$

where $P$ and $P_0$ are the LD power with and without feedback respectively; $g$ is the normalized LD power, also known as SMI signal; $m$ is called modulation parameter. Equations 1.9 - 1.11 are the common used stationary SMI model which has been widely accepted to describe the waveforms of SMI signals [31,32,41-44].

#### 1.3.1.3 SMI signal

For convenience, the SMI model equations are relisted here:

$$\phi_F = \phi_0 - C\cdot\sin(\phi_F + \arctan\alpha) \tag{1.12}$$

$$g = \cos(\phi_F) \tag{1.13}$$

In the phase condition equation (Equation 1.12), $\alpha$ and $C$ are two important system parameters, their values determines the features of SMI signals.

The optical feedback factor $C$ and its influence on SMI signals has been widely investigated and studied [45-48]. A few feedback regimes have been recognized with: weak $0 < C < 1$, moderate $1 < C < 4.6$, strong $C > 4.6$. Figure 1-2 respectively depicts the characteristics of SMI signals in different feedback regimes. Assuming the vibration of target is simple harmonic, as shown in Figure 1-2(a), then $\phi_0$ is expressed as:

$$\phi_0(t) = \varphi_0 + \Delta\varphi \sin(2\pi ft) \tag{1.14}$$

where $\varphi_0 = 4\pi L/\lambda_0$ and $\Delta\varphi = 4\pi\Delta L/\lambda_0$; $L$ is the initial external cavity length; $\Delta L$ and $f$ are target vibrating amplitude and frequency respectively. Then SMI signals can be generated by using Equations 1.12-1.13. The parameters used for Figure 1-2 are: $L$=0.45$m$, $\Delta L$=2.25$\lambda_0$, $f$ =100Hz, $\alpha$=3; $C$=0.7 in (b), $C$=2 in (c), $C$=5 in (d),.

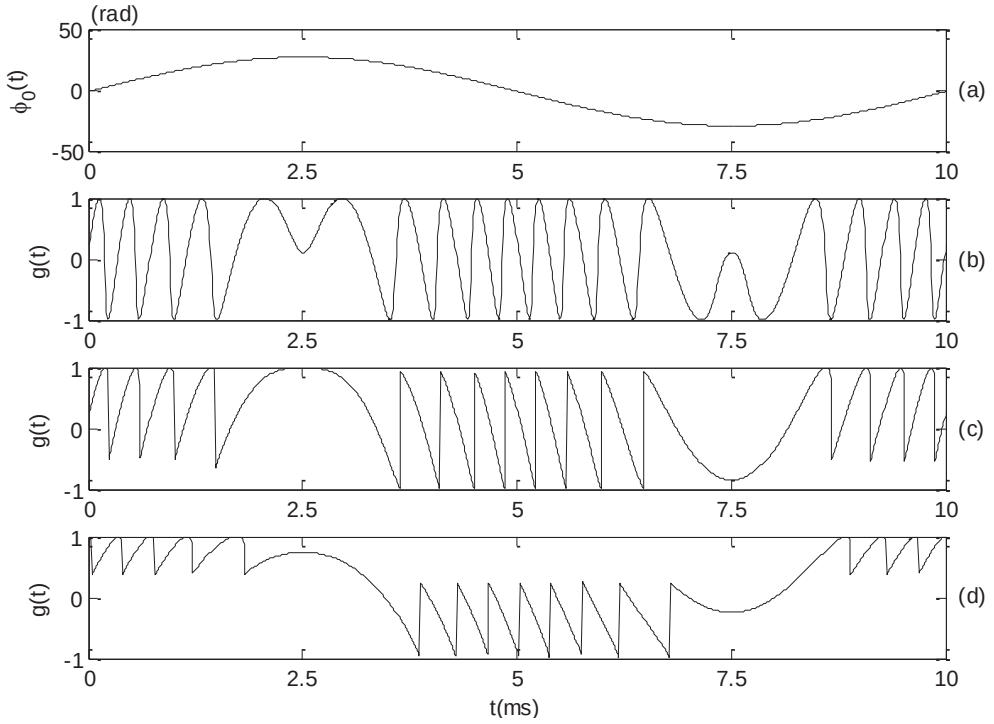


Figure 1-2: Simulated SMI waveforms: (a) target movement trace; (b) SMI under weak feedback; (c) SMI under moderate feedback; (d) SMI under strong feedback.

From Figure 1-2, it can be seen in weak feedback regime (Figure 1-2(b)) the SMI signal is sinusoidal and symmetrical-like. In moderate (Figure 1-2(c)) and strong feedback regime (Figure 1-2(d)), sharp transitions appear.

As illustrated earlier, $\alpha$ is an important parameter for semiconductor lasers, it determines multiple behaviours of the laser, including spectral effects, injection locking and the modulation response. Since its influence on SMI signal waveform is not in an obvious manner like $C$, only a few researches studied $\alpha$ from this perspective [45]. To give some illustrative examples, two sets of SMI waveforms are generated with a fixed constant $C$, and three different values for $\alpha$ in each set, as shown in Figure 1-3. The parameters used for Figure 1-3 are: $L$=0.45$m$, $\Delta L$=1.5$\lambda_0$, $f$=100Hz.

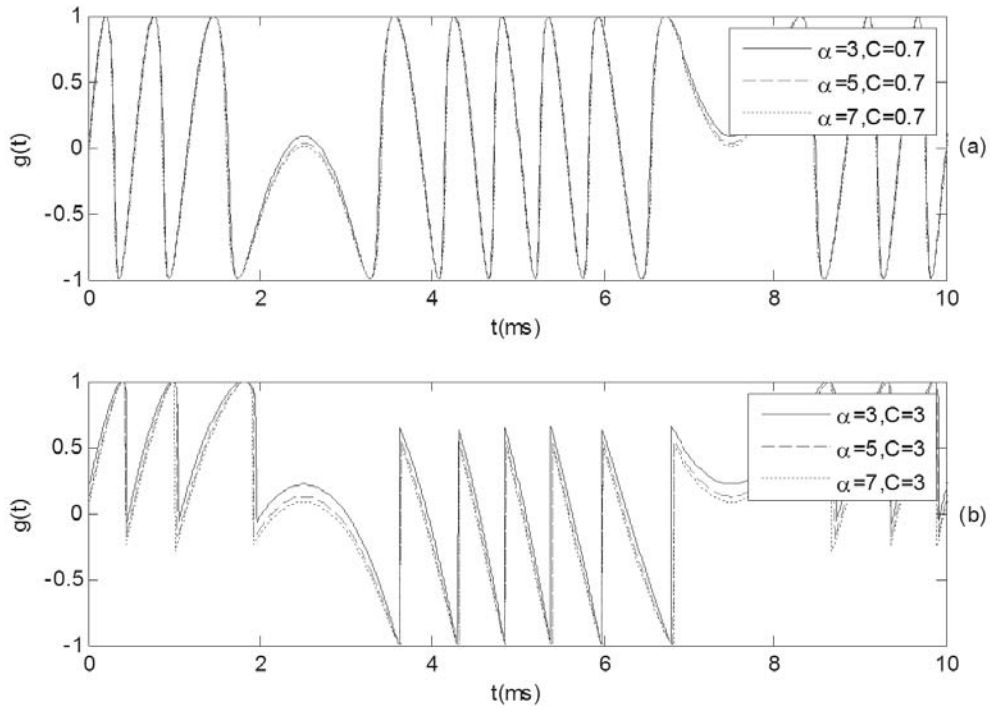


Figure 1-3: SMI signals with different $\alpha$ (a) week feedback case; (b) moderate feedback case.

The interval of $\alpha$ is set based on most of the laser diodes used for sensing applications, which lies within the range (3, 7). Figure 1-3 shows generally the SMI signals with different $\alpha$ values are fairly close. That is, compared to $C$ measurements, the estimation of $\alpha$ is more challenging. But it is worth notice that the difference caused by $\alpha$ is more distinct in

moderate feedback level than in weak feedback level. This suggests conducting $\alpha$ measurement in the moderate feedback regime is more likely to achieve accurate results.

### 1.3.2 Time-domain based methods

In 2004, Yu et al. proposed the first SMI-based $\alpha$ measurement method [23]. This method based on the hysteresis phenomenon in SMI signal and $\alpha$ is estimated from the characteristic points in the SMI signal waveform as shown in Figure 1-4 and Figure 1-5 [23].

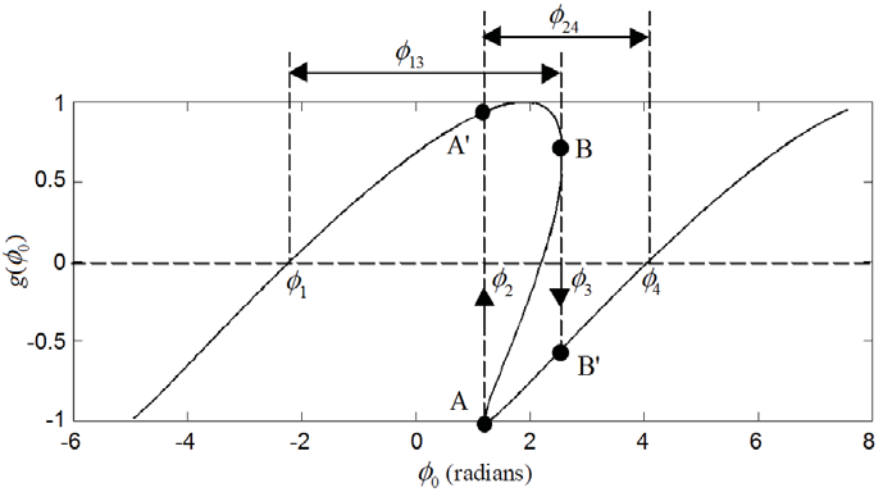


Figure 1-4: Hysteresis in the relationship between $\phi_0$ and $g(\phi_0)$.

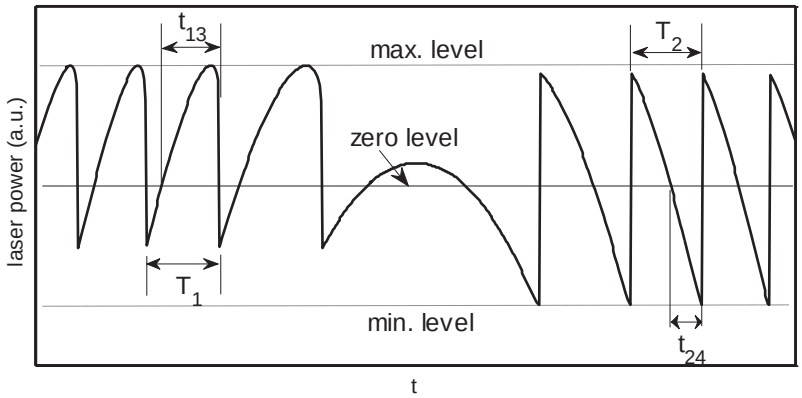


Figure 1-5: Simulated SMI signal at moderate feedback.

As illustrated earlier in previous sections, when the laser diode operates in the moderate feedback regime, the laser output power exhibits hysteresis and sawtooth-like fringes. When $\phi_0$ increases, $g(\phi_0)$ follows the path A'→B→B', while it follows a different path B'→A→A'

when $\phi_0$ decreases. Deriving from the SMI model equations, the relationship between $\alpha$, $C$ and the phase intervals between different phase points is obtained [23]:

$$\phi_{13} = \sqrt{C^2 - 1} + \frac{C}{\sqrt{1+\alpha^2}} + \arccos(-\frac{1}{C}) - \arctan(\alpha) + \frac{\pi}{2} \tag{1.15}$$

$$\phi_{24} = \sqrt{C^2 - 1} - \frac{C}{\sqrt{1+\alpha^2}} + \arccos(-\frac{1}{C}) + \arctan(\alpha) - \frac{\pi}{2} \tag{1.16}$$

Note $\phi_{13} = 2\pi t_{13}/T_1$ and $\phi_{24} = 2\pi t_{24}/T_2$. Thus, $\alpha$ and $C$ can be solved from Equation 1.15-1.16.

Although the above method is fast and easy, there are some restrictions that its usage and performance are limited. Firstly, the method works in moderate feedback regime and $C$ must less than approximately 3, otherwise, the hysteresis area will cover the phase interval $\phi_{34}$ and there will be no zero-crossing points when $\phi_0$ increases [49]. Secondly, the algorithm is achieved by assuming the external target is moving back and forth in a constant speed, which is hard to implement strictly in practice. To reduce the inherit error, the set of fringes which correspond to the moment that external target moves across the equilibrium position, should be used in calculation since they has the minimum acceleration and the movement trace is most linear.

In 2005, Xi et al. [24] developed a gradient optimization-based $\alpha$ estimation algorithm that works under weak optical feedback level. The core algorithm of this approach is data fitting technique, whereby the theoretical model incorporates an estimate of $\alpha$ and that are optimized to yield the best match for the observed SMI signal. For this purpose, a cost function is defined to achieve the best match which is the summation of square errors between the observed data samples and the calculated ones using the model. To speed up the process of fitting, gradient-based algorithm is employed that ensures $\alpha$ and $C$ update toward the direction that the cost function tends to minimum. The advantages of this method are simple implementation and suiting all single-mode laser diodes running in weak

feedback regime. On the other hand, the main limitation of this method is the external target must subject a pure harmonic vibration, and the prior knowledge of vibration trajectory is required, which is difficult to achieve in practice thus restricts the applicability of this method.

In 2005, Yu et al. [49] proposed an improved data-to-model fitting method for measuring $\alpha$ and $C$ that lifts the main limitation in [24]. This method addresses the situation where the target is subject to a simple harmonic vibration with unknown frequency and amplitude, leaving four variables to be identified in the cost function including $\alpha$ and $C$, target vibration amplitude and equilibrium position. To avoid the algorithm converging to a local minimum, initial parameter values must be carefully set in the beginning. The vibration frequency and the initial phase are estimated using auto-correlation and phase unwrapping respectively. The improvement in this method not only enhances the measurement accuracy but also reduces the difficulty of implementation of the system. Unfortunately, this method still only covers the weak feedback regime.

### 1.3.3 Frequency-domain based method

The idea of measuring LD parameters by analysing SMI signals in frequency-domain was first proposed by Yu et al. in 2011 [50]. The measurement equations are derived from the SMI theoretical model equations, which are relisted below:

$$\phi_F(t) = \phi_0(t) - C \cdot \sin(\phi_F(t) + \arctan\alpha) \tag{1.17}$$

$$g(t) = \cos(\phi_F(t)) \tag{1.18}$$

$$P(t) = P_0(1 + m \cdot g(t)) \tag{1.19}$$

Since the external target is moving periodically in this method, the above equations are expressed with respect to time variance. By taking Fourier transform on both sides, Equation 1.17 is transferred into frequency domain:

$$\Phi_F(f) = \Phi_0(f) - C \cdot F\{\sin(\phi_F(t) + \arctan\alpha)\} \tag{1.20}$$

where $\Phi_F(f)$ and $\Phi_0(f)$ are the Fourier transforms of $\phi_F(t)$ and $\phi_0(t)$ respectively; $F\{\cdot\}$ denotes the Fourier transform operation. Since the target is moving in simple harmonic, the spectrum of $\phi_0(t)$ should be very narrow that can be easily excluded from Equation 1.16 by applying a frequency interval where $\Phi_0(f) \approx 0$ ([50] suggests $f$>15$f_0$ which is 15 times bigger than the target vibration frequency). Meanwhile, by using the phase unwrapping technique in [51], we can obtain the phase signal $\phi_F(t)$, thereby its spectrum $\Phi_F(f)$. Finally, by giving $\alpha$ a reasonable value, the spectrum of $\sin(\phi_F(t) + \arctan\alpha)$ can be calculated, then $C$ becomes the only unknown factor in Equation 1.16 thus can be easily solved from spectrum. Although this method fails to work out the value of $\alpha$, it does provide a new approach of retrieving LD information from SMI signals.

Soon in 2013, Yu et al. [25] published an improved frequency-domain based method that is capable of measuring both $C$ and $\alpha$ simultaneously. In this work, the sin part in the phase condition equation (Equation 1.17) is expanded as:

$$\begin{aligned} &C \cdot \sin(\phi_F(t))\cos(\arctan(\alpha)) + C \cdot \cos(\phi_F(t))\sin(\arctan(\alpha)) \\ &= \sin(\phi_F(t)) \cdot \frac{C}{\sqrt{1+\alpha^2}} + \cos(\phi_F(t)) \cdot \frac{C\alpha}{\sqrt{1+\alpha^2}} \end{aligned} \tag{1.21}$$

By substituting $C/\sqrt{1+\alpha^2}$ and $C\alpha/\sqrt{1+\alpha^2}$ with $k_1$ and $k_2$ respectively, Equation 1.15 becomes:

$$\phi_F(t) = \phi_0(t) + k_1\phi_1(t) + k_2\phi_2(t) \tag{1.22}$$

where $\phi_1(t) = \sin(\phi_F(t))$ and $\phi_2(t) = \cos(\phi_F(t))$. By taking Fourier transform on Equation 1.19, we have:

$$\Phi_F(f) = \Phi_0(f) + k_1\Phi_1(f) + k_2\Phi_2(f) \tag{1.23}$$

And again, $\phi_F(t)$ is obtained by performing phase unwrapping on SMI signal, $\Phi_0(f)$ is excluded from the equation by applying a frequency interval, which leaves $k_1$ and $k_1$ the only unknown factors:

$$\Phi_F(f) = k_1\Phi_1(f) + k_2\Phi_2(f),\ \ f \subset \Omega \tag{1.24}$$

where $\Omega$ is defined as the frequency range $f \subset (15f_0,\ f_M)$, $f_M$ is the maximum frequency that $\Phi_0(f) \neq 0$. Considering above equation with respect to all the frequencies on $\Omega$, we have the following:

$$\Psi_F = k_1\Psi_1 + k_2\Psi_2 \tag{1.25}$$

By using $\Psi_F = \sum_{f\subset\Omega}\Phi_F(f)$ denotes the Since Fourier transform result is a complex function, the above equation can be separated into real and imaginary two parts. Then by taking a segment from spectrum for calculation which is denoted by $\Psi$, the values $k_1$ and $k_1$ can be estimated by jointly solving the two equations:

$$k_1 = \frac{\Psi_F^I\Psi_2^R - \Psi_F^R\Psi_2^I}{\Psi_1^I\Psi_2^R - \Psi_1^R\Psi_2^I},\ \ k_2 = \frac{\Psi_1^R\Psi_F^I - \Psi_1^I\Psi_F^R}{\Psi_1^I\Psi_2^R - \Psi_1^R\Psi_2^I} \tag{1.26}$$

where superscript $R$ and $I$ denote the real part and imaginary part of $\Psi$. Finally, $\alpha$ and $C$ are solved from:

$$\alpha = k_2 / k_1,\ \ C = \sqrt{{k_1}^2 + {k_2}^2} \tag{1.27}$$

In summary, this method measures $\alpha$ in frequency domain, the most significant benefit is it lifts the limitation in time domain measurements and covers a wide range of $C$. Moreover, this approach does not require the prior knowledge associated with target movements, such as external cavity length or target vibration amplitude.

Although the major algorithm of this method is frequency-domain based, the pre-processing procedures still have to be done in time-domain, e.g. noise cancelling and phase unwrapping, which may induce complicated consequences in frequency domain, thereby potentially degrade the accuracy of this method. The error analysis on the processing procedures of this method will be discussed in detail in Chapter 3.

### 1.3.4 Comparison

The overall comparison between different SMI based methods is summarised in Table 1-2.

Table 1-2: Comparison between different SMI based $\alpha$ estimation approaches.

| Approaches | Description | Accuracy | Requirements | Computational complexity |
|---|---|---|---|---|
| Time domain based | Using data-to-model fitting to obtain the only unknown parameters $\alpha$ and $C$ [2]. | ±6.7% | Accurate target moving trajectory, $0 < C < 1$ | High |
| | Using data-to-model fitting to obtain multiple system parameters including $\alpha$ automatically [3]. | ±3.9% | $0 < C < 1$ | High |
| | Using the hysteresis phenomenon in SMI signal and calculate $\alpha$ from the waveform [4]. | ±6.5% | $1 < C < 3$ | Low |
| Frequency domain based | Calculating the spectra of phase signals and calculates $\alpha$ from their functional relationship [1]. | no record | no feedback level limitation | Low |

By comparing the feasibility of the above methods, we can conclude that the frequency-domain based $\alpha$ measurement method in [25] is very promising. Firstly, there is no need to accurately adjust the optical feedback strength since the method covers a wide range of $C$. In practice, $C$ is depending on many factors including the structure of the laser diode and the characteristic of the external target. Therefore, measuring $\alpha$ in frequency domain greatly reduces the difficulty of system implementation and maintenance. In contrast, the method in [24] is hard to implement due to the additional requirement on the initial condition of SMI system, whereas the other methods [23,25,49] have less constraints on implementation. From the perspective of algorithm complexity, the methods based on data fitting techniques [24] and [49] are more suitable for off-line processing due to their huge computational

resources consumption; in this respect, measurement methods in [25] and [23] are more suitable for real-time measurement.

Based on the above comparison table and comments, it is clear that the frequency-domain based alpha measurement method possesses the advantages of high feasibility, easy implementation and medium computational complexity, which is ideal for implementing on other platforms (besides PC) in real-time.

## 1.4 Existing research problems and objectives

Since we need to demodulate the required information from SMI signals, the quality of signals plays a crucial role for achieving a high performance sensing and measurements. From the configuration of an SMI system shown in Figure 1-1, an SMI system contains both optical and electronic components. Noises can be introduced to an SMI signal from the external cavity (e.g. background light and cavity vibration), driving devices to the SL (e.g. temperature fluctuations, the detection circuit and the operating status of an SMI system), etc. There are three types of noises (or distortions) that commonly exist in SMI signals: slow fluctuation, Gaussian-like noise and transient oscillation. Unfortunately, there are very few investigations on SMI signal noise cancellation in literatures, and the existing processing techniques unable to handle all those noises. Especially for the transient oscillation which has strong influence on the measurement accuracy, to the best of our knowledge, there is no report on how to remove such noise. Hence, the development of an effective signal processing technique for suppressing the noises in SMI signals is required.

The frequency-domain based method is very promising as it has the advantages of high precision and wide feedback level applicable range [25]. Through this method, $\alpha$ can be retrieved from a wide range of frequency components. However, not all the frequency components can generate accurate measurement results due to the influence of noises. Although we can improve the signal quality by applying filters or other signal pre-processing

techniques, the influence of noises cannot be eliminated completely and it will propagate through the calculation. Therefore, the optimization on the signal processing and result selection of this method is an important topic for investigation.

For all the SMI based alpha measurement approaches mentioned in Chapter 1, the signal processing and alpha estimation are off-line. To meet the requirements of high-efficiency for practical applications, DSP platforms can be employed for real-time alpha measurement.

## 1.5 Thesis organization and contributions

The contributions of the work in this thesis are three-fold. Firstly, the influence of noises on the measurement accuracy is discussed, from which an effective filtering method is presented. Secondly, a series of optimization methods for improving the accuracy and reliability of the frequency-domain based $\alpha$ measurement against noises are proposed. Finally, a real-time $\alpha$ measurement is implemented on FPGA.

In Chapter 2, an overview is given on the features of SMI signals and all sorts of noises contained in the signal. Then, the existing filtering methods are reviewed. Finally, a new filtering technique is proposed specially for eliminating the influence of transient oscillation.

In Chapter 3, firstly the four stages of the frequency-domain based $\alpha$ measurement method are reviewed, which followed by a detail analysis on the error introduced at each stage. From the analysis, a series of optimization methods are proposed that can effectively prevent error propagation during the calculation.

In Chapter 4, an FPGA based real-time $\alpha$ measurement system using the frequency-domain based method is presented. The FPGA module design includes: signal acquisition module (analog to digital), signal pre-processing module (filtering and normalization), calculation module (phase and spectrum calculation) and result display module.

# Chapter 2. SMI signals and filtering

In the previous chapter, the mathematical model and the basic setup of a SMI system has been introduced, as well as the characteristics of ideal SMI signals. The signal quality plays a crucial role in the performance of SMI based sensing. However, ambient noise, electronic noise and thermal noise are inevitably in SMI systems, which can seriously degrade the accuracy of measurement. As a result, noise removal is an important topic in this area of research. A few digital filters have been proposed to suppress the noises in SMI signals [52], but these methods are still limited and not able to effectively remove the transient oscillation.

This chapter is focused on how to acquire a clear SMI signal. Firstly, an overview is given on the features of SMI signals and all sorts of noises contained in the signal. Then, the existing filtering methods are reviewed. Finally, a new filtering technique is proposed specially for eliminating the influence of transient oscillation.

## 2.1 Noises and distortions in SMI systems

### 2.1.1 Experimental system

The typical scheme of an experimental SMI system is implemented and shown in Figure 2-1. It mainly consists of three parts: a laser source, a controlled target and a signal detection system.

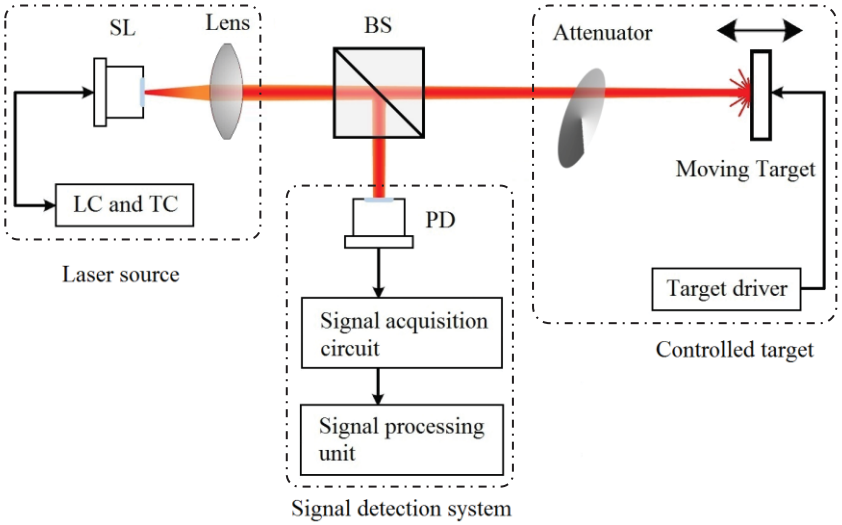


Figure 2-1: Experimental SMI system schematic with external PD.

A laser source consists of a semiconductor laser diode, a laser diode driver and a focusing lens. In practice, the SL and the lens are always packed in one device for better stability and alignment, e.g. the SL mount shown in Figure 2-2, which also provides interfaces for the laser controller and the temperature controller (LC and TC). The LC is mainly functioned as a current controller, providing stable injection current or modulated injection current for various applications [44,53]. The TC allows the laser to be temperature controlled for stable operation. The lens is used to focus the light emitted by the SL onto the target, and the lens coating also reduces unwanted background light.

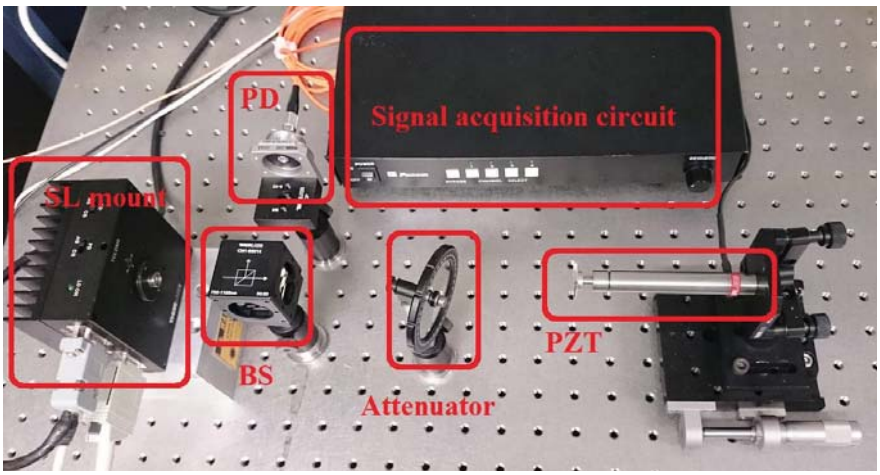


Figure 2-2: SMI experimental system.

A controlled target consists of a moving target, a target driver and an attenuator. In practice, the controllable target can be a PZT (piezoelectric ceramic transducer) or simply a loudspeaker depending on the precision requirement of measurements. The target driver connected with a signal generator will allow the target moving in certain pattern, which is required by some of SMI based applications [23,24,32,44]. The attenuator is installed for diming the reflected laser light since some SMI based measurements have strict limitations on the optical feedback level [23,24,54].

A signal detection system consists of a PD, a signal detection circuit and a digital data acquisition (DAQ) device. Although it is common that for many laser diodes, there is a built-in PD packaged at the rear of SL, due to the limit in the rising time of the PD (or can be considered as the cut-off frequency is limited), it may not be able to detect the details in a high frequency SMI waveform [55]. Therefore, an external detection PD is employed in some cases [55,56]. Since the amplitude of SMI signals are very weak [52], so a signal detection circuit is required to pick out the signal and amplify it. The details of an experimental signal detection circuit will be discussed in Section 2.1.4. Finally, the analog signal is converted into digital signal via a DAQ device and fed into a signal processing terminal.

Since the signal passes through both optical and electrical paths, ambient noise, electronic noise and thermal noise are inevitable in practice. A significant issue that impacts on the performance of SMI is the quality of signals. Figure 2-3(a) gives an example of experimental SMI signals when the target is subject to a simple harmonic vibration, which mainly contains two types of noises: white noise (enlarged in Figure 2-3(b)), transient oscillation (enlarged in Figure 2-3(c)). Furthermore, slow fluctuation is also very common in experimental signals. In the following sections, the causes of these noises will be analysed and the possible solutions will be discussed.

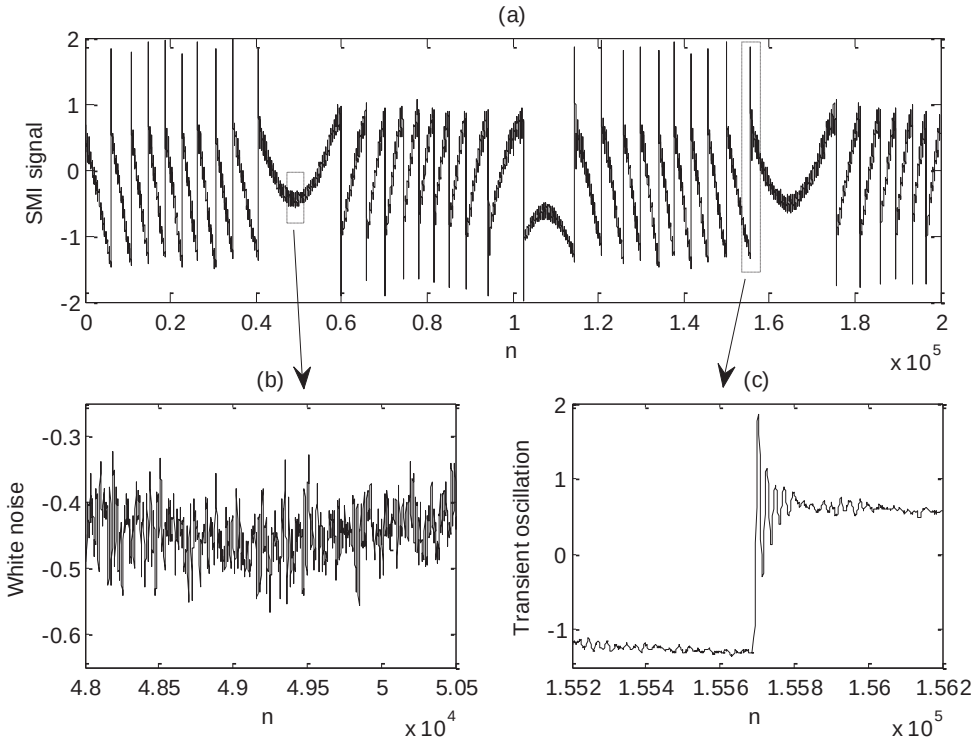


Figure 2-3: (a) A piece of experimental SMI signal; (b) white noise in the signal; (c) transient oscillation in the signal.

### 2.1.2 Transient oscillation

Transient oscillation happens when the system enters the moderate feedback regime, i.e. when $C$ > 1 and the SMI signal shows sawtooth-like fringes. For the stable-state SMI model, multiple solutions can be obtained in the moderate feedback regime, which leads to discontinuities in the modelled laser power when the external cavity length changes. This phenomenon is related to the assumptions made for simplification, i.e. $dE(t)/dt = 0$, $d\phi(t)/dt = \omega_s - \omega_0$ and $dN(t)/dt = 0$. While unique solution can be obtained by solving the complete L-K equations. A simulated self-mixing signal which is calculated from the L-K equations is plotted in Figure 2-4 ($L$=1m, $\Delta L$=1.5$\lambda_0$, $f$=80KHz, $C$=2.5, $\alpha$=3.5), in which the laser power shows damped oscillations where the stable-state model predicts discontinuities.

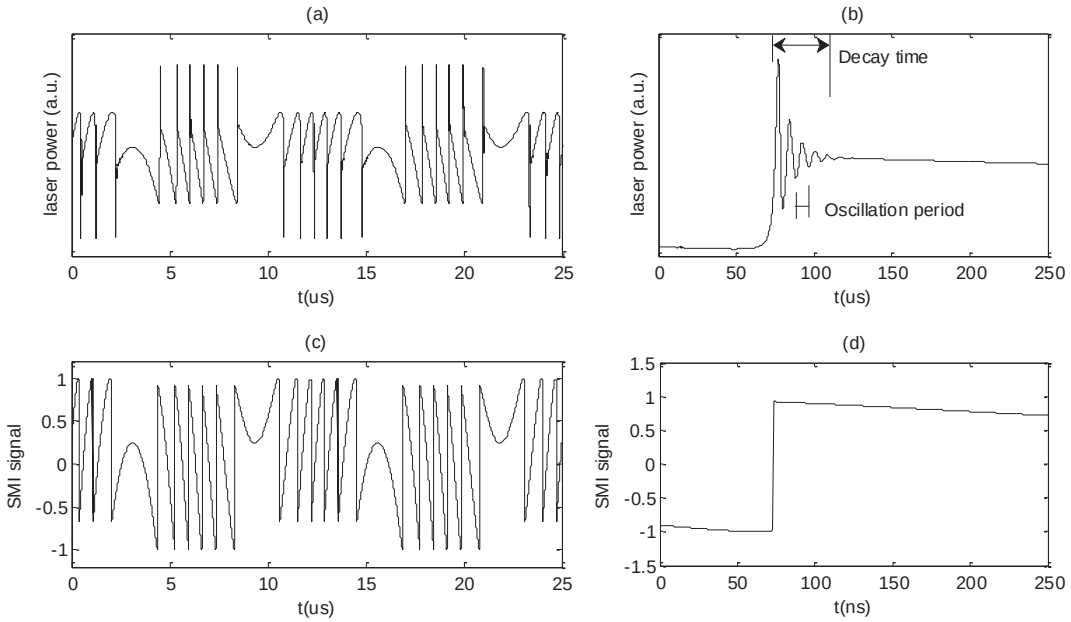


Figure 2-4: (a) and (c): simulated SMI signals respectively generated by L-K equations and stable-state model; (b) and (d): details enlarged for the sharp changing edges in (a) and (c).

Damped oscillations are often described by their amplitude, decay time and oscillation period (frequency). According to the research in [56,57], there are three factors can significantly influence the features of transient oscillation: optical feedback strength ($C$), laser-to-target distance ($L$) and the linewidth enhancement factor ($\alpha$). The oscillation amplitude varies proportional with $C$ [57]. The oscillation period increases with $L$ and $\alpha$ [56,57]. And finally, increasing any one of the three factors will extend the decay time [56,57].

When the external target moves at low speed in the moderate feedback regime, the duration of transient oscillation is much less than a fringe, which can be easily eliminated by simple filtering and lowering the sampling frequency. However, if the target moves at high speed, the oscillation will take a comparatively big part of the fringe. In this case, although the SMI signal with transient oscillations still has the basic interference resolution for displacement sensing like normal SMI signals, for some applications, such as accurate displacement reconstruction and laser diode parameter estimations, the measurement performance can be severely degraded. Besides, the overshoots in oscillations will also cause

problems when normalizing the signal for further information demodulation. Therefore, to guarantee the measurement accuracy, it is desirable to remove the transient oscillations.

Narrowing the bandwidth of acquisition system is a straightforward way to avoid transient oscillation, but the original signal will also be distorted, an example is given in Figure 2-5. Figure 2-5(a) and (c) are the processing results of applying low-pass filters with different cut-off frequencies (100MHz and 30MHz respectively) on the signal in Figure 2-4(a). Figure 2-5(b) is an enlarged view on the sharp changing part in Figure 2-5(a), which suggests the transient oscillations can pass through the system when the bandwidth is wider than 100MHz. While in Figure 2-5(d), which is enlarged from Figure 2-5(c), the sharp edge has been seriously blurred. Therefore, adjusting the bandwidth is not a desirable way to remove transient oscillations.

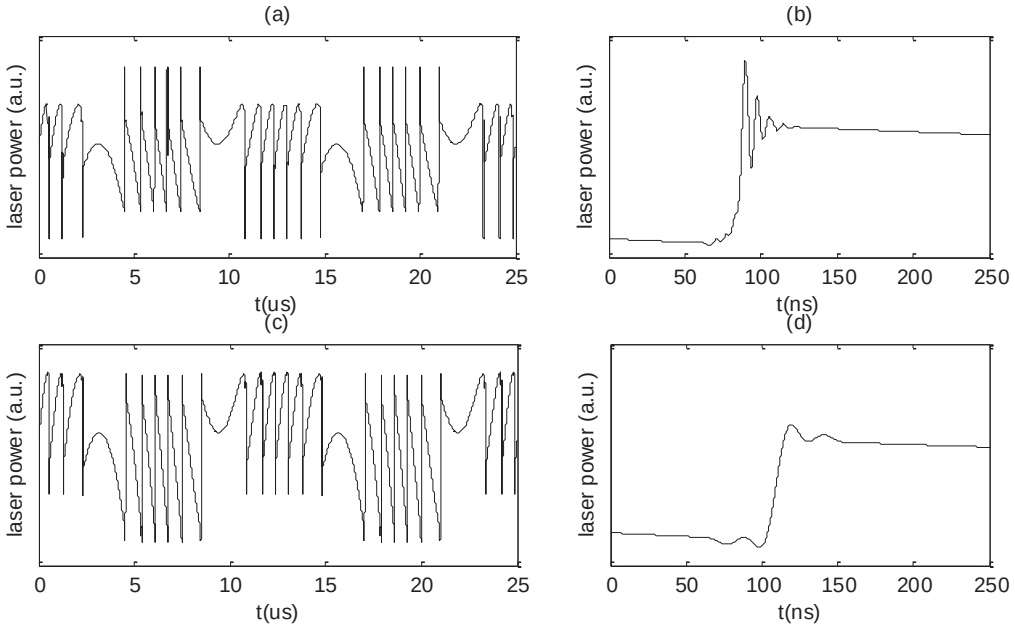


Figure 2-5: (a) and (c): results obtained by applying low-pass filters on the signal in Figure 2-4(a); (b) and (d): enlarged details of the sharp changing edges in (a) and (c).

Since it is hard to control or avoid the transient oscillations during the measurement process, the development of an effective digital filter to remove those oscillations is required. In Section 2.3 we propose to use a Myriad filter to solve this problem, which is capable of removing oscillations while preserve the details in signal.

### 2.1.3 Slow fluctuation

Slow fluctuations commonly exist in SMI signals when the external target is subject to reciprocating movements, e.g. sinusoidal movement and triangle wave movement. Examples can be found in: Fig. 7 in [46], Fig. 5 in [58], Fig. 1 in [59], Fig. 2 and Fig. 3 in [60], etc.

Figure 2-6 gives two examples of slow fluctuations which were observed in our experimental SMI system. In Figure 2-6(a), it can be seen the slow fluctuation shares the same fundamental period (or frequency) with the target movement. While in Figure 2-6(b), the slow fluctuation is more like an additive sinusoidal interference, which appears to be irrelevant to the fundamental period of SMI signal. According to our research, the slow fluctuation phenomenon is related to the operating frequency range (bandwidth) of the signal acquisition circuit.

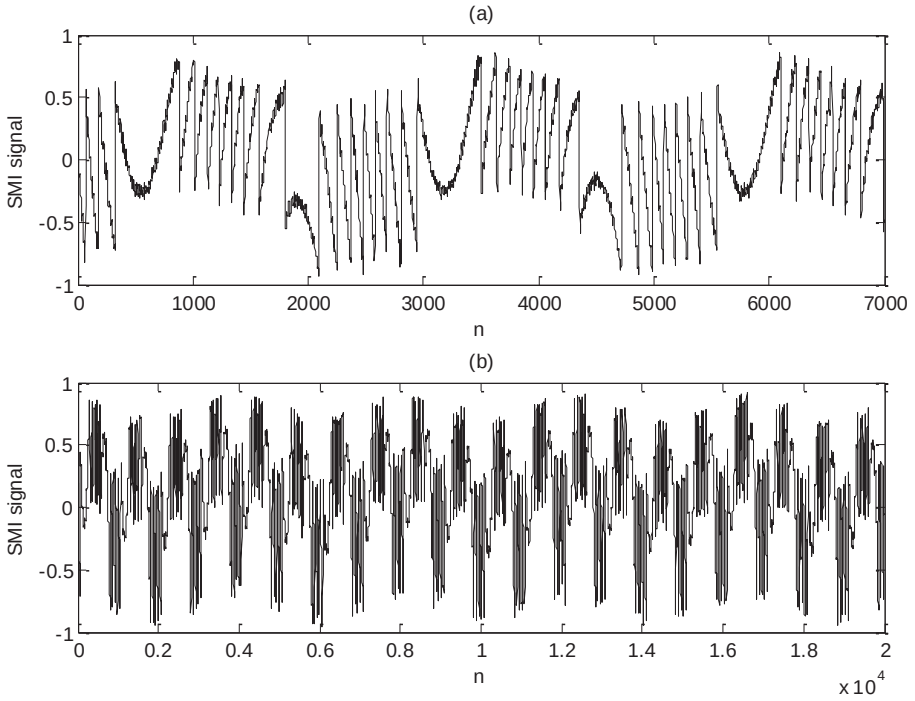


Figure 2-6: Examples of SMI waveforms containing slow fluctuations.

A simplified signal detection circuit is depicted in Figure 2-7, which consists of two parts: an optoelectronic conversion circuit (within the dashed box) and a trans-impedance amplifier.

Between those two parts, an AC-coupling capacitor (or called DC-blocking capacitor) is employed for the following purposes:

1) Extracting SMI signal from the received laser power thus avoid amplifying the signal to an excessive power level, which increases the system instability and enhances the performance of AD converter;

2) Isolating low-frequency noises, including temperature variations, mechanical vibration, power noise and other slow-time noises inherited from the LD (e.g. servo effects in LD driver).

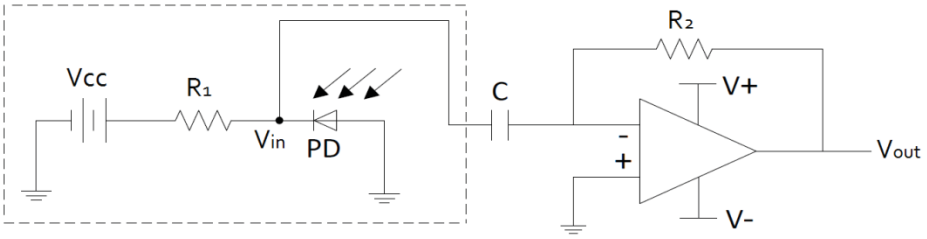


Figure 2-7: Signal acquisition circuit.

Unfortunately, the coupling capacitors can also introduce nonlinear distortion when the signal contains lower frequency components relative to the RC cut-off frequency. Then, the low frequency components can develop across the capacitor, leading to distortions, in this case, slow fluctuations. To solve this issue, a capacitor with higher capacitance should be used in the circuit which lowers the cut-off frequency, or alternatively, increasing the fundamental frequency of SMI signal, i.e. target vibration frequency.

To test above assumptions, we conducted simulation tests with a powerful software tool Simulink, which supports importing SMI signals into an analog circuit model. The circuit model is plotted in Figure 2-8, where “Input port” and “Output port” are modules work as digital signal generating and recording unit respectively. Simulation results are plotted in Figure 2-9.

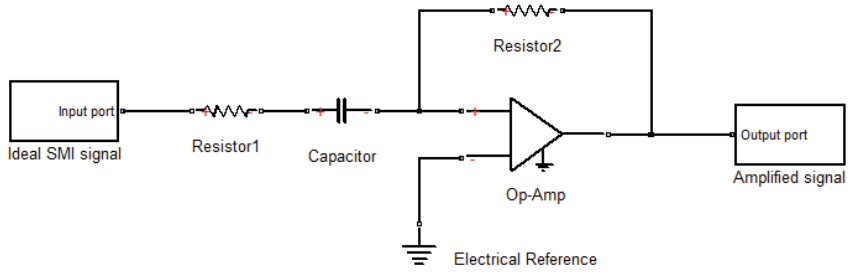


Figure 2-8: Analog circuit model built in Simulink.

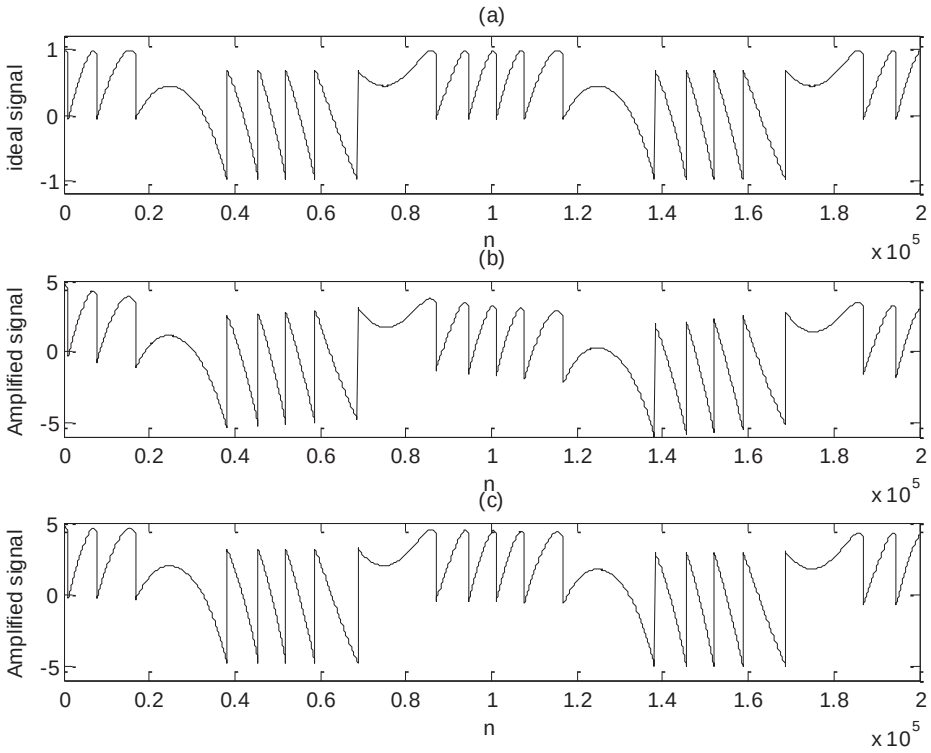


Figure 2-9: (a) Input simulated SMI signal; (b) and (c): signals before and after correcting the capacitance respectively.

The ideal SMI signal (in Figure 2-9(a)) is generated by Matlab using SMI model ($L$=0.45$m$, $\Delta L$=1.4$\lambda_0$, $f$ =100Hz, $\alpha$=3, $C$=3). Firstly, we assigned the capacitor with a small value, and the output signal in Figure 2-9(b) is clearly covered in slow fluctuations, which just like the experimental signal shown in Figure 2-6(a). Then we increased the value of capacitor to a much bigger value, and the result in Figure 2-9(c) suggests the problem has been solved effectively. Meanwhile, the slow fluctuation phenomenon in our experimental system also

was well suppressed after the target vibration frequency adjusted to a higher level (since the capacitor in our circuit is fixed on board).

In summary, the slow fluctuation in an SMI system is most likely caused by inappropriate AC coupling configurations. Either upgrading the capacitor or increasing the fundamental frequency of SMI signal can suppress this phenomenon.

## 2.2 Existing filtering methods

The main existing filtering methods for SMI signal pre-processing including linear FIR filter, median filter, Kaiser window filter, outlier detection method. In the following paragraphs, these filtering methods will be briefly introduced and discussed regarding their filtering performance and feasibility in practice.

- **FIR filter**

The classic processing flow of an Nth-order discrete FIR filter is given in Figure 2-10.

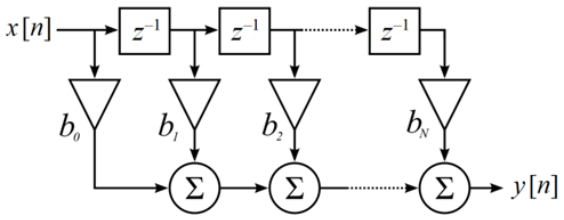


Figure 2-10: Block diagram of a simple FIR filter.

Where $x[n]$ and $y[n]$ are input signal sequence and output signal sequence respectively. $z^{-1}$ represents the delay operator in Z-transform notation. $b_0, b_1, \dots, b_N$ are coefficients of the filter. Because of the complexity of SMI signals, an FIR filters with constant coefficients is hard to meet the requirement of noise cancelling and even can result in distortions, an example is given in Figure 2-11. For demonstration purpose, a piece of simulated clean SMI signal (a segment from Figure 2-9(a)) is used so it can be seen that the details of the sharp edges are lost after went through an FIR filter.

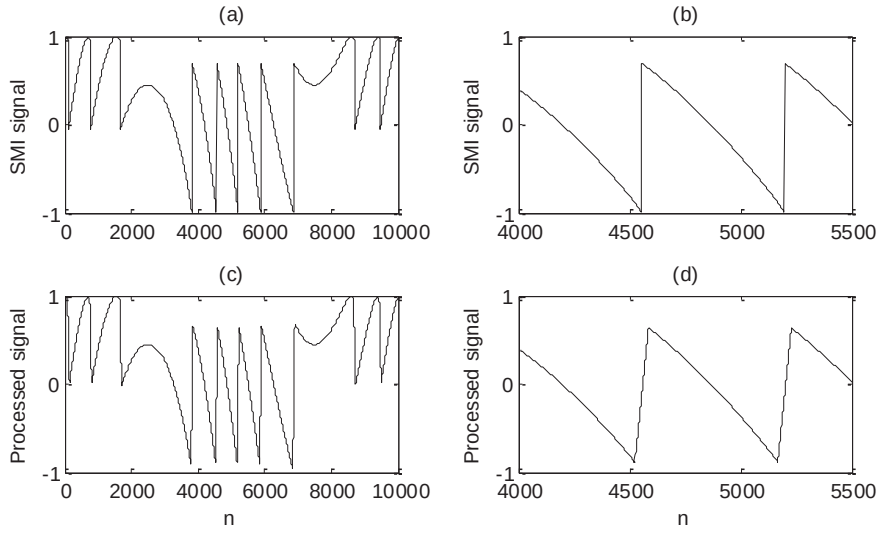


Figure 2-11: Processing results for simulated signals: (a) a piece of ideal SMI signal; (b) an enlarged view on the sharp fringe edges in (a); (c) the processing results of (a); (d) an enlarged view on the distorted edges after filtering.

- **Median filter**

Median filters are typical non-linear filters which has been widely used in digital image processing because of its edge preservation property and efficient noise attenuation with robustness against impulsive type noise (speckle noise and salt and pepper noise) [61,62]. The median (usually denoted by $MED$ in expressions) of an odd number of $N$ elements vector is the $[(N+1)/2]$th largest element. When using median in a sliding window as a filter, the output of a median filter is calculated after the odd number of sample values in the window are sorted, and the middle or median value is used as the filter output. The filtering procedure is defined as:

$$y(n) = MED[x(n-N_1),\ldots,x(n),\ldots,x(n+N_2)] \tag{2.1}$$

where $N$ is window length (if $N$ is even then $N_1 = N/2$ and $N_2 = N_1 - 1$; if $N$ is odd then $N_1 = (N-1)/2$ and $N_2 = N_1$). To demonstrate its outlier rejecting property, a median filter using a window size of three will be applied to the simple signal vector $x = [1, 2, 50, 3, 0]$, then, the median filtered output sequence is calculated as follows:

$y(1) = MED[1, 1, 2] = 1$

$y(2) = MED[1, 2, 50] = 2$

$y(3) = MED[2, 50, 3] = MED[2, 3, 50] = 3$

$y(4) = MED[50, 3, 0] = MED[0, 3, 50] = 3$

$y(5) = MED[3, 0, 0] = MED[0, 0, 3] = 0$

i.e. $y = [1, 2, 3, 3, 0]$.

By comparing the output sequence with the input, it is clear the outlier sample value $x(3) = 50$ has been eliminated. Such outlier rejecting feature makes median filter desirable for removing sparkle-like noise, especially salt and pepper noise.

It is noticeable in the above example that the first value and the last value are repeated during the process since there are not enough entries to fill the running window. Not just for median filter, it is common in signal processing with a sliding window that need handling missing window entries at the boundaries of the signal. In addition to this scheme, there are other ways to solve this issue in other particular circumstances:

1) Skip processing the boundaries if the window is small enough compared to the whole signal that the influence of both beginning and ending of the signal is negligible;

2) Shrink the window near the boundaries, so that every window is full;

3) Fill the window with the samples in adjacent periods if the signal is periotic.

Despite the advantages, a median filter's performance suffers when dealing with sustained noises (or distortions), e.g. the oscillations in SMI signals. To demonstrate this flaw, a piece of simulated SMI signal with oscillations is processed and the result is given in Figure 2-12. Although the impulses are removed as shown in Figure 2-12(d), the edge is also smoothed just like being processed by a low-pass filter.

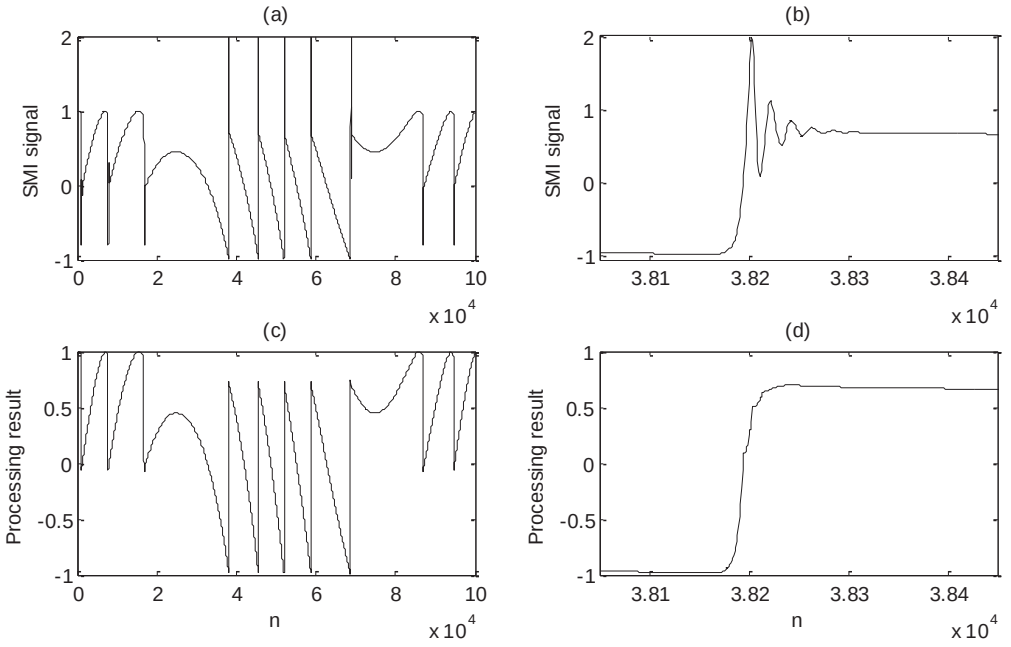


Figure 2-12: Processing results using a median filter: (a) simulated SMI signal with overshoot; (b) an enlarged view of the overshoot in (a); (c) the processing result of (a); (d) the overshoot after being filtered.

- **Kaiser window filter**

In [52], the authors proposed a filtering method that combined a median filter and a band-pass filter based on Kaiser window. The impulse response of the filter is described by:

$$h[n] = w[n]h_d[n]\cos\omega_0 n \tag{2.2}$$

where $h_d[n] = \sin\omega_c n/\pi n$, $\omega_c = \omega_{c2} - \omega_{c1}$ is the pass-band width. $\omega_0 = (\omega_{c1} + \omega_{c2})/2$ being the central frequency, where $\omega_{c1}$ and $\omega_c$ are two boundaries of the frequency band. The Kaiser window function $w[n]$ is defined as:

$$w[n] = \begin{cases} I_0\left[\delta_1\sqrt{1-\left(\dfrac{n-\delta_2}{\delta_2}\right)^2}\right], & 0 \le n \le N \\ 0, & else \end{cases} \tag{2.3}$$

Where $I_0(.)$ is the zero-th order modified Bessel function of the first type, $\delta_1$ is a parameter that determines the shape of the window. $\delta_2$ is half window width that equals to $N/2$, where $N$ is the window width. By running simulations on experimental SMI signals, the optimal boundaries of frequency band can be determined.

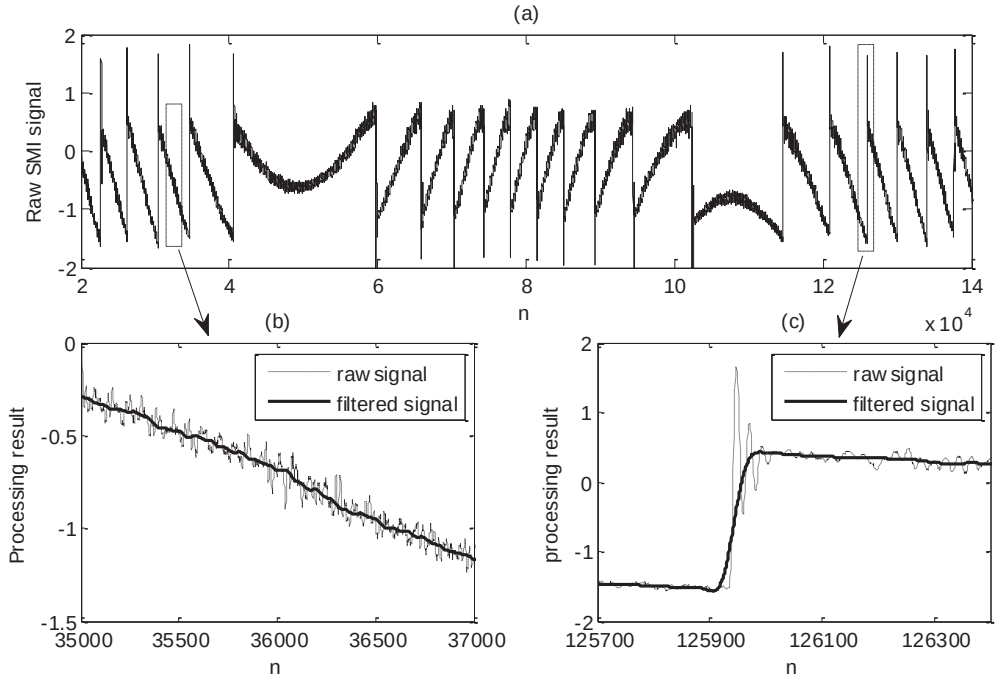


Figure 2-13: Processing results for an experimental SMI signal at moderate feedback: (a) raw SMI signal; (b) and (c): processing results (just show the enlarged view for the two pieces indicated in (a)).

The original intention of combining median filter with Kaiser window function is to improve the performance of median filter on suppressing high frequency noises. Unfortunately, the Kaiser window filter belongs to the class of FIR band-pass filters, which means both smoothing and blurring property of FIR filters are inherited. Figure 2-13 gives the example of using a median filter with Kaiser window function to process a piece of experimental SMI with oscillations at the edges. As demonstrated by Figure 2-13(b), the high frequency components are removed from the signal, while the sharp changing edges are also smoothed as shown in Figure 2-13(c).

- **Outlier detection approach**

An outlier detection approach was proposed in [63], which proposed an approach that detecting the data samples corrupted by the noises and then using the least square curve fitting to rectify the waveform. The idea of the outlier detection approach are summarised as follows:

1) Set a standard reference by using linear equation;

2) Determine the two coefficients in the standard reference equation by minimizing the cost function which is defined as the summation of square errors between the observed data samples and the fitting parameters;

3) Evaluate the smoothness of every data sample in the waveform sequentially by referencing to the standard reference trajectory and thus locate the position of corrupt signal samples including transient overshooting;

4) Replace the located noise samples with the curve fitting result which is based on the reference sample set.

An example of using outlier detection method to process SMI signals is given in Figure 2-14 where the same piece of SMI signal shown in Figure 2-13(a) is processed. It can be seen from the processed waveform that the white noise is reduced and most of the transient oscillation has been removed, except the raising edge part.

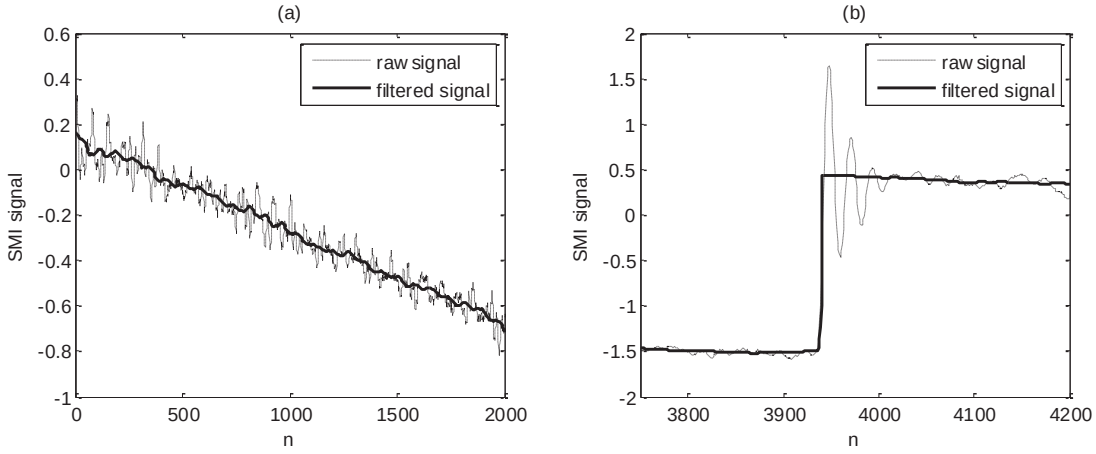


Figure 2-14: Processing results by outlier detection method on the experimental signal in Figure 2-13(a): (a) the enlarged view on the slow changing part; (b) the enlarged view on the sharp changing edge.

Additionally, the processing sequence of this approach is backwards and every fringe needs to be processed separately. The non-casual property of this approach determines it is only suitable for post-processing on computers instead of working in real-time like other filters.

In summary, all the existing pre-processing methods have merits and shortcomings: FIR filters and Kaiser window filters are good at high frequency white noise cancelling while can seriously blur the sharp changing edges; median filters are very effective to impulse noises and salt/pepper noise while has poor performance on handling sustained noises like damped oscillations; the outlier detection approach has passible performance on white noise and overshoots removal, but its application is limited to post-processing on computers.

## 2.3 A new filtering method

### 2.3.1 Introduction to Myriad filter

The theory of non-linear filtering was proposed with the intension of lifting the limitations in linear filtering whenever the underlying processes are impulsive. At first, median based filters were widely preferred in 1-D and image processing since it possesses the properties of impulse resistivity and relative computational simplicity [64]. Then, it has been noticed that filters based on the median operator are not very flexible that their output is always constrained to one of the samples in the input window [65,66]. Meanwhile, median based filters tend to blur edges when smoothing noisy signals, and are not capable of performing edge enhancing operations [64].

The Myriad filter was proposed as a robust, non-linear filtering and an estimation technique in impulsive environments (e.g. atmospheric noise in radio links, switching transients in telephone channels, and multiple access interference in radio communication networks [65]). It represents a wide class of maximum likelihood type estimators (M-estimators) of location [67].

The structure of location M-estimator is defined as:

$$\hat{\beta}_K = \arg\min_{\beta} \sum_{i=1}^{N} \rho(x_i - \beta) \tag{2.4}$$

where $x$ is a set of samples in length $N$; $\beta$ is the estimated value which minimizes the expression; $\rho$ is the cost function associated with the estimator which plays an important role in the characterization of M-estimators [64]. The class of Myriad filter is based on the Cauchy distribution which has the probability density function when scaling factor $K > 0$:

$$f(z;\beta) = \frac{K}{\pi}\frac{1}{K^2 + z^2} \tag{2.5}$$

where $z$ denotes $x - \beta$ that is the location parameter, scaling factor $K$ is also known as the half interquartile range. Its associated cost function is described by:

$$\rho(z) = \log\left(K^2 + z^2\right) \tag{2.6}$$

The expression of cost function defines the class of selection Myriad estimators, which has proven successful in the management of signal smoothing and edge enhancing [68,69]. As illustrated in the previous section, the existing filtering approaches can cause serious blurry at the sharp changing edges. Therefore, for SMI signal processing, the later property of Myriad estimator is extremely desirable, which makes Myriad a highly promising candidate for removing the transients without blurring the waveforms.

The complete expression of Myriad estimator is given as following:

$$\begin{aligned} \hat{\beta}_K &= myriad\{K; x_1, x_2 ..., x_N\} \\ &= \arg\min_{\beta} \sum_{i=1}^{N} \log[K^2 + (x_i - \beta)^2] \\ &= \arg\min_{\beta} \prod_{i=1}^{N} [K^2 + (x_i - \beta)^2] \end{aligned} \tag{2.7}$$

In Myriad estimator, the scaling factor $K$ is rather referred as the linearity parameter since it controls the impulse-resistance (outlier rejection capability) of the estimator. This parameter offers a rich class of operation that can be easily controlled by tuning the value of $K$. The impact of $K$ on the behaviour of Myriad estimator has been extensively investigated [64-66,70,71]. When $K \to \infty$, the estimator converges to the sample average that is the Gaussian-efficient sample mean behaviour (linear property). When $K \to 0$, the estimator

tends to favour values near the most repeated clusters of input samples which represents the behaviour of impulse-resistant, that is the mode property (non-linear property) of Myriad, or short for mode-myriad. The following figure is given to interpret the definition of Myriad in a more intuitive manner, which shows the mechanism of how $K$ influences the estimation output in a geometrical way [69].

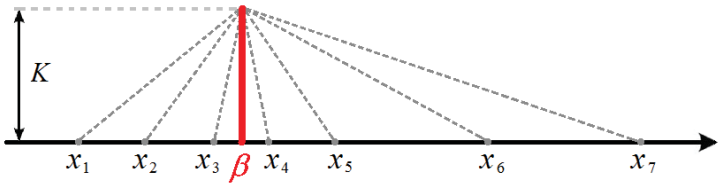


Figure 2-15: Geometrical interpretation of Myriad estimation.

Considering $|x_i - \beta|$ and $K$ in Figure 2-15 as the base-side and height of a right triangle respectively, then the hypotenuse has the expression of $K^2 + (x_i - \beta)^2$ which is the basic element in Equation 2.7. That is, the output of the estimator is actually the location that minimises the product of all the hypotenuses. With the assistance of above figure, it is easy to imagine: when $K$ is small, the output of Myriad estimator should converge to the densest area of input values, thus rejects the outlier values which are far away from the cluster; if tuning $K$ to +∞, or more practically, much longer than the differences of input samples (the differences of input samples $x_1, \ldots, x_7$ between each other), every hypotenuse tends to be equal in length which means the final output is equally influenced by all the input samples, thus the estimator will degrade into an averager.

It is important to realise that the location estimation being considered is related to the problem of filtering a time-series signal using a sliding window. The input of the Myriad filter is the sequence of SMI signal samples, denoted by $g(n)$. And the width of sliding window, that is the quantity of input samples $N$ in Myriad estimator. According to the definition in (4), the output of the Myriad filter with window width $N$ is expressed as:

$$\hat{g}(n) = myriad\{K; g(n-N), g(n-N+1), .., g(n)\}$$
$$= \arg\min_{g} \sum_{i=0}^{N} \log\{K^2 + [g(n-i) - g]^2\} \tag{2.8}$$

There are two important parameters in above expression, one is the linear parameter $K$ and other is the slide window width $N$. The values of these two parameters determine the characteristics of Myriad filters. In the following section, the configuration of these two parameters for achieving a good filtering result on an SMI signal will be deeply investigated.

### 2.3.2 Design of Myriad filter

#### 2.3.2.1 Configuration of $K$

As mentioned in last section, the value of $K$ determines the output feature of Myriad filters. Figure 2-16 presents a series of enlarged views on the Myriad processed signals with different $K$ value settings. According to the processioning results shown in Figure 2-16(b) and (c), the transient oscillations at sharp changing edges are all removed after applying the Myriad filter, regardless of the value of $K$. By comparing the details in filtering results, we can conclude that: when $K$ is small, the Myriad filter reflects strong non-linear property that mainly targets the oscillations, thus not very effective to white noise, as shown in Figure 2-16(b); when $K$ is large, the Myriad filter degenerates into a linear filter that smooths the whole waveform including white noise and sharp changing edges, as shown in Figure 2-16(c). In practice, as the SMI signal contains both white noise and transient oscillations (when in moderate feedback regime), the two properties of Myriad filter need to be balanced by choosing a suitable $K$ thus eliminates the transient oscillations while preserve the sharp edges.

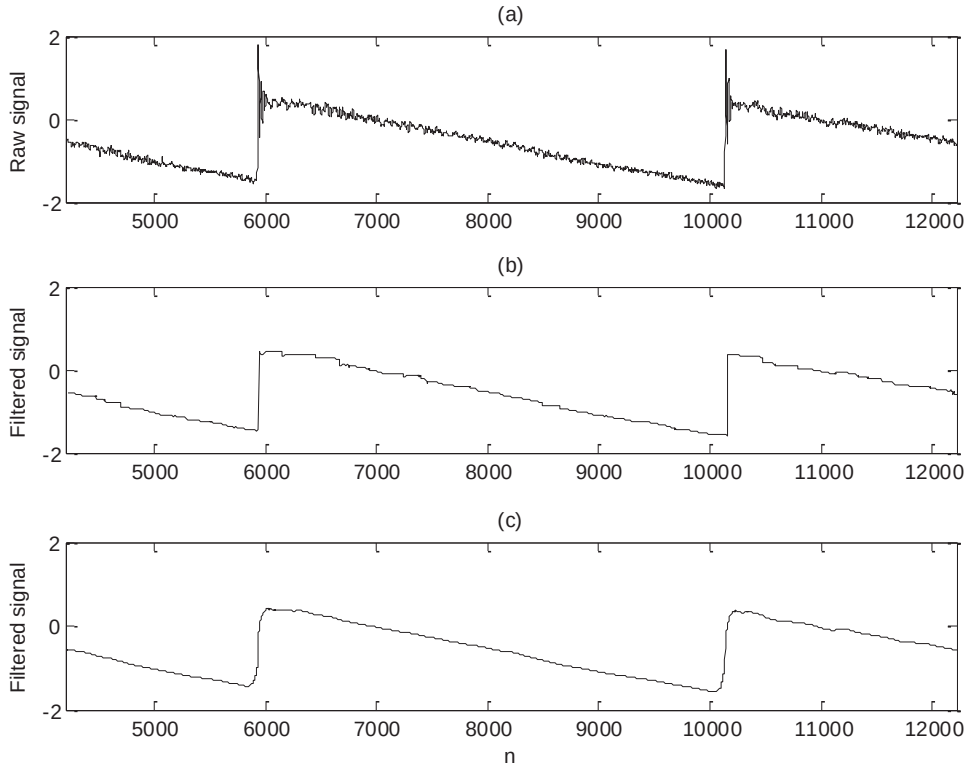


Figure 2-16: Processing results by Myriad filter with different $K$ values: (a) a part of raw SMI signal segmented from the experimental signal in Figure 2-13(a); (b) and (c) are the processing results of using Myriad filters with $K$=0.001 and 1 respectively.

In order to investigate the influence of $K$ on filtering various transient oscillations, let us generate simulated SMI signals containing transient oscillations. As discussed in Section 2.1.3, transient oscillations appear in the form of fast decaying oscillation in SMI signals, which can be featured by amplitude, decay time and oscillation period (frequency). To quantify those features, we defined the following parameters as shown in Figure 2-17: $\mathrm{S}_1$: the amplitude of oscillation; $\mathrm{S}_2$: the amplitude of a clean SMI signal fringe; $\mathrm{T}_{\mathrm{dur}}$: the decay time of oscillation; $\mathrm{F}_{\mathrm{dur}}$: the duration of a single fringe. Then two ratios $\mathrm{R}_1$ and $\mathrm{R}_2$ ($\mathrm{R}_1 = \mathrm{S}_1/\mathrm{S}_2$ and $\mathrm{R}_2 = \mathrm{T}_{\mathrm{dur}}/\mathrm{F}_{\mathrm{dur}}$) are used to describe the intensity and the duration of oscillations respectively. By our knowledge from the experiments and simulations, $\mathrm{R}_1$ is usually in the range of (0, 1) when the system works in stable state. For $\mathrm{R}_2$, although it is practically pointless to give a fixed interval since its value is related to both transient oscillation and target movement, here $\mathrm{R}_2$ is only a variable parameter that used to

investigate the performance of Myriad filter. Nevertheless, a general test interval (0, 1/20) is set for $\mathrm{R}_2$ based on our experience. For a normalized ideal SMI signal $g(n)$, the absolute values of all the data sample should fall in the range of [0, 1]. Thereby, the worth considering range of $K$ should also be inside this range [70].

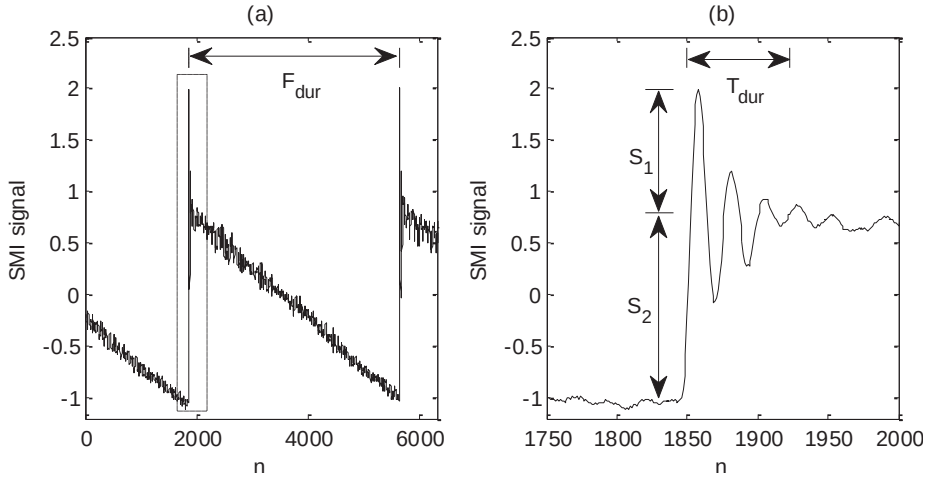


Figure 2-17: Enlarged views for a short segment from the experimental SMI signal shown in Figure 2-3(a).

The SMI signals in the following tests are generated by using the stable-state SMI model described in Equation 1.9-1.11. Meanwhile, in order to adjust $\mathrm{R}_1$ and $\mathrm{R}_2$ flexibly, transient oscillations are approximated by the simple harmonic damped oscillation model in the tests. For determining the optimal value for $K$, the filtering error $E(K)$ is introduced to evaluate the filtering performance, which is defined as:

$$E(K)=\sum_{n=1}^{M}\left[\hat{g}_K(n)-g(n)\right]^2 \tag{2.9}$$

where $M$ is the length of the signal under test. As an example, a piece of SMI signal with additive damped oscillations ($\mathrm{R}_1$=0.6 and $\mathrm{R}_2$=1/50) is generated. By increasing $K$ from 0.001 to 1 with a minimum step of $\Delta K$=0.001, the filtering errors are calculated by using above equation. The relationship between filtering error $E(K)$ and the value of $K$ is plotted in Figure 2-18, where the minimum error is achieved at $K$=0.012 (Figure 2-18(b) provides a better view of the minimum point of $E(K)$ by using logarithmic axes).

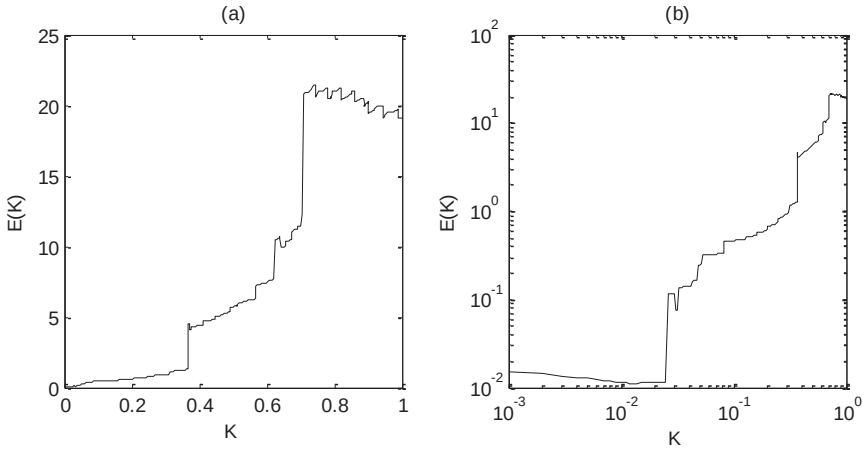


Figure 2-18: Filtering error $E(K)$ vs. $K$ shown in: (a) linear axes; (b) logarithmic axes.

Next, we will investigate if the two ratios $\mathrm{R}_1$ and $\mathrm{R}_2$ influence the optimal $K$ that minimize the filtering error.

First we alter $\mathrm{R}_1$ (oscillation amplitude) and remain $\mathrm{R}_2$ (oscillation duration) fixed ($\mathrm{R}_2$=1/50). In this test, three pieces of SMI signal were generated with $\mathrm{R}_1$= 0.8, 0.6 and 0.45 respectively, and then processed by Myriad filter with difference $K$ settings from 0.001 to 1 (just like in the above example). The correspondences between $E(K)$ and $K$ of the three SMI signals are plotted in Figure 2-19. According to the optimal $K$ values found in this test (are all around 0.01), it can be concluded that the optimal value of $K$ is not affected by $\mathrm{R}_1$.

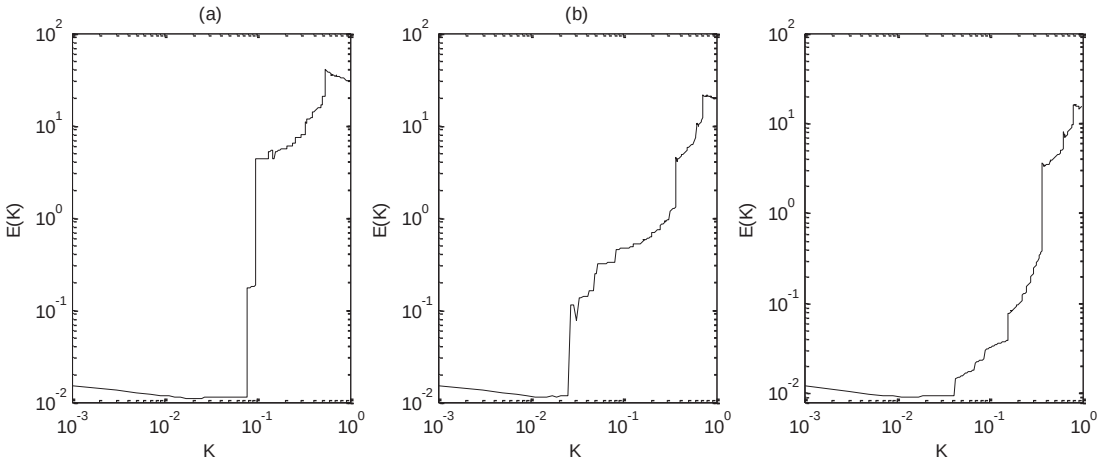


Figure 2-19: Filtering error $E(K)$ vs. $K$ shown in logarithmic axes: (a) $\mathrm{R}_1$= 0.8; (b) $\mathrm{R}_1$= 0.6; (c) $\mathrm{R}_1$= 0.45.

Similarly, in the following simulation, $R_2$ will be adjusted while $R_1$ is fixed to 0.8. The filtering errors for the cases with $R_2$=1/30, 1/50 and 1/70 are plotted in Figure 2-20 respectively. Clearly, the optimal values of $K$ are still around 0.01, which proves $R_2$ can hardly affect $K$.

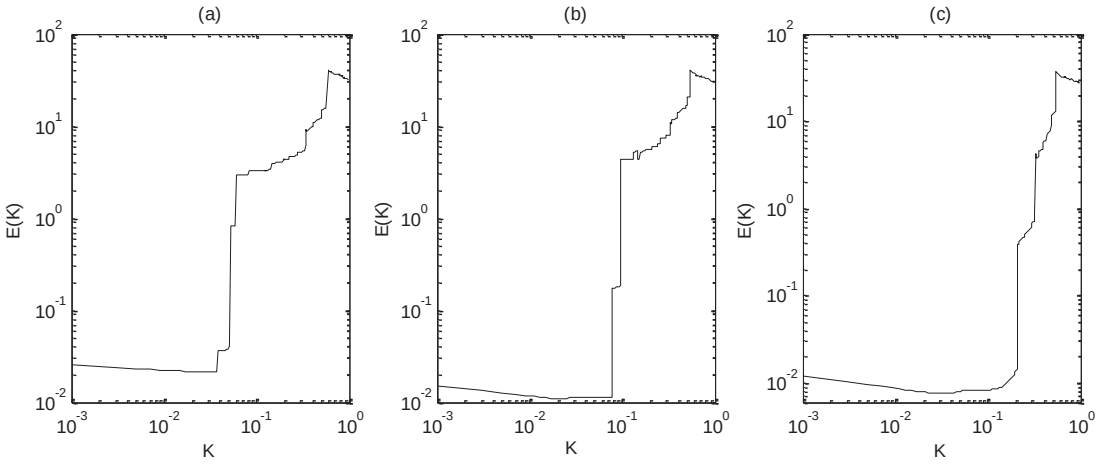


Figure 2-20: Filtering error $E(K)$ vs. $K$ shown in logarithmic axes: (a) $R_2$= 1/30; (b) $R_2$= 1/50; (c) $R_2$= 1/70.

As the simulation results showed in Figure 2-19 and Figure 2-20, the best $K$ values locate within (0.01, 0.04). While there is another important feature in those figures should be noticed, the filtering error $E(K)$ increases significantly at certain point when $K\subset$(0.025, 0.2). Therefore, to avoid the risk of introducing huge filtering error, the smallest value of the best $K$ values should be the most feasible value, i.e. 0.01.

In summary:

1) The features of transient oscillation (amplitude and duration) have negligible impact on the selection of $K$;

2) $K$=0.01 is the most feasible choice for cancelling the transient oscillations in SMI signal with a Myriad filter.

#### 2.3.2.2 Configuration of $N$

Equation 2.8 indicates that the output of a Myriad filter depends on the length and the values of an input sample sequence. Therefore, the window width $N$ (the quantity of input samples) in Myriad filter is another important parameter needs to be carefully determined.

In order to investigate the influence of $N$ on the filtering performance, the same piece of simulated SMI signal is processed by Myriad filter with different window width settings. For a clear demonstration, only one sharp changing part from each result is shown in Figure 2-21. Apparently, the oscillation cannot be completely removed if the window width $N$ is not wide enough. However, an overlarge $N$ can also introduce distortions and leads to considerable computational complexity. Therefore, the selection of $N$ is crucial for both signal quality and processing efficiency.

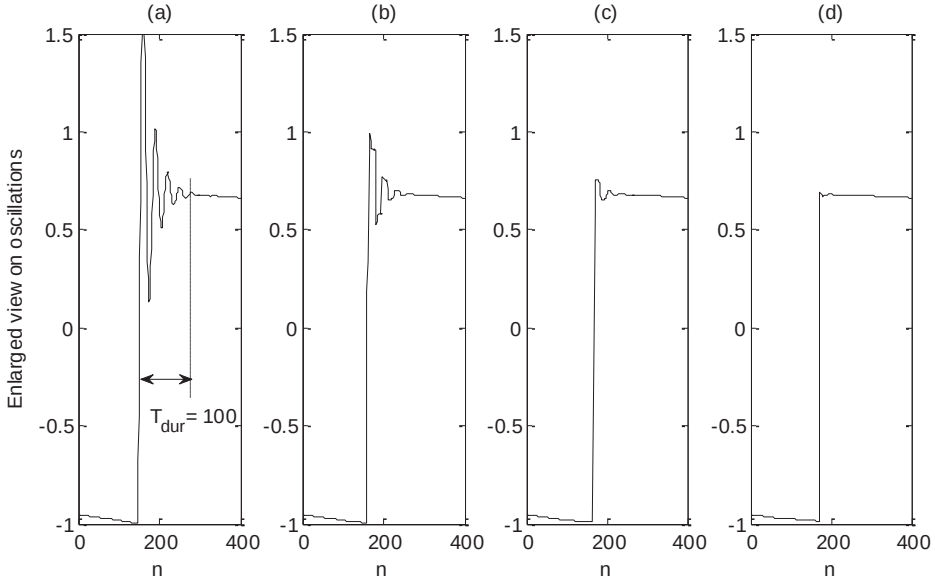


Figure 2-21: Comparison on the filtering results of using Myriad filters with different sizes of window $N$: (a) raw signal with overshooting; (b) $N$=50; (c) $N$=100; (d) $N$=150.

As shown in Figure 2-21(a), the damped oscillation is approximately 100 sample points wide. For the cases when $N$<150, there are still some residual sparkles which suggest $N$ should wider than $\mathrm{T_{dur}}$. However in practice, it is difficult to detect $\mathrm{T_{dur}}$with the existence of all kinds of noise throughout the signal. There is no doubt that the window width can be set

manually by measuring the duration of oscillation, but this kind of manual intervention is not ideal for the automation of signal processing. Here, an iterative method is proposed that adjusting the window width based on filtering results to work out an optimal $N$.

There are two key points in this iteration: the initial value of window width (denoted by $N_0$) and the iterative rule of $N$. Based on our experience, the transient oscillation in SMI signal is worth noticing when its duration is wider than 1/100 of a fringe width $\mathrm{F_{dur}}$, i.e. $\mathrm{R_2}$>1/100. So the initial window width can be simply set to $\mathrm{F_{dur}}$/100, where $\mathrm{F_{dur}}$ is roughly estimated by detecting the interval between two consecutive peaks from a raw SMI signal. That is, dividing a piece of received SMI signal into fringe based segments, and $\mathrm{F_{dur}}$ is the average over the lengths of the segments.

For each iteration, the current window width $N$ should be adjusted according to the filtering results. As indicated by Figure 2-21, a fraction of sparkle will remain if $N$ is not big enough. So the following formula is introduced to assess the flatness of filtering results:

$$\left|\hat{g}(i)-\hat{g}_{ave}\right|<\mathrm{S_2}\cdot 5\%,\ i=m+1,m+2m,...,m+N \tag{2.10}$$

where $\hat{g}_{ave}$ denotes the average value of the filtering results; $\mathrm{S_2}$ is the fringe amplitude; 5% is the threshold which is set based on experience; $m$ is the index of a sharp changing location. If the filtering result does not satisfy the above condition, then update the window width $N$ by 1.2 times of its current value. The iterative process for determining the window width $N$ is summarized in Figure 2-22.

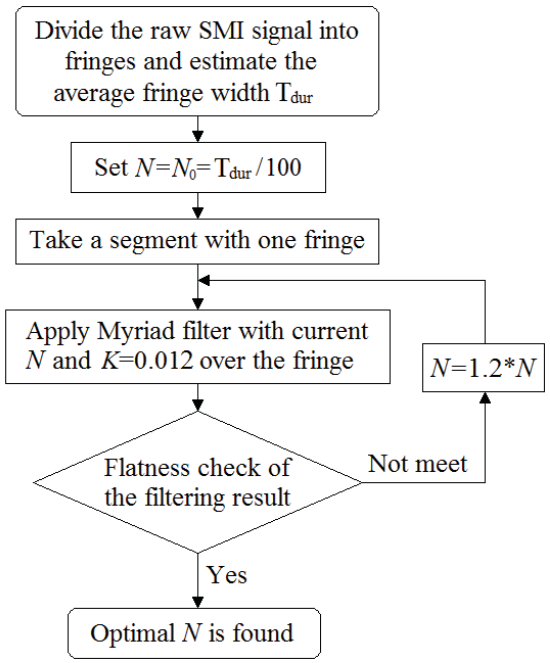


Figure 2-22: Flow chart on determining an optimal window width $N$.

### 2.3.2.3 Delay correction

Most of the existing filters can introduce distortion to the original signal more or less, Myriad filter is no exception. Figure 2-23 gives an example of such issue in Myriad filters, where the sharp edge in the filtering result (indicated by $D_2$) shows a very short delay relative to its original location (indicated by $D_1$).

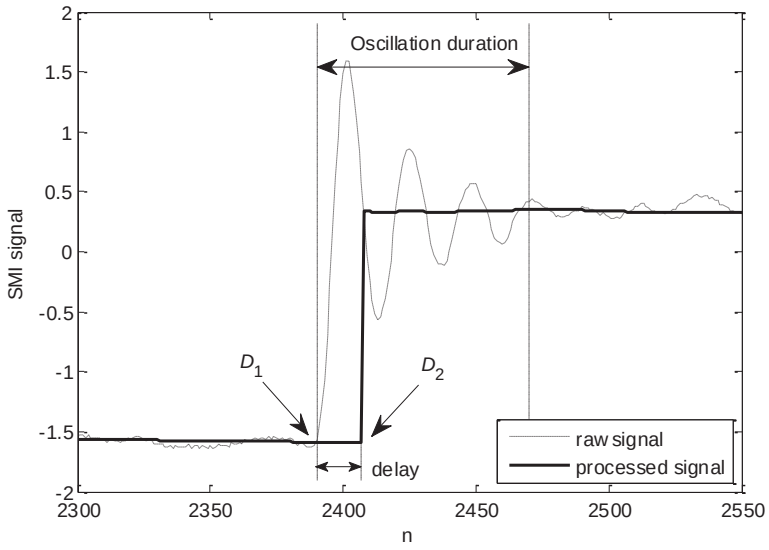


Figure 2-23: Sharp edge delay caused by Myriad filter.

Although the duration of such delay is extremely small compared to a whole fringe, for some particular applications which are sensitive to the locations of characteristic points, e.g. the algorithm in [23] for alpha estimation, this error is not negligible. In order to avoid the error introduced by such delay, a post-processing correction is required.

The key of delay correction is to determine the duration of delay, i.e. the time interval between $D_1$ and $D_2$, that is $|D_1 - D_2|$ in time sequence. $D_2$ can be easily detected by monitoring the differential value of the output signal. While since there is no sharp change in transient oscillations, so $D_1$ cannot be detected in the same way as $D_2$. As demonstrated in Figure 2-23, the oscillation starts from $D_1$ where the raw signal intersects with the filtered signal, which suggests such intersection can be used to determine the location of $D_1$. The procedure of detecting $D_1$ is summarised as follows:

(1) Locate the sharp changing edge in filtered signal $D_2$;

(2) Locate the nearest intersection of the processed signal and the raw signal that ahead of $D_2$;

(3) Calculate the delay duration as $|D_1 - D_2|$.

With the knowledge of delay duration, the original sharp changing edge then can be approximately restored. The most direct way to reconstruct the waveform is using the stable-state value to replace all the values inside the delay interval. Alternatively, the waveform can be generated by curve fitting. Although the latter option is more reasonable from the perspective of mathematical model, there is no guarantee of the fitting performance due to the residual noises. In summary, both solutions are feasible in practice since the delay duration is very short.

### 2.3.3 Adaptive Myriad filter for SMI signal processing

The idea of adaptive Myriad filter was proposed and extensively discussed in the field of robust non-linear filtering, and the main topic is how to assign appropriate values for linear

parameter $K$ and weights for Myriad filters depending on the signal and the features of noise [65,68,69,71-73]. The existing adaptive methods all have very specific area of applications. So far, there is no feasible adaptive algorithm for SMI signal processing. In this section, an adaptive Myriad algorithm is proposed to remove noises from SMI signals.

As mentioned earlier, the objects of filtering SMI signals are removing white noise and transient oscillations. To reduce white noise, Myriad filter is expected to exhibit its linear property, which requires a large $K$. While for removing oscillations, Myriad needs to be highly selective, which requires a very small $K$. An adaptive algorithm for $K$ is desired to solve this contradictory, that is, using a small $K$ to process transient oscillations and using large $K$ values to cancel the rest. The authors in [70] presented a deep discussion regarding the choice of $K$ that how much is large and how much is small, and an empirical method is given: if the values of $K$ on the order of the data range, $K \sim x_{(N)} - x_{(1)}$, the Myriad will reflect linear property and outputs the sample average; while when $K \sim \min_{i \neq j} |x_i - x_j|$, the output of Myriad will become very selective (where $x_{(i)}$ denotes the $i$th-order statistic of the sample sequence $x$). This simple but effective method for $K$ selecting has been accepted and adopted [72]. Unfortunately, this method is based on the assumption that all the samples are under the Cauchy distribution, thereby this approach does not suitable for SMI signals. Nevertheless, it still provides a general idea for designing an adaptive algorithm for $K$, that is: the value of $K$ should depends on the dispersion of input samples. To verify this hypothesis, we define the dispersion of the samples inside the filtering window as:

$$D_{MSN} = \frac{1}{N} \sum_{i=1}^{N} [g(i) - g_{ave}]^2 \tag{2.11}$$

where $N$ is the filtering window width, $g_{ave}$ is the average of all the samples inside the window. According to the requirements, the transient overshooting (high dispersion) should be processed with a very small $K$, and for other part of the waveform that far from the overshooting, a large $K$ is desirable that helps reducing the white-like noise. Therefore, the

adaptive $K$ value (denoted by $K_{adapt}$) should be inversely proportional to $D_{MSE}$, which can be simply described by the following expression:

$$K_{adapt} = \frac{k}{D_{MSE}} \tag{2.12}$$

where $k$ is a coefficient need to be determined. Next, we will specify a suitable value for $k$ through simulations.

In the following simulations are based on an ideal SMI signal (Figure 2-24(a), a segment from Figure 2-9(a)) and an experimental signal (Figure 2-24(b)). By temporarily letting $k = 1$ in the above equation, $K_{adapt}$ of every sample was calculated throughout both signals, the results are shown in Figure 2-24(e) and (f).

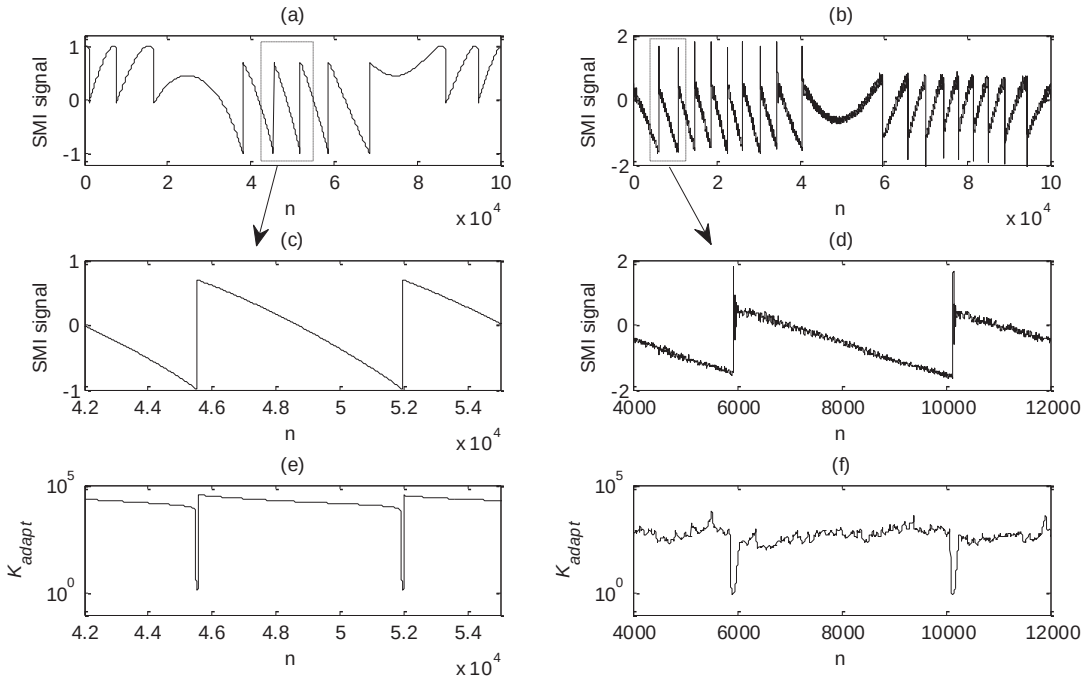


Figure 2-24: SMI signals and their corresponding $K_{adapt}$ throughout the signal: (a) and (b): simulated and experimental SMI signal respectively; (c) and (d): enlarged view for (a) and (b) respectively; (e) and (f) are calculated $K_{adapt}$ of (c) and (d) respectively.

As depicted in Figure 2-24(e) and (f), the locations of sharp changing edges have been clearly indicated through the calculation of Equation 2.11 and 2.12. It is worth noting that, the smallest $K_{adapt}$ in both simulated and experimental signals are all approximately $10^0$ (i.e. 1),

while $K = 0.01$ was found the most desirable value for eliminating transient oscillation (according to Section 2.3.2.1). So by setting coefficient $k$=0.01 in Equation 2.12 will allow $K_{adapt}$ approximating 0.01 around the sharp changing edges. Since $K$=1 is large enough to reduce the white noise and smooth the waveform (as shown in Figure 2-16), thus the final expression for $K_{adapt}$ is:

$$K_{adapt} = \begin{cases} K_{adapt}, & K_{adapt} \leq 1 \\ 1, & K_{adapt} > 1 \end{cases} \tag{2.13}$$

To test the performance of proposed adaptive Myriad filter, the same piece of signal (Figure 2-24(b)) was processed with simple Myriad filter, adaptive Myriad filter and the filter proposed in [52], results are plotted in Figure 2-25 and Figure 2-26.

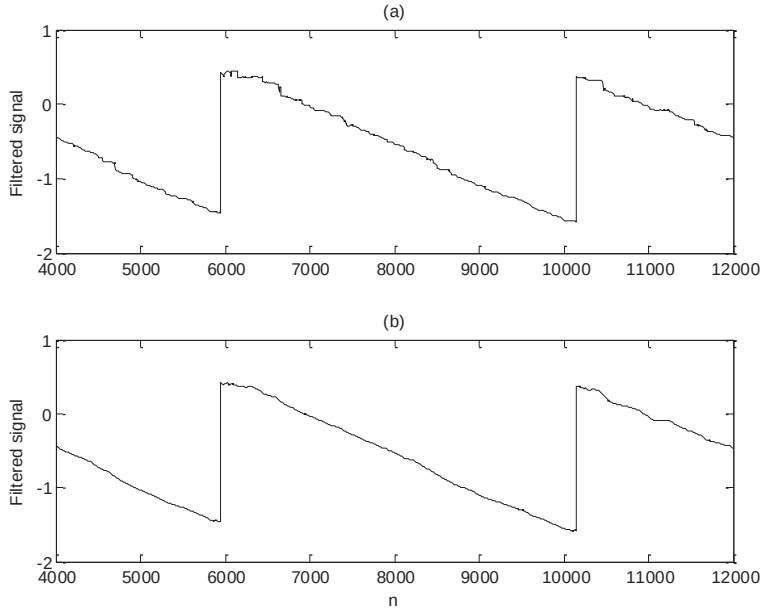


Figure 2-25: Performance comparison between simple Myriad filter and adaptive Myriad filter: (a) processed with fixed $K$=0.01; (b) processed with adaptive $K$.

By comparing the waveforms in Figure 2-25, clearly adaptive Myriad filter yields much better performance on white noise suppression. From Figure 2-26, it can be seen that the two filtered waveforms are almost overlapped except around the sharp changing edge, which suggests the two filtering methods have similar performance on white noise

removal. The difference is that the proposed method removes the oscillation without distorting the sharp edges, while the method in [52] fails.

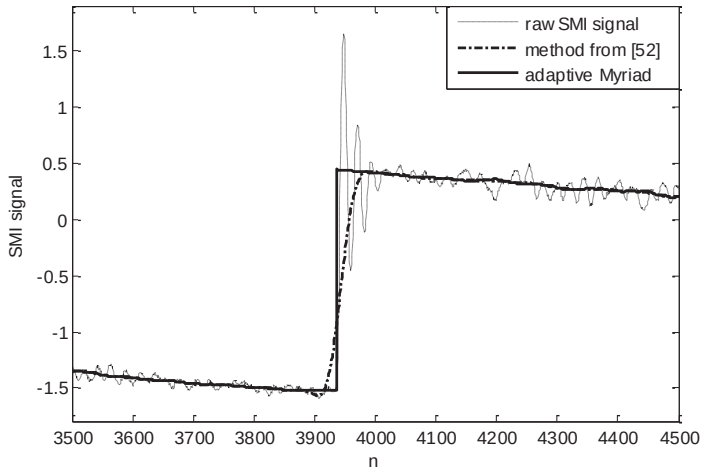


Figure 2-26: Performance comparison between adaptive Myriad filter and the filtering method from [52].

In order to verify the performance of the proposed filtering method in practical applications, the measurement of $\alpha$ using the algorithm presented in [23] is used as a validating method which is sensitive to the quality of SMI signals.

According to the $\alpha$ estimation algorithm in [23], each target vibration period can generate 1~3 values of $\alpha$ depending on the number of fringes. For the experimental SMI signal partially shown in Figure 2-24(b), it contains 7 vibration periods and from which, 21 estimation results can be obtained in total. Both the proposed filtering method and the one in [52] were employed to process this piece of signal. Then the filtered signals were fed into the algorithm in [23] for $\alpha$ estimation. The average value and the mean squared error (MSE) of the estimation results are reported in Table 2-1. It can be seen that the results estimated from the signal processed by the proposed method are characterized by better accuracy than that from the approach in [52]. Although the average results from the two approaches are different, as the proposed method leads to less distortions to the original SMI waveform, it is expected that our result (4.36) is more reliable and closer to the true value of $\alpha$ than that from [52].

Table 2-1: Estimation results of $\alpha$.

| *Filtering method* | *Average value* ( $\hat{\alpha}$ ) | *MSE* (1/n $\sum(\alpha-\hat{\alpha})^2$) |
|---|---|---|
| Method in [52] | 4.81 | 0.31 |
| Proposed method | 4.36 | 0.06 |

## 2.4 Summary

This chapter is focused on acquiring a clear SMI signal. Firstly, an overview is given on the features of experimental SMI signals and the noises contained in the signal. Then, the influence of noises on measurements are evaluated, which followed by the possible solutions for reducing the noises. Finally, a new filtering technique based on Myriad algorithm is proposed specially for SMI signal processing, which can effectively eliminate the transient oscillation while preserve the waveform of SMI signals.

# Chapter 3. Error analysis and optimization on frequency-domain based alpha measurement

The alpha factor ($\alpha$) is a fundamental LD parameter that characterises LDs in terms of the linewidth, modulation response, injection locking, and the response to external optical feedback [3]. Therefore, it is of significant interest to know the value of this parameter since the knowledge of alpha is required both for SMI system analysis and design. Among the existing measuring method of alpha factor, the frequency domain based approach is highly promising since it has the advantages of high precision and wide feedback level applicable range [25]. However, the measurement performance can be severely degraded due to the noises contained in the signal. Although the quality of an SMI signal can be improved by pre-processing techniques (e.g. the adaptive Myriad filter presented in Chapter 2), the influence of the noises cannot be eliminated completely. Therefore, it is important to optimize the calculation process thus avoid error propagation and minimize the influence of noises on estimation accuracy.

This chapter is organised as follows. Firstly, the four stages of the frequency-domain based $\alpha$ measurement method are reviewed in Section 3.1. Then, for each stage, a detail analysis on the introduced error is provided. Finally, from the analysis, a series of optimization methods are proposed for preventing error propagation during the calculation and the effectiveness of proposed methods will be verified through simulations.

## 3.1 Method review

The frequency domain method proposed in [25] has been introduced in Chapter 1. In this section, a brief review is provided that gradually leads to the following sections of error analysis and optimization. The frequency domain method is capable of measuring both optical feedback parameter $C$ and $\alpha$ simultaneously with SMI signals. The values of $C$ and $\alpha$

are estimated from the spectrum of the feedback phase which is extracted from an SMI signal.

For illustration convenience, the SMI model equations are relisted below:

$$\phi_F(n) = \phi_0(n) - C \cdot \sin(\phi_F(n) + \arctan\alpha) \tag{3.1}$$

$$g(n) = \cos(\phi_F(n)) \tag{3.2}$$

$$P(n) = P_0(1 + m \cdot g(n)) \tag{3.3}$$

By expanding the sine component, Equation 3.1 becomes:

$$\phi_F(n) = \phi_0(n) + k_1\phi_1(n) + k_2\phi_2(n) \tag{3.4}$$

where $\phi_1(n) = \sin[\phi_F(n)]$, $\phi_2(n) = \cos[\phi_F(n)]$, $k_1 = C/\sqrt{1+\alpha^2}$, $k_2 = \alpha \cdot C/\sqrt{1+\alpha^2}$. Then by taking Fourier transform of the above equation, phase equation in frequency domain is obtained as:

$$\Phi_F(f) = \Phi_0(f) + k_1\Phi_1(f) + k_2\Phi_2(f) \tag{3.5}$$

If target is in harmonic vibration with a frequency of $f_0$, by choosing $f \gg f_0$, the frequency component of $\Phi_0(f)$ can be excluded from above equation, then we have:

$$\Phi_F(f) = k_1\Phi_1(f) + k_2\Phi_2(f), \ f \subset \Omega \tag{3.6}$$

where $\Omega$ denotes the frequency range which starts from $\Phi_0 \approx 0$ and ends at $\Phi_F = 0$. The authors in [25] gave an approximate range that $f \subset (15f_0, 125f_0)$ based on experience. Since $\Phi_F(f)$, $\Phi_1(f)$ and $\Phi_2(f)$ are all complex functions that consist of real and imaginary components, Equation 3.6 can be separated as:

$$\begin{cases} \Phi_F^R(f) = k_1\Phi_1^R(f) + k_2\Phi_2^R(f) \\ \Phi_F^I(f) = k_1\Phi_1^I(f) + k_2\Phi_2^I(f) \end{cases}, \ f \subset \Omega \tag{3.7}$$

where superscripts "$R$" and "$I$" denote the real and imaginary parts of the relevant complex numbers (e.g. $\Phi_F(f) = \Phi_F^R(f) + j\Phi_F^I(f)$). In this case, expect for $k_1$ and $k_2$, all the component are known constants at a certain frequency component. Then, each frequency component inside frequency range $\Omega$ can be used to worked out a pair of $k_1$ and $k_2$.

Finally, $\alpha$ and $C$ can be estimated by using the values of $k_1$ and $k_2$, and calculated as follows:

$$\alpha = \frac{k_2}{k_1}, C = \sqrt{k_1^2 + k_2^2} \tag{3.8}$$

Theoretically, the estimation results of $k_1$ and $k_2$ using each frequency component inside range $\Omega$ should be identical. While in practice, their values often deviate from the true values due to the influence of various noises and the error introduced in signal processing.

The procedures of the frequency domain based alpha estimation algorithm are summarised as follows:

1) Normalisation: normalise the raw SMI signal into the range of [-1, 1], so that the phase can be extracted from SMI signal by performing inverse-cosine transform (Equation 3.2);

2) Phase unwrapping: reconstruct the feedback phase based on the method in [51];

3) Spectrum calculation: generate the spectrum of phase signals by performing FFT (fast Fourier transform);

4) Optimization of results: select the optimal value based on the processing results.

In the following sections, we will investigate the errors at each stage caused by noises and signal processing, from which, corresponding optimization methods are proposed to minimize the errors.

## 3.2 Error analysis and optimization

### 3.2.1 Normalization

For a SMI signal in standard model, the values of all the data sample should fall in the range of [-1, 1], while the signals acquired from the experimental setup in practice are unlikely to fit in this range perfectly. Therefore, for most of the high precision applications which involve calculations based on phase signals (e.g. alpha factor measurement [23-25,43,49] and target movement reconstruction [44,51,59,74]), a normalization process is required in

signal pre-processing stage before further calculations can be done. However, in practice, it is difficult to accurately determine the true boundaries (upper limit and lower limit) of an SMI signal duo to the noises, which can result distortions during the normalization process. Despite a variety of signal pre-processing and filtering methods were proposed to improve signal quality, the enhancement on the accuracy of normalization has barely been investigated.

In this section, an optimized normalization process with the assistance of the frequency domain based alpha estimation is presented. Firstly, the influence of normalization on the performance of alpha estimation is investigated through simulations. Then, by analysing the results of simulations, a novel method was proposed to improve the accuracy of normalization and thus enhance the performance of SMI based sensing.

As discussed in Chapter 2, due to the various noises contained in the experimental system, which cause SMI signals featured in time domain with transients and slow-time fluctuation, as shown in Figure 3-1. Since acquired experimental SMI signals are not fitting in the range of [-1, 1], a normalization process is required. However, unlike ideal signals, the peak points in an experimental signal are usually not in the same horizontal level (e.g. the peak points in Figure 3-1), as well as the valley points.

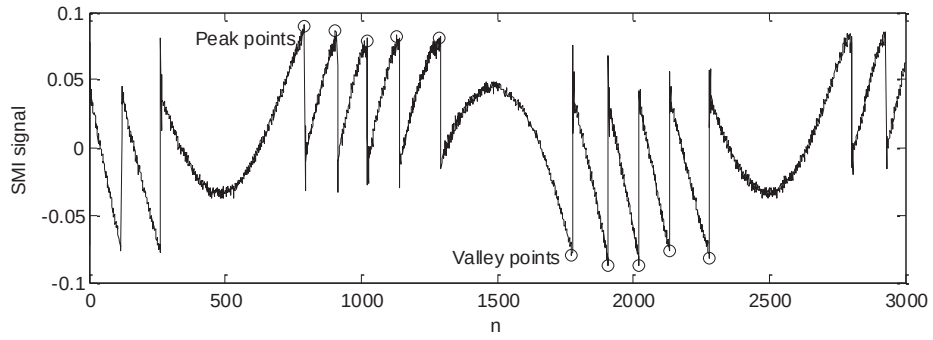


Figure 3-1: An experimental SMI signal obtained at moderate feedback with an external target in harmonic vibration.

In this case, simply setting the maximum value (or minimum) value as the upper limit (or lower limit) will introduce massive error during the normalization process, which then will be

passed on to the next procedure: phase unwrapping. To demonstrate the consequences of normalization error, the phase signal unwrapped from an improperly normalized SMI signal is given in Figure 3-2. By comparing the unwrapped phase with the true phase signal in Figure 3-2(b), it is clear that the error produced by normalization has been passed on. Although according to Figure 3-2(a) that most of samples in unwrapped result are accurate, actually this minor error is not negligible for alpha estimation, which will be demonstrated in the following section.

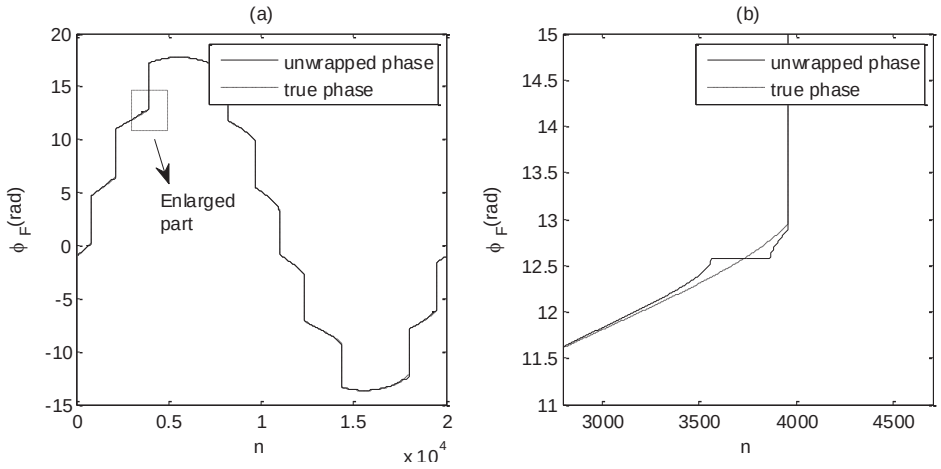


Figure 3-2: (a) Noise affection on phase unwrapping; (b) an enlarged view on the part indicated in (a).

### 3.2.1.1 Error analysis on normalization process

As required by the frequency domain based alpha estimation algorithm, extracting phase signal $\phi_F(n)$ from the SMI signal $g(n)$ is the first step. If $g(n)$ is already distorted due to an inaccurate normalization, the error can be passed on or even be amplified throughout the calculations. In order to find out the influence of normalizing error on the performance of alpha estimation, a simulated SMI signal (with the boundary of [-1, 1]) was shifted upwards (or can be considered as the signal boundaries were shifted downwards) by 2% of its range (i.e. 0.04) to simulate a normalization process with error. Then the frequency domain based alpha measurement algorithm was applied for alpha estimation, the results are plotted in Figure 3-3(b). For comparison, the results calculated from the ideal signal are also given in

Figure 3-3(a). Remarkably, only 2% normalization error has caused considerable disturbance to the estimation results: for the ideal signal, the alpha results are identical at each frequency component in Figure 3-3(a) (coincide with the true value of $\alpha$=2.5); in contrast, the results in Figure 3-3(b) exhibit a large dispersion in the estimated results of $\alpha$, which indicates a poor measurement accuracy.

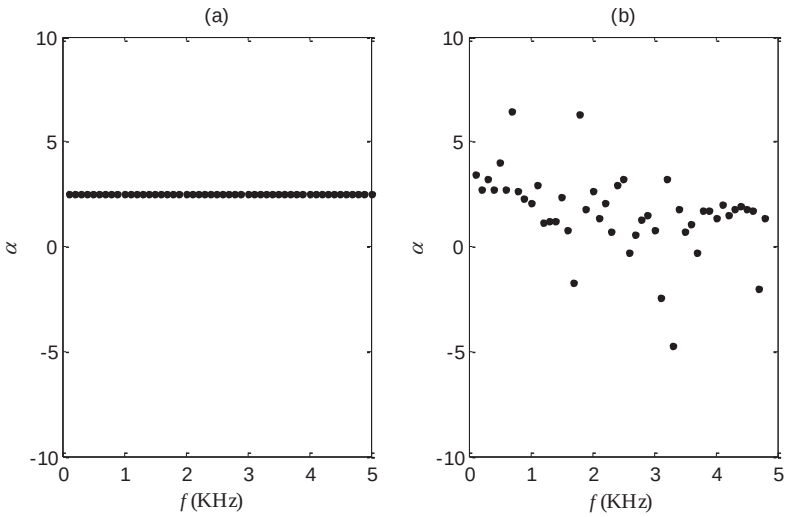


Figure 3-3: Alpha results estimated from: (a) an ideal SMI signal; (b) the signal with normalization error.

In practice, it is very hard to have both upper limit and lower limit (denoted by $L_{upper}$ and $L_{lower}$ respectively) set accurately in normalization. It is common that one of the limits is set deviated from its true value, and we call it an inaccurate setting of the limit. In order to investigate the influence of inaccurate limit setting on the measurement results, the following two cases were tested:

Case 1: Supposing the upper limit is accurate, observe the influence of inaccurate setting in lower limit by varying $L_{lower}$ from -4% to 4% with step of 0.5%;

Case 2: Supposing the lower limit is accurate, observe the influence of inaccurate setting in upper limit by varying $L_{upper}$ from -4% to 4% with step of 0.5%;

To quantify the dispersion of estimated results, mean square error (MSE) was adopted to assess each set of the results, which is calculated as:

$$MSE(\alpha) = \frac{1}{N}\sum_{n=1}^{N}[\alpha(n) - \alpha_{ave}]^2 \tag{3.9}$$

where $N$ and $\alpha_{ave}$ are the length and average value of sequence $\alpha$ respectively. Figure 3-4 gives the correspondences between limit deviation and MSE of the estimation results in above two cases.

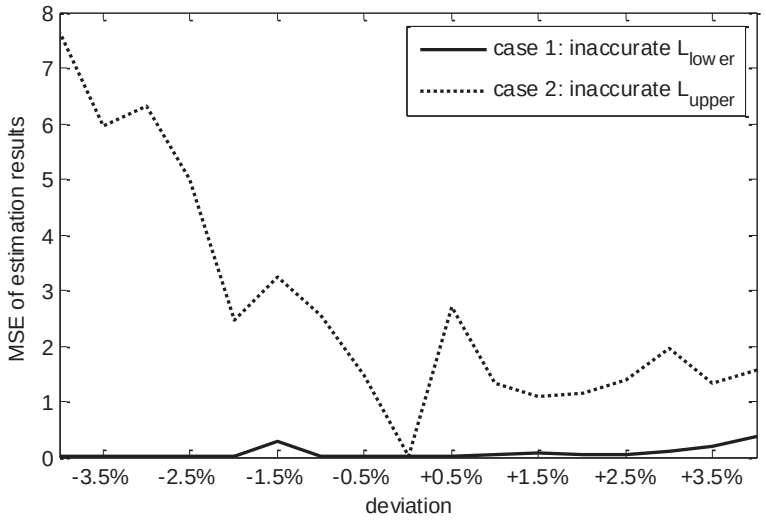


Figure 3-4: Correspondence between limit deviation and MSE of estimation results.

Two conclusions can be drawn from above tests:

1) The lower limit setting has nearly no influence on alpha estimation, but upper limit has very strong influence on the estimation;

2) The more error introduced by normalization, the more dispersive the alpha estimation results will be.

#### 3.2.1.2 Proposed normalization method

Based on the Conclusion 2 above, the accuracy of normalization is reflected in the dispersion of alpha estimation results. That is, the extent of dispersion can be referenced to verify the accuracy of normalization. Moreover, according to the Conclusion 1, since the lower limit has negligible impact on estimation results, instead of blindly adjusting both signal boundaries simultaneously, the lower limit can be roughly set at first, then by simply

adjusting the upper limit and comparing the alpha estimation results, the best value for upper limit in normalization can be found. The optimized normalization process is summarised below:

Step 1: Pick a piece of SMI signal which has the minimum fluctuations on the values of peak points and valley points, and then segment one target vibration period of waveform;

Step 2: Set the minimum value of the valley points as the lower limit;

Step 3: Set the average value of the peak points as the reference upper limit value;

Step 4: Deviate the upper limit from the reference value with a step of 0.5%, from -4% to +4%, record the MSE of estimated alpha values at each step;

Step 5: Find out the optimal value for upper limit by corresponding to the minimum MSE of alpha, and normalize the SMI signal with this limit.

#### 3.2.1.3 Test on experimental signal

In order to test the feasibility of the proposed normalizing method in practice, we applied the proposed method on the same piece of experimental signal where the waveform in Figure 3-1 was segmented from. Figure 3-5 gives the result of MSE vs. adjustment amount which is calculated at Step 4. As expected, the dispersion of estimation results reaches a bottom when the upper limit is adjusted with certain amount (-1% in this case), which means the actual upper limit of this SMI signal has been found

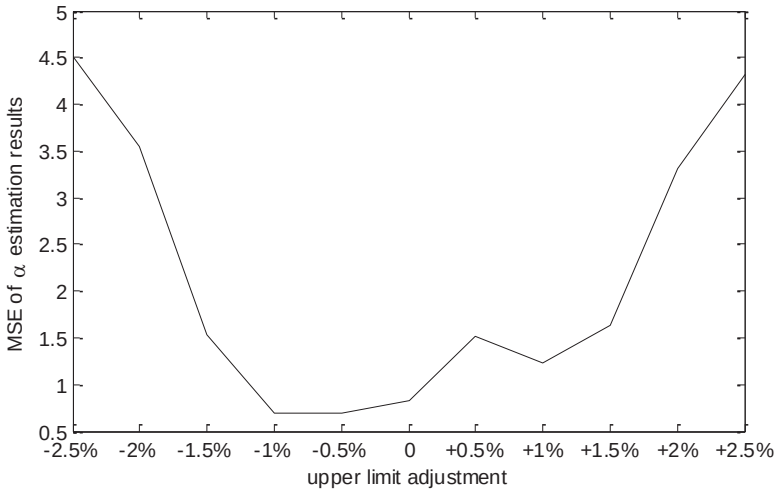


Figure 3-5: Correspondence between upper limit adjustment and MSE of estimation results.

In summary, the proposed normalization method is based on the fact that the results of alpha estimation are highly sensitive to signal quality. By analysing the correspondence between the dispersion of alpha estimation results and the positions of signal limits, the true signal limits can be worked out thus improves the accuracy of normalization. The feasibility of proposed method has been verified through test on experimental signals. However, noise is another important factor that affects signal quality besides signal limit settings. Therefore, the proposed method only works on properly filtered signals where noise is no longer the prior concern.

### 3.2.2 Phase unwrapping

The idea of phase unwrapping was firstly introduced to enhance the resolution of displacement measurement [51,59,74]. Before that, the resolution of the measurement using fringe counting is limited to half-wavelength, which is based on the fact that each fringe in SMI signal indicates a half-wavelength shift of target movement [54]. In [51], the authors proposed a high-accuracy phase unwrapping method that prevents the errors exist in [75] and [76].

Firstly, the principle of PUM (phase unwrapping method) is reviewed. For illustration purpose, a piece of simulated ideal SMI signal ($\alpha$=2.5 and $C$=3) is plotted in Figure 3-6.

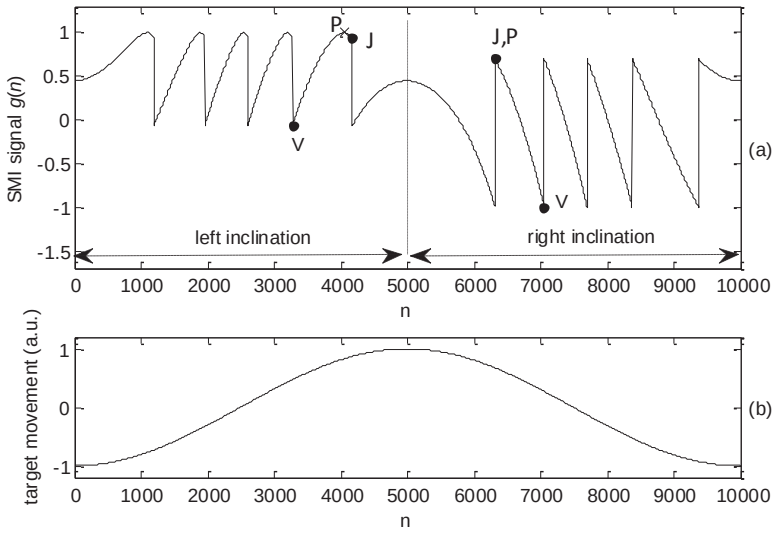


Figure 3-6: A simulated SMI signal and the corresponding target movement.

In Figure 3-6(a), characteristic points V and P indicate the valley and peak of a fringe respectively, and J is the sharp changing edge of a fringe. Because of the hysteresis phenomenon [46,54], P and J are overlapped in the right inclination.

When the system is in weak feedback regime ($C$<1), there is no hysteresis effect and the phase is calculated as:

$$\phi_F(n) = (-1)^{i_{VP}} \arccos[g(n)] \tag{3.10}$$

When the system is in moderate feedback regime, for the waveform in right inclination, the phase is calculated as:

$$\phi_F(n) = (-1)^{i_{VP}} \arccos[g(n)] + 2\pi(i_V + 1) \tag{3.11}$$

For the waveform in left inclination, the phase is calculated as:

$$\begin{cases} \phi_F(n) = -\arccos[g(n)] + 2\pi i_V, \text{ for VP and PV part} \\ \phi_F(n) = +\arccos[g(n)] + 2\pi i_J, \text{ for PJ part} \end{cases} \tag{3.12}$$

Where $i_{VP}$ $i_V$ and $i_J$ are updated as:

$i_{VP} = i_{VP} + 1$, when at P points or V points

$i_V = i_V - 1$, when at V points in right inclination

$i_V = i_V + 1$, when at V points in left inclination

$i_J = i_J + 1$, when at J points in left inclination

The rough PUM recorded in [75] and [76] ignores the particularity of the PJ part, so the obtained phase signal is not suitable for high-precision displacement reconstruction and SL parameter estimations (e.g. alpha factor).

An important source of phase unwrapping error is the uneven fringe peaks in SMI signals. In Figure 3-7, two segments from the same piece of experimental SMI signal are plotted. Compared to Figure 3-7(b), the fringe peaks of the waveform in Figure 3-7(a) are more scattered due to the stronger slow-time noises. Then both signals were pre-processed by the proposed adaptive Myriad filter and the optimized normalisation process, their alpha estimation results are plotted in Figure 3-8. Apparently, the estimation results of the signal in Figure 3-8(b) are more stable and concentrate which yield to more accurate alpha estimation.

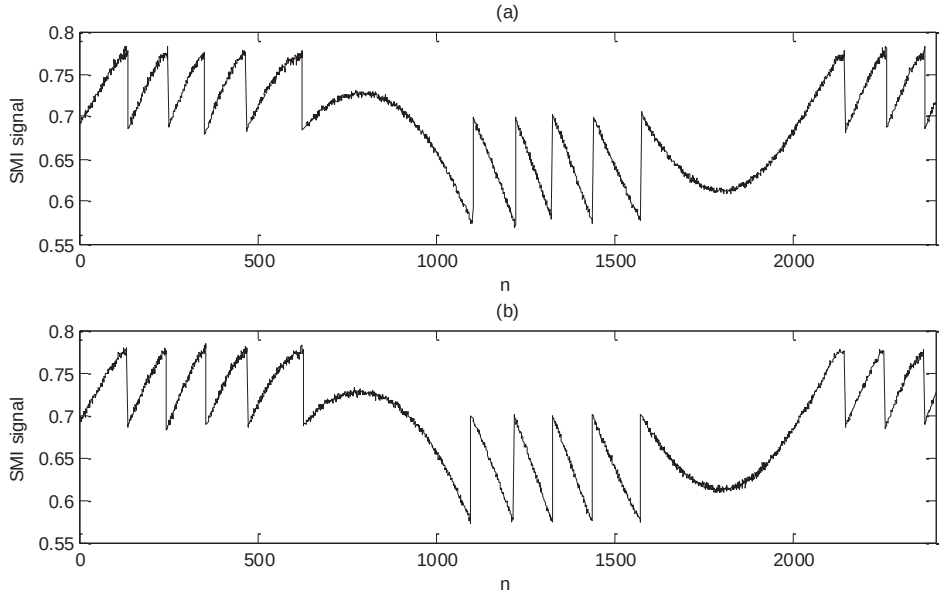


Figure 3-7: Two segments from the same piece of experimental SMI signal.

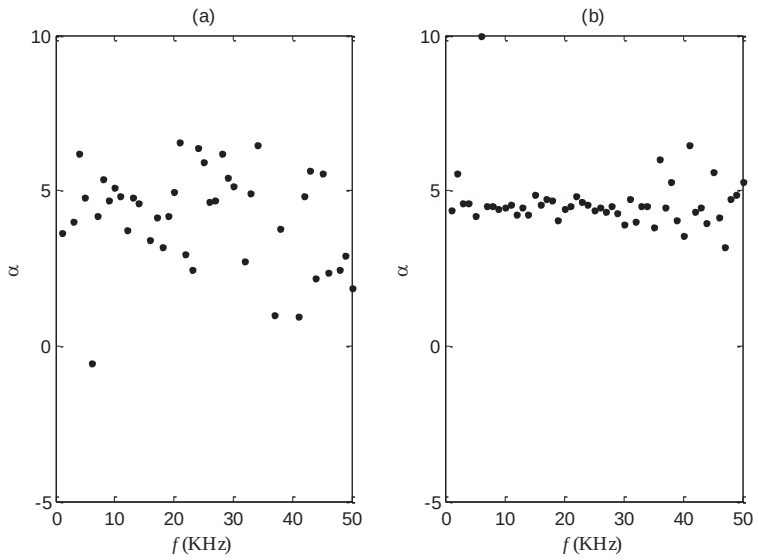


Figure 3-8: Alpha estimation results of the signal in: (a) Figure 3-7(a); (b) Figure 3-7(b).

As discussed earlier in Section 3.2.1, in most cases, the fringe peaks in acquired SMI signals are not even. Even with the proposed pre-processing techniques, the uneven peaks still can cause serious performance degradation, as demonstrated in Figure 3-8. Therefore, choosing a high quality signal (without obvious uneven peaks and severe noises/distortions) is the premise of achieving accurate alpha estimations.

### 3.2.3 Period detection and spectrum calculation

As required by the principle of frequency domain based alpha measurement algorithm, the external target is subject to a simple harmonic vibration which makes $\phi_0$ close to a sinusoidal signal. Hence, $\phi_0$ has the expression of:

$$\phi_0(t) = \frac{4\pi\Delta L_0}{\lambda_0}\sin(2\pi f_0 t) \tag{3.13}$$

where $\Delta L_0$ and $f_0$ are vibration amplitude and vibration frequency of the target. Then, by substituting into SMI model equations (Equation 3.1 and 3.2), we have:

$$\phi_F(t) = \phi_0(t) + C\cdot\sin(k) - C\cdot\sin(\phi_F(t)+k) \tag{3.14}$$

$$g(t) = \cos(\phi_F(t)) \tag{3.15}$$

It is seen from above equations that the target vibration frequency $f_0$ is also the fundamental frequency of $g(t)$.

There are two objectives to achieve the target vibration period (or frequency). One is for excluding the frequency component of $\Phi_0(f)$ from the FFT results (Equation 3.5), which requires the general knowledge of frequency interval that allow$\Phi_0(f) \approx 0$ and $\Phi_F(f) \neq 0$, i.e. $f \subset (15f_0, 125f_0)$. Another purpose is for spectrum calculation (FFT), which strictly requires the input sequence duration is an integer multiple of the target vibration period, otherwise, serious error can be caused by spectral leakage during the FFT.

#### 3.2.3.1 Error analysis on period detection

According to the principle of discrete Fourier transform, the observed data sequence will be extended periodically during the calculation. If a signal with frequencies is not periodic in the observation window, the periodic extension of that signal will not commensurate with its natural period thus can exhibits discontinuities at the boundaries of the observation, which are responsible for the spectral leakage [77]. For SMI signal processing, in order to achieve high quality spectrum for alpha estimation, it is of significant importance to ensure the length of input signal sequence is exactly equal to the target vibration period.

To investigate the impact of period detection error on alpha estimation using frequency domain based method, we conducted a series of tests on ideal simulated SMI signals. In practice, the detected period can be larger or smaller than the true value, therefore, we simulated both circumstances separately. For a clear demonstration of simulation results, the cases for period detection error = 0.1%, 0.5% and 1% respectively, are chosen and plotted in Figure 3-9.

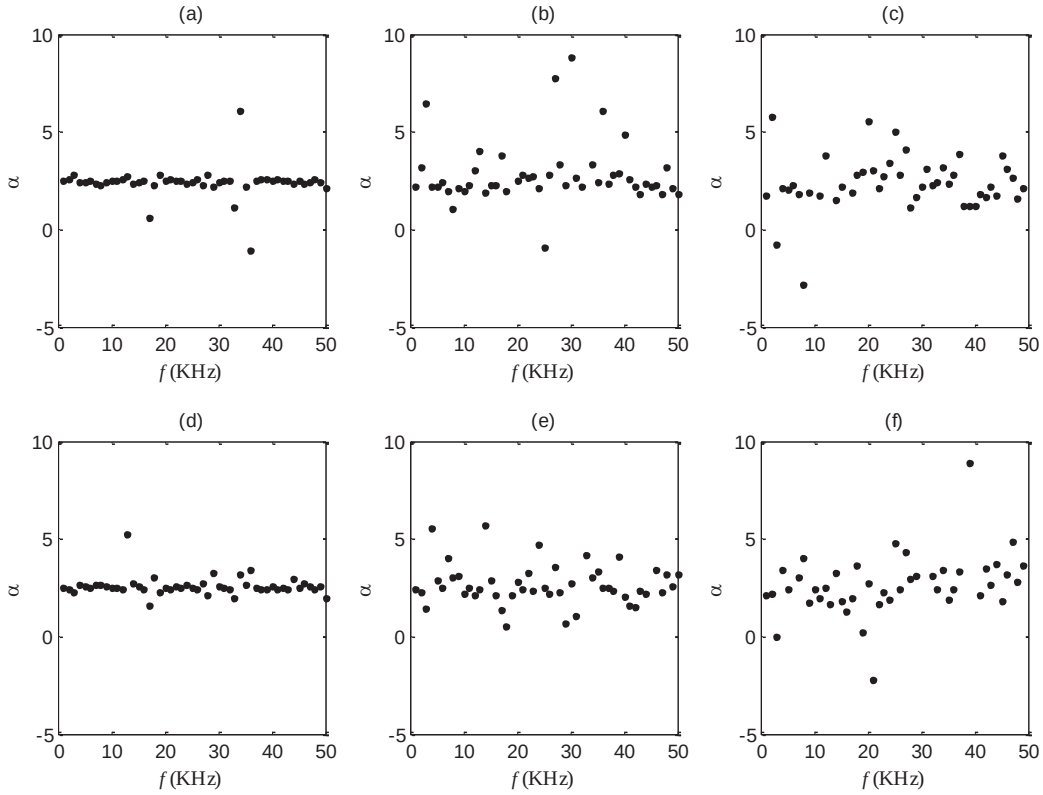


Figure 3-9: Estimation results of alpha for SMI signals with different period detection errors: (a) +0.1% error; (b) +0.5% error; (c) +1% error; (d) -0.1% error; (e) -0.5% error; (f) -1% error.

As demonstrated by Figure 3-9, the reliability of frequency domain based alpha estimation is closely related to the accuracy of period detection. It can be seen in Figure 3-9(a) and (d), even 0.1% period detection error already caused considerable errors in few frequency components. Fortunately, most of the results in Figure 3-9(a) and (d) exhibit very low fluctuations, thus accurate value of alpha still can be achieved via result optimisation processing. But for bigger period detection errors like 0.5% and 1% in Figure 3-9(b) (c) and (e) (f), the estimation results in most of the frequency components are not acceptable, so no matter how we improve other procedures in alpha estimation algorithm, the accuracy and reliability of alpha measurement most be poor.

#### 3.2.3.2 Optimization on period detection

In [43], the authors proposed to acquire target vibration period using the auto-correlation, which has the following expression:

$$r_{ac}(m) = \frac{1}{N} \sum_{n=0}^{N-1-m} g_N(n) \cdot g_N(n+m) \tag{3.16}$$

where $N$ is the data length of SMI signal segment $g_N(n)$ under test. $m$ is time delay which varies from $-(N-1)/2$ to $(N-1)/2$. An example of SMI signals (period is approximately 1000 sample points) and its corresponding auto-correlation result is given in Figure 3-10.

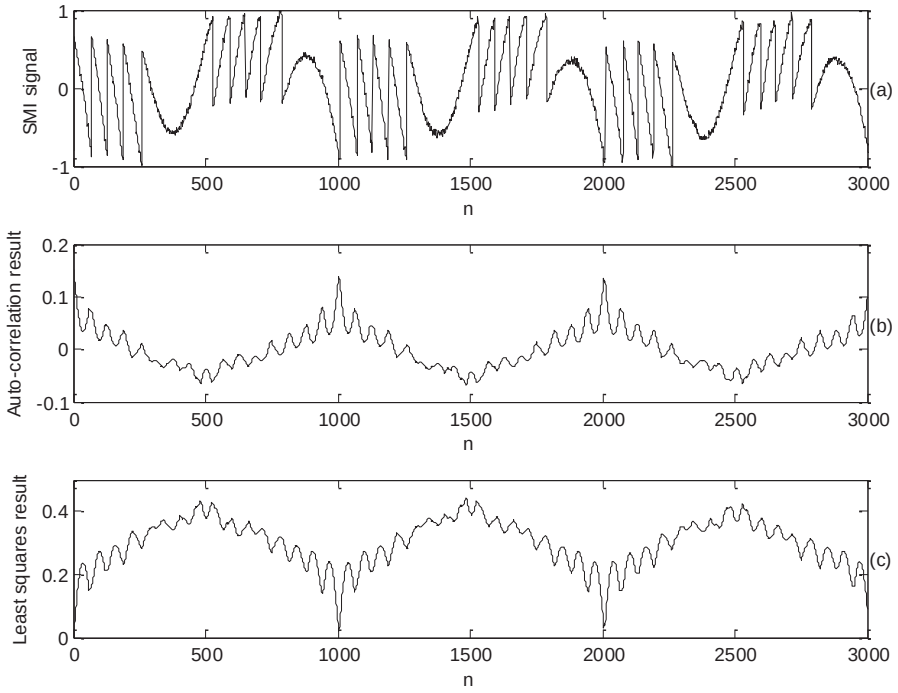


Figure 3-10: (a) A piece of experimental SMI signal; (b) period detection with auto-correlation; (c) period detection with least square.

Similarly, we also can use the least square approach to acquire repeatability which has the following expression:

$$r_{ls}(m) = \frac{1}{N} \sum_{n=0}^{N-1-m} \left[ g_N(n) - g_N(n+m) \right]^2 \tag{3.17}$$

The calculation result of using least square is plotted in Figure 3-10(c). Clearly, the fundamental period can be obtained by detecting the intervals of the peaks or valleys in either auto-correlation result or least square result.

So far, it seems no difficulties in period detections, but it is important to aware the detection error must be controlled less than 0.1%, e.g. only 1 sample point of error is allowed for the

signal in Figure 3-10. To investigate the accuracy of our period detection approaches, we applied auto-correlation and the least square method onto a piece of long experimental signal (contains more than 20 fundamental periods). The period detection results are plotted in Figure 3-11.

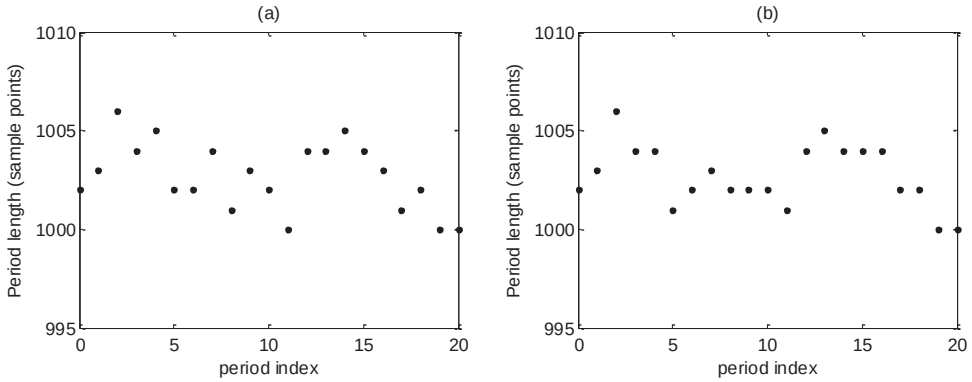


Figure 3-11: Period detecting results calculated by (a) auto-correlation; (b) least square method.

By comparing the results obtained by two different detection approaches, we can say they have similar accuracy, both around 0.3%.

To achieve a detection error less than 0.1%, an optimal value should be selected based on the period detection results, which requires a very long piece of signal. In this way, the error caused by a single period detection is minimized. Based on this idea, we propose the following procedure of period detection:

1) Acquire a piece of SMI signal long enough for period detection, which should contain dozens of fundamental period;

2) Apply auto-correlation or the least square method, and record the durations of peak interval;

3) Apply Myriad estimator (illustrated in Section 2.3) to obtain the most repeated value as the final detection result.

### 3.2.4 Optimization of estimation results

As mentioned earlier, in ideal circumstances, the estimation results of $k_1$ and $k_2$ at each frequency component should be identical. However, due to the interference of all kinds of noise and the errors involved in signal processing, the estimation results deviate from the true values more or less (e.g. Figure 3-3 in Section 3.2.1 and Figure 3-8 in Section 3.2.2).

In previous chapter and sections, we already discussed how to enhance the quality of SMI signals and how to avoid introducing error during the signal processing. Even though, the noise residual still can cause considerable errors during the calculation. In order to investigate the influence of such error and find a way to diminish it, a simulated noisy SMI signal is generated for the test on alpha estimation. To make the noises more realistic, the simulated ideal signal is contaminated with both white noise and slow-time noises. The simulated target movement and the corresponding SMI signal are given in Figure 3-12 with discrete time index ($L$=0.45$m$, $\Delta L$=1.4$\lambda_0$, $f$ =100Hz, $\alpha$=4.5, $C$=4.5).

By applying the frequency domain based alpha measurement algorithm, the true values of $k_1$ and $k_2$ for the above simulated SMI signal are calculated as -0.976 and -4.393 respectively. After sequentially processed through adaptive Myriad filter, normalisation, phase unwrapping, period detection and spectrum calculation, the results of $k_1$ and $k_2$ are obtained, which lead to the results of alpha factor ($\alpha$) and optical feedback parameter ($C$) by using Equation 3.8. The estimation results are plotted in Figure 3-13.

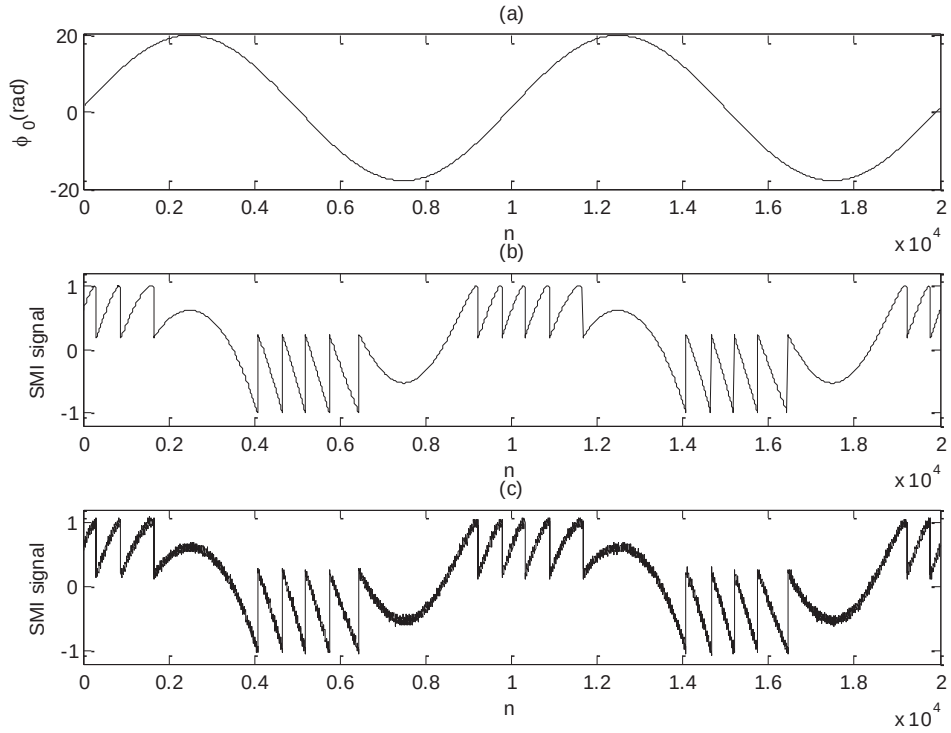


Figure 3-12: Simulated target movement and the corresponding SMI signal: (a) simple harmonic target movement; (b) clean SMI signal; (c) SMI signal contaminated with slow fluctuations and white noise.

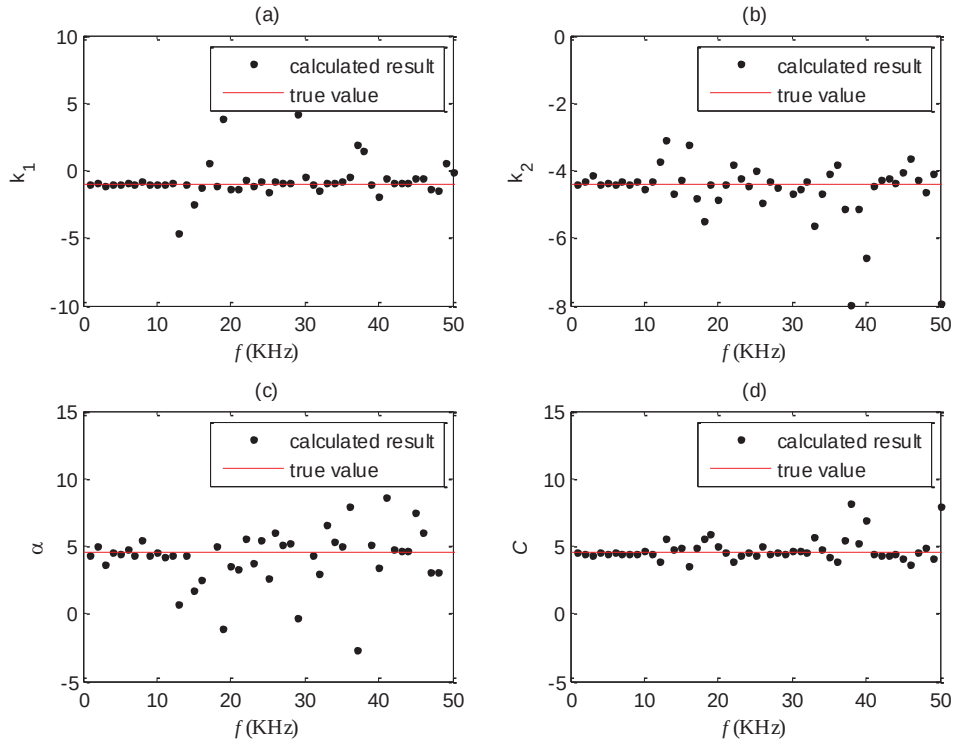


Figure 3-13: Estimation results of $k_1$, $k_2$, alpha factor and feedback parameter.

As expected, instead of being identical, the calculation results of all the parameters deviate from their true values more or less. As shown in Figure 2-13, since the value of $k_1$ is very close to zero and alpha is calculated as $\alpha = k_2/k_1$, the accuracy of alpha is highly dependent on $k_1$. Moreover, the results of alpha (in Figure 3-13(c)) are much disperse compared to $k_1$ and $k_2$, which suggest the error lies in $k_1$ and $k_2$ is actually amplified through the calculation. Therefore, instead of calculating alpha at each frequency component individually, we can determine an optimal value for $k_1$ based on the whole set of calculation results, as well as for $k_2$, then work out the final result of alpha.

When it comes to result selection, Myriad estimator can be a good candidate, especially in this case. As indicated by the result distribution pattern shown in Figure 3-13, the estimation results are distributed around the true value and also containing few outliers as well. Such pattern is very close to the impulse environment, that Myriad estimator can be highly effective.

After performing Myriad estimation, the final results of $\alpha$ and $C$ from the above simulation and their errors are listed below.

Table 3-1: Optimized estimation results of the simulated SMI signal.

| *Parameter* | *True value* | Without result optimization | | Results optimized with Myriad | |
|---|---|---|---|---|---|
| | | *Value* | *Error* | *Value* | *Error* |
| $\alpha$ | 4.5 | 2.51 | 44.2% | 4.44 | 1.3% |
| $C$ | 4.5 | 4.78 | 7.2% | 4.49 | 0.2% |

As demonstrated by Table 3-1 that the accuracy of estimation has been greatly improved, which proves the effectiveness of Myriad on removing the outliers in calculated results.

To test the performance of our proposed result optimization method in practice, a further test was conducted on experimental SMI signals. The experimental setup is based on the typical structure of an SMI system as given in Figure 1-1. The SL used in system is HL8325G with a wavelength of 830nm provided by Hitachi. During the experiment, the SL is biased

with a DC current of 70 mA and stabilized at 25±0.1°C. The moving target is a PZT placed 20 cm away from the SL front facet, which is driven by a signal generator and vibrates harmonically at 210 Hz frequency. The SMI signal consists of approximately 20 fundamental periods was collected under moderate region, for demonstration only, two periods of signal is plotted in Figure 3-14. Then the whole signal was segmented into 20 pieces and fed into the frequency-domain based alpha estimation algorithm separately. For each segment, a set of $k_1$ and a set of $k_2$ were obtained just like in Figure 3-13(a) and (b). In order to verify the effectiveness of the proposed result optimization approach, the calculation of alpha was conducted in two groups: in one group, alpha and $C$ were calculated directly from $k_1$ and $k_2$ results; in another group, the raw data of $k_1$ and $k_2$ were processed with Myriad estimator at first, then alpha and $C$ are calculated from the optimal results of $k_1$ and $k_2$. Thus 20 final results of alpha were obtained in each group. Finally, by using the mean squared error (MSE) to evaluate the accuracy of the estimation done by each group, the comparison information is reported in Table 3-2.

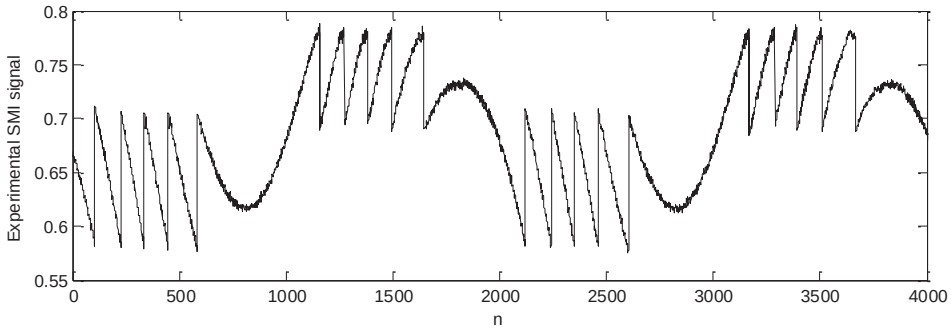


Figure 3-14: A piece of experimental SMI signal acquired under moderate feedback level.

Table 3-2: Estimation results of experimental SMI signals.

| *Parameter* | Without result optimization | | Results optimized with Myriad | |
|---|---|---|---|---|
| | *Average value* | *MSE* | *Average value* | *MSE* |
| $\alpha$ | 4.239 | 1.006 | 4.432 | 0.134 |
| $C$ | 4.394 | 0.038 | 4.434 | 0.004 |

It is noticeable that the average results of estimations are different between the two groups. But considering the results optimized with Myriad are characterized by much less MSE, it is expected that the results obtained by the proposed method are more reliable and closer to the true value than that without the result optimization process.

## 3.3 Summary

In this chapter, the calculation process of the frequency-domain based alpha measurement method is investigated in detail. Firstly, the four stages of the frequency-domain based $\alpha$ measurement method are reviewed. Then, for each stage, a detail analysis on the introduced error is provided, which followed by the optimization method proposed for preventing error propagation during the calculation. Finally, the effectiveness of proposed optimization method is verified through tests on both simulated and experimental signals.

# Chapter 4. Real-time alpha measurement on FPGA

In all the SMI based alpha measurement approaches introduced in Chapter 1, the signal processing and alpha calculation are implemented by a computer with prepared experimental SMI signal. However, this off-line computer-based processing is hard to meet the requirements of practical applications on processing speed and system compactness.

In recent years, FPGAs (Field Programmable Gate Array) are widely used in the fields of communications, consumer electronics, automotive electronics, industrial control, detection and measurements. A basic FPGA architecture consists of an array of logic blocks (or called configurable logic block), I/O pads and routing channels, generally, all the routing channels have the same width [78]. FPGA is the further development product of programmable devices such as PLA (Programmable Logic Arrays), GAL (Generic Array Logic), CPLD (Complex Programmable Logic Device). FPGA is considered as a kind of semi-custom circuits in the field of ASIC (application specific integrated circuit), thus it solves the defects in custom circuits and also overcomes the shortcomings in programmable devices duo to limited number of gates. Compared to traditional DSP (digital signal processor), FPGA supports parallel operation which provides better flexibility to suit different speed and cost requirements. Moreover, compared with the ASIC chip, FPGA is able to be reconfigured at run-time without sacrificing speed [79].

In order to make FPGA more widely available in the field of digital signal processing, FPGA suppliers like Xilinx and Altera, they all have launched simplified developing tools for their products, such as Xilinx's System Generator for DSP (or short for System Generator) and Altera's Quartus Ⅱ, thus designed algorithms can be efficiently mapped into reliable and synthesisable hardware systems with the help of developing tools.

Based on the above characteristics, combining FPGA with SMI sensing system is considered as a good solution for the real-time alpha measurements since it possesses the advantages of small size, high efficiency, abundant I/O ports and related modules, easy to configure and high-flexibility.

In this chapter, the general FPGA development process is introduced in Section 4.1.1. The structure of SMI-FPGA system and the overall design scheme of alpha measurement algorithm based on FPGA are briefly described in Section 4.1.2. In Section 4.2, the details of each block in the design is presented which followed by individual performance test. Finally, the overall testing results are reported in Section 4.3.

## 4.1 Introduction

### 4.1.1 Introduction to FPGA development

Generally, the process of FPGA design includes algorithm and module design, synthesis, implementation and download to FPGA devices. The process of FPGA design flow chart is shown in Figure 4-1 [80]. Take the Xilinx FPGA design development kit for example, the design steps are briefly described in the following paragraphs.

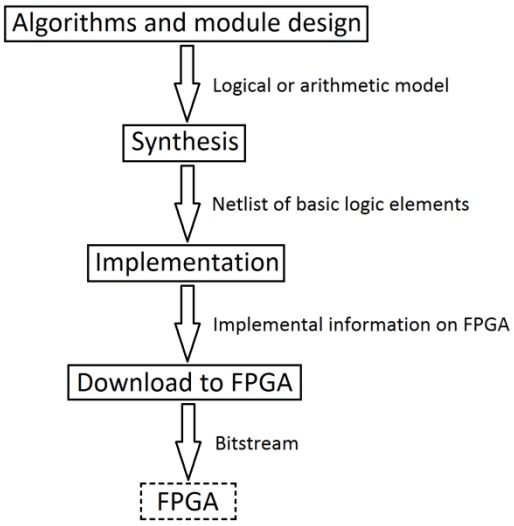


Figure 4-1: FPGA design flow.

- Algorithm and module design

System Generator is a system modelling software tool which developed by FPGA manufacturer Xilinx. System Generator provides system modelling and automatic HDL (Hardware Description Language) code generation from embedded simulation software Simulink which is based on MATLAB [80]. System Generator capable to generate the most widely-used HDL code types, Verilog HDL and VHDL (Very-high-speed Hardware Description Language). System Generator provides a suitable DSP hardware modelling environment, accelerate and simplify the FPGA design, designers only need to connect and configure the pre-set Xilinx modules built in Simulink. Related tools: Matlab, Simulink, System Generator, Xilinx blockset.

- Synthesis

After finish modelling with the Xilinx modules, by configuring the synthesis tool and output code type, the HDL contained in the modules is compiled into a netlist which comprises basic logic gates and FPGA resources. Synthesis report contains useful information like maximum frequency, they can indicate hidden problems [80]. Related tool: System Generator.

- Implementation

Implementation in Xilinx design flow has three stages: translate, map and place/route [80]. During the translate phase, the netlist generated in synthesis is translated into another netlist based on SIMPRIM library which is more close to detailed components. During the map phase, the netlist generated in translate phase is mapped into a specific device resources, like LUTs (Look Up Table) and flip-flops, moreover, precise switching delays is contained in this phase. Place and route phase is the most important, it gives the list of different device resources and how they are interconnected inside an FPGA [80]. Related tool: Xilinx ISE Project Navigator.

- Download to FPGA board

The final bitstream of configuration is downloaded into FPGA device. Related tool: Xilinx ISE Project Navigator, iMPACT.

### 4.1.2 Design overview

As the frequency-domain based alpha measurement method has been introduced in last chapter, to implement this method, the overall measuring system setup scheme is shown in Figure 4-2. The system shares the same basic structure with the one shown in Figure 2-1. The optical path from the front facet of the SL to the target surface forms the external cavity of the SL. When the target moves, the light phase at external cavity will vary accordingly, and thus results a modulation of the emitted SL power. The modulated SL power (SMI signal) is detected by a PD through a beam splitter. Finally, the SMI signal is picked out and amplified by the signal acquisition device, then fed into FPGA for real-time processing and calculations.

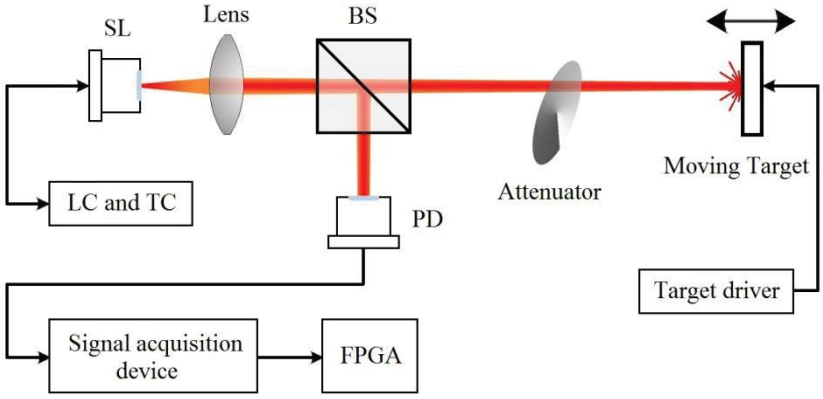


Figure 4-2: Real-time processing system schematic.

As the frequency-domain based alpha measurement has been introduced in Chapter 1, according to the measuring principle and the sensing system setup, the signal processing flow chart is plotted in Figure 4-3.

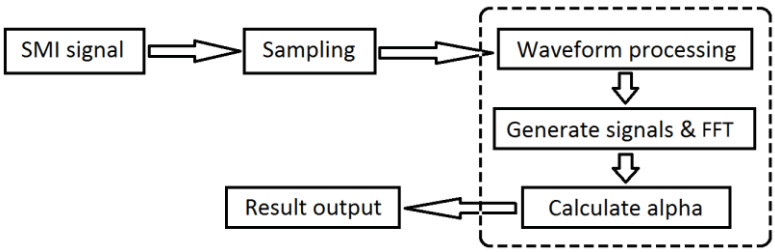


Figure 4-3: Signal processing flowchart.

The overall processes consist of three main steps:

1. Signal acquisition: The SMI signal is received by PD and amplified by trans-impedance amplifier, and then the signal is sampled by an AD converter;

2. Signal processing: This is the main process consists of three procedures that calculate alpha from the sampled initial measured SMI signal;

1) Waveform pre-processing: The raw SMI signal should be filtered and normalized first;

2) Generate related phase signals and perform FFT: The purpose of this procedure is to generate $\phi_1(n)$ and $\phi_2(n)$ from $\phi_F(n)$, which is obtained by performing inverse cosine transform and phase unwrapping on SMI signal $g(n)$. Then, applying FFT on $\phi_1(n)$, $\phi_2(n)$ and $\phi_F(n)$ to calculate their spectrum;

3) Calculate alpha: Calculate alpha by solving the spectrum-based equations;

3. Result output: The results of alpha estimation are stored and analysed, and then output an ultimate value.

According to the signal processing flow inside the dashed box in Figure 4-3, the Simulink model is designed as shown in Figure 4-4 using Xilinx blocksets.

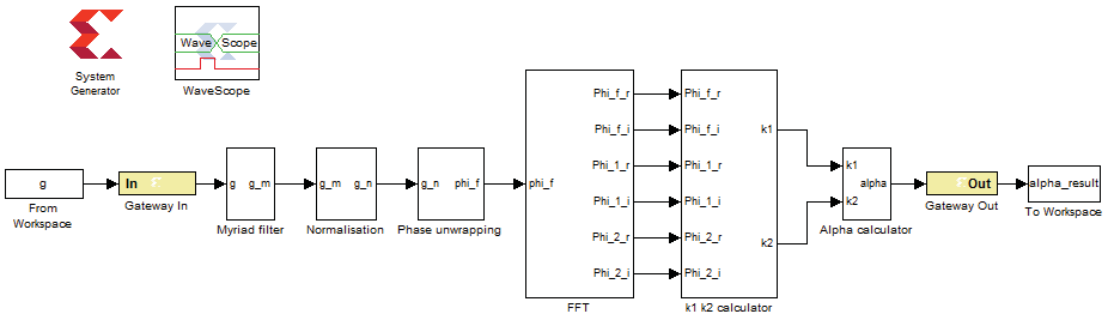


Figure 4-4: Block diagram of overall signal processing design.

In order to make the design scheme more compact, related block components are packed into subsystems according to the function they belong to.

The general processing mode is: the amplified and sampled SMI signal is sent to the signal processing unit continuously, so the output value of alpha will be updated throughout the calculation. Next, each block in Figure 4-4 will be briefly described regarding their functions and how do they work.

There are three non-stop modules: “Myriad filter”, “Normalisation” and “Phase unwrapping”. They output processing results in real-time. The “Myriad filter” module is designed based on the adaptive Myriad filter proposed in Chapter 2, which is effective to both oscillations and white noise. The “Normalisation” module keeps tracking on the value range of the filtered signal and then adjusts the amplifying rate accordingly. The “Phase unwrapping” module is integrated with the phase unwrapping algorithm specifically designed for real-time processing, which is able to synthesis the phase signal instantly from the input SMI signal (details are presented in Section 4.2.4). The “FFT” module consists of several FFT calculation units, which generate the spectrum of $\phi_1(n)$, $\phi_2(n)$ and $\phi_F(n)$ from the unwrapped phase signal. The “k1_k2_calculator” module implements the calculation of Equation 1.26, and outputs the result sequences of $k_1$ and $k_2$ which lead to the final result of alpha. The “Alpha calculator” module records and analyses the results of $k_1$ and $k_2$, then computes the final result of alpha.

In the following sections, the above modules are introduced in detail. Meanwhile, a series of simulation tests are conducted to verify the validity of each module.

## 4.2 Module design for real-time alpha measurement

### 4.2.1 Signal input

The FPGA development board Xilinx Spartan-3E (XC3S500E-4FG320C), is integrated with abundant I/O ports and associate components, including built-in AD convertors (LTC1407A-1 dual ADC) and amplifiers (LTC 6912-1 dual AMP). The two-channel analog capture circuit of ADC on the FPGA board is plotted in Figure 4-5 [81]. The programmable amplifier is employed to scale the incoming voltage on VINA or VINB so that it maximises the conversion range of the DAC. According to data sheet [81], the gain of each amplifier is programmable from -1 to -100, which is sent as an 8-bit command word, consisting of two 4-bit fields. The maximum sampling rate of the ADC is approximately 1.5 MHz and the sampling depth is 14-bit per

channel. Firstly, the gain setting of amplifier is configured by FPGA through SPI (Serial Peripheral Interface) bus. Then the scaled signal is sent into ADC, where the analog signal is converted into a 14-bit discrete digital representation. Finally, the sampled signal is sent into FPGA chip via SPI bus. Both the pre-amplifier and the ADC are serially programmed or controlled by the FPGA chip, and the data communication between them is based on SPI bus. Table 4-1 lists the important interface signals associate with the analog capture circuit.

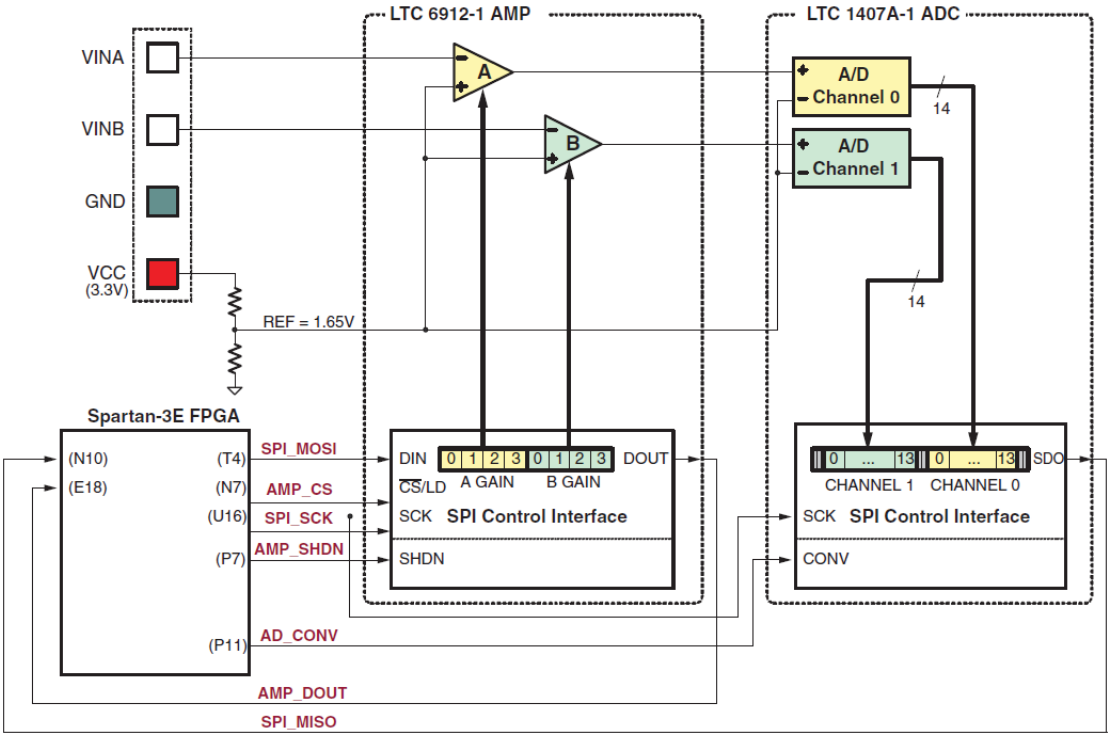


Figure 4-5: Detailed view of the analog capture circuit on FPGA.

Table 4-1: Important interface signals associate with the analog capture circuit.

| *Signal* | *Direction* | *Description* |
|---|---|---|
| SPI_MOSI | FPGA→AMP | Serial data: master output, slave Input. Presents 8-bit programmable gain settings. |
| AMP_CS | FPGA→AMP | Active-Low chip-select. The amplifier gain is set when signal returns High. |
| SPI_SCK | FPGA→AMP<br>FPGA→ADC | Clock for SPI bus communication. |
| AMP_SHDN | FPGA→AMP | Active-High shutdown/reset amplifier. |
| AMP_DOUT | FPGA←AMP | Serial data. Echoes previous amplifier gain settings. Refresh gain data when SPI_SCK returns Low. |

| | | |
|---|---|---|
| AD_CONV | FPGA→ADC | When the AD_CONV signal goes High, the ADC simultaneously samples both analog channels. |
| SPI_MISO | FPGA←ADC | Serial data: master input, serial output. Presents the digital representation of the sample analog values as two 14-bit two's complement binary values. Converted data is presented with a latency of one sample. |
| SPI_SS_B | FPGA→SPI | Disable the device to avoid bus contention by setting to logic value 1. |
| DAC_CS | FPGA→DAC | The same use as SPI_SS_B. |
| SF_CE0 | FPGA→ StrataFlash | The same use as SPI_SS_B. |
| FPGA_INIT_B | FPGA→ Platform flash | The same use as SPI_SS_B. |

By importing the HDL code into a Black Box in Xilinx Blockset, the AD controlling program can be added to our design in System Generator as a normal Xilinx module. To test the effectiveness of AD module, another module LCD display is employed (details are given in Section 4.2.7), so the digital value converted from the captured analog voltage can be directly displayed on the build-in LCD screen. The test result shows the AD module works well, as shown in Figure 4-6.


Figure 4-6: ADC module test: LCD displays the actual 14-bit value from ADC (represented in hexadecimal).

### 4.2.2 Filtering

As illustrated in Chapter 2, the main noises/distortions in SMI signals are white noise, transient oscillations and slow fluctuation. Among them, slow fluctuation can be eliminated by adjusting the acquisition circuit (discussed Section 2.1.4), while the white noise and transient oscillations are hard to avoid in practice. Therefore, the adaptive Myriad filter is designed (in Section 2.2.2) specifically for those two types of noise, and its effectiveness is verified by testing on experimental signals.

Firstly, let us review the general design idea of adaptive Myriad filter. The linear parameter $K$ determines the output characteristics of Myriad filter: to reduce white-like noise, Myriad filter is expected to exhibit its linear property, which requires a large $K$; while for removing transient overshooting, Myriad needs to be highly selective, which requires a very small $K$. Therefore, in order to simultaneously suppress two noises, suitable values should be assigned to $K$ depending on the feature of noise, e.g. in Section 2.3.4, the dispersion of signal samples is proved to be a good reference for $K$ value.

Accordingly, the design scheme of the adaptive Myriad filter block is shown in Figure 4-7, where $g_f(n)$ denotes the filtered signal sequence.

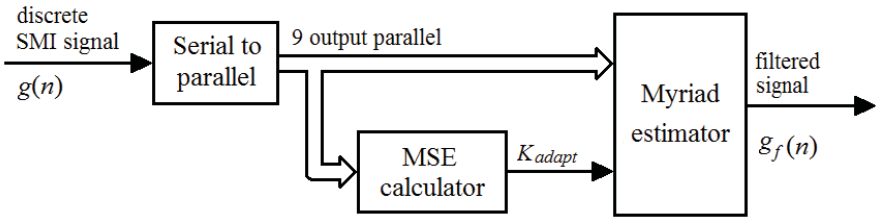


Figure 4-7: 9-point adaptive Myriad filter schematic.

Limited by the sampling rate of ADC on FPGA board, the duration of a transient response is less than 6 points in most of the SMI signals, the window width of Myriad filter $N$ can be set to 9 sample points. Firstly, sequential input SMI signal data are collected and converted into 9 paralleled outputs at block serial to parallel. Then the 9 outputs are sent to the MSE calculator block where the dispersion of the input samples and the adaptive value of $K$ is

calculated by following Equation 2.11 and 2.12. Finally, the paralleled signal and the $K$ value are sent into the Myriad estimator block where the output value is calculated by Myriad algorithm (Equation 2.8). Considering the complexity MSE calculation and Myriad algorithm, the "MCode" block provided by Simulink in Xilinx blockset category is employed to simplify the design which can be easily configured by importing Matlab functions.

Figure 4-8 shows the FPGA design of adaptive Myriad filter on System Generator. By using "From Workspace" block and "To Workspace" block, we can import test signals (simulated or experimental) from Matlab and export FPGA processing results to Matlab. To test the performance of design, a piece of experimental SMI signal was fed into the filter. Figure 4-9 presents the real-time processing results captured at the output of MSE calculator and Myriad estimator. It can be seen from Figure 4-9(b) that appropriate values were calculated and assigned to $K$ based on input signal. According to the filtering result in Figure 4-9(c), the impulsive noise-like transient has been eliminated and the white-like noise is well suppressed, which indicate the filter has satisfied the design requirements.

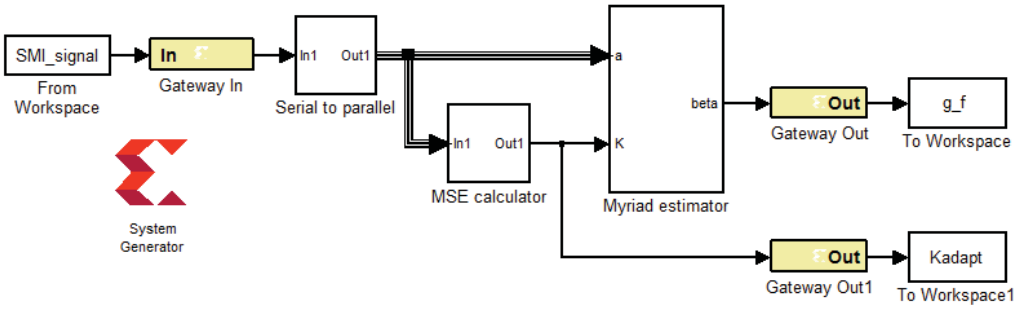


Figure 4-8: FPGA design of adaptive Myriad filter unit.

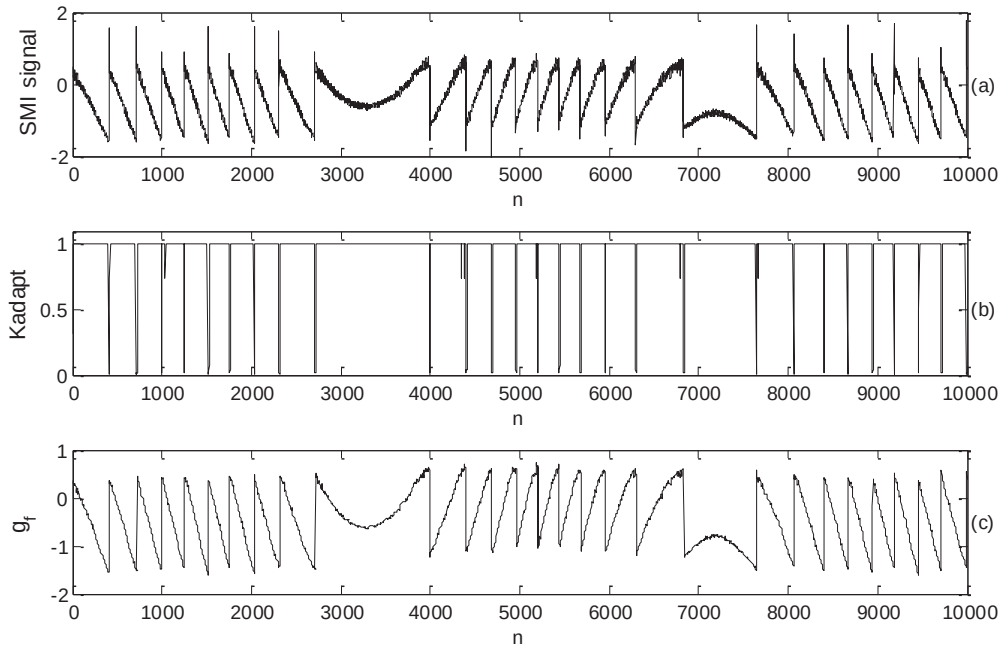


Figure 4-9: (a) Input experimental SMI signal with oscillations and white noise; (b) real-time calculation result of $K_{adapt}$; (c) real-time filtering result $g_f$.

### 4.2.3 Normalization

Normalisation is a crucial step in the signal pre-processing before applying further measurement algorithms. For a standard SMI signal $g(t)$, the values of all the data samples should fall in the range of [-1, 1] as indicated by Equation 1.11, while the signals acquired from the experimental setup in practice are unlikely to fit in this range perfectly. Furthermore, according to the frequency-domain based alpha estimation algorithm [25], the phase signal is extracted from SMI signal $g(t)$ by performing inverse cosine function and phase unwrapping, that is why a normalization process is required in signal pre-processing stage before further calculations can be done.

After filtering process, the normalisation is no longer affected by the transient overshooting and most of the white-like noise. So, it is simple to remove the direct current component through the following equation:

$$g_{nor}(n) = 2 \cdot \frac{g_f(n) - g_{fmin}}{g_{fmax} - g_{fmin}} - 1 \tag{4.1}$$

where $g_{nor}(n)$ is the normalised signal; $g_{fmax}$ and $g_{fmin}$ are the maximum value and the minimum value in $g_f(n)$ respectively. Obviously, the key point of the design is acquiring $g_{fmax}$ and $g_{fmin}$ in real-time.

Traditionally, maximum and minimum values can be found using a register. The first come-in value of the signal $g_f(n)$ is stored as an extreme value, and the next value compares with the stored one. If the next value is larger than the maximum value or smaller than the minimum value, the extreme value will be replaced by the new value. However, in practice, influenced by the slow fluctuations and residual noises that unable to be filtered out, the extreme values obtained by this method are very unreliable. An example is given in Figure 4-10 to illustrate this issue.

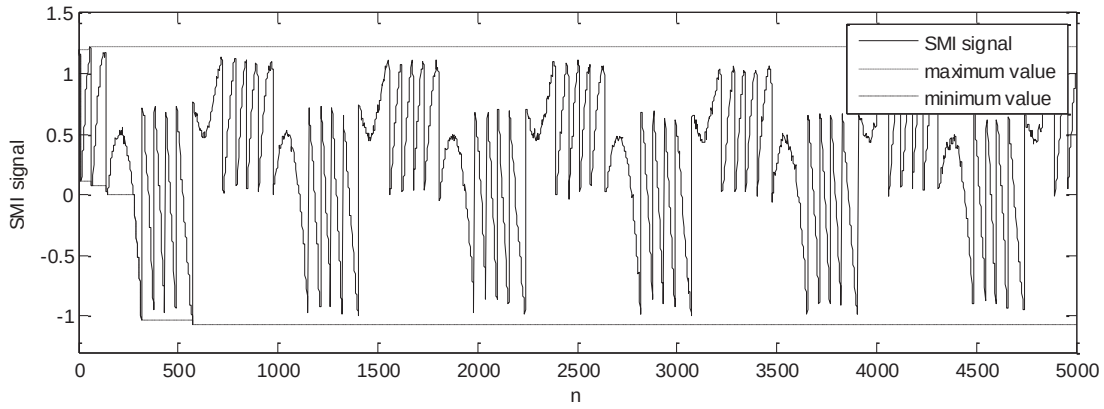


Figure 4-10: Real-time extreme value detection result.

As shown in the figure, due to the fluctuations at the beginning, the detected extreme values are not suitable for the rest of the waveform, which must lead to considerable error during the normalisation. The flaw of this detection method has been revealed though this case: instead of flexible updating along with the real-time signal, the range (extreme values) can only be expanded during the detection. To compensate this deficiency, a negative feedback mechanism is required.

Figure 4-11 gives the design idea of updating maximum value based on the input signal, where $m$ denotes the index of the maximum value of signal in a certain period (local

maximum); $x$ is a configurable threshold. In Figure 4-11, Case 2 describes the traditional detection method mentioned earlier: once the come-in sample value $g_f(n)$ exceeds the current maximum value, $g_{fmax}$ will be updated. Additionally, two other cases are considered in this design to address the remaining issue in the traditional method. Case 3 describe the situation when $g_{fmax}$ has not been exceeded for a long period of time, then $g_{fmax}$ should be reduced so it can stick to the signal border again. In order to avoid triggering Case 3 too frequently, a tolerance range is designed in Case 1. That is, if the local maximum value only exceed $g_{fmax}$ a little bit, then $g_{fmax}$ does not need to be updated.

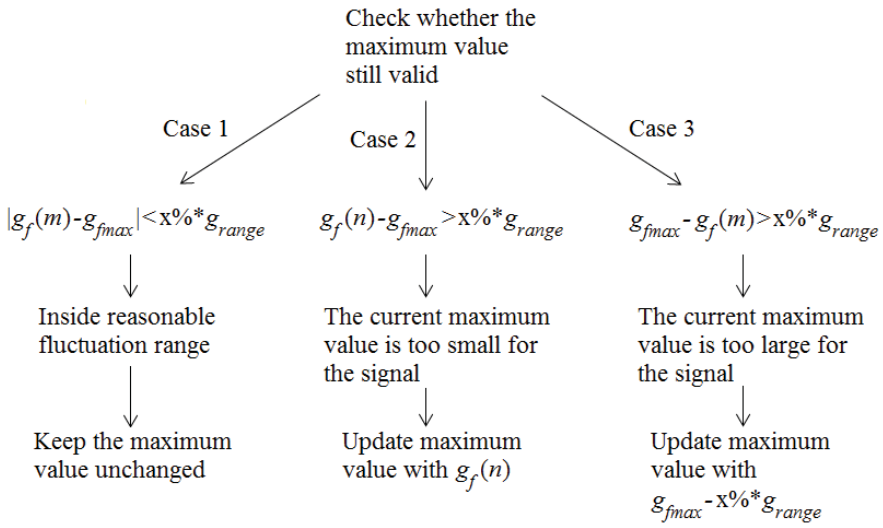


Figure 4-11: Flow chat on how to update maximum value based on the input signal.

The idea of this design is simple and straightforward, only involves IF statements and simple calculations which can be easily implemented by a single "MCode" block with Matlab function. With the real-time maximum and minimum values ( $g_{fmax}$ and $g_{fmin}$ ), then the rest of the normalization calculation only requires several basic arithmetic blocks in Xilinx Blockset category. The final design diagram is given in Figure 4-12.

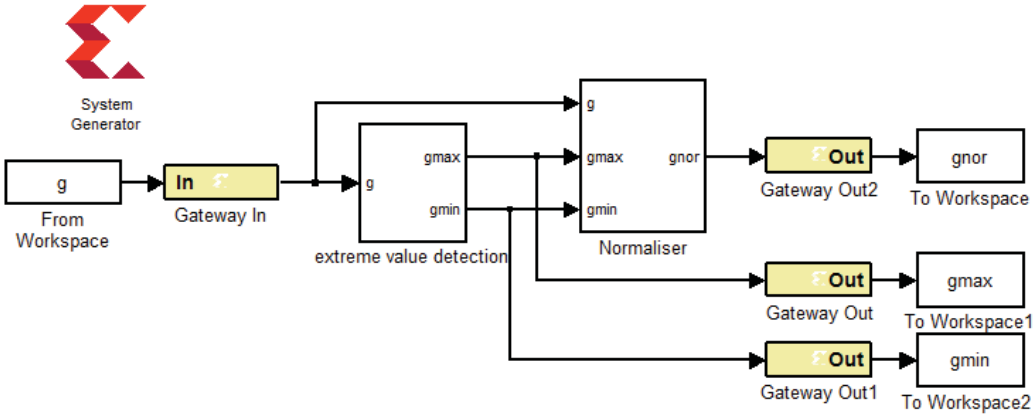


Figure 4-12: FPGA design of normalisation unit.

To test the effectiveness of the design, the SMI signal in Figure 4-10 is employed again as the input signal, and the real-time processing results are plotted in Figure 4-13.

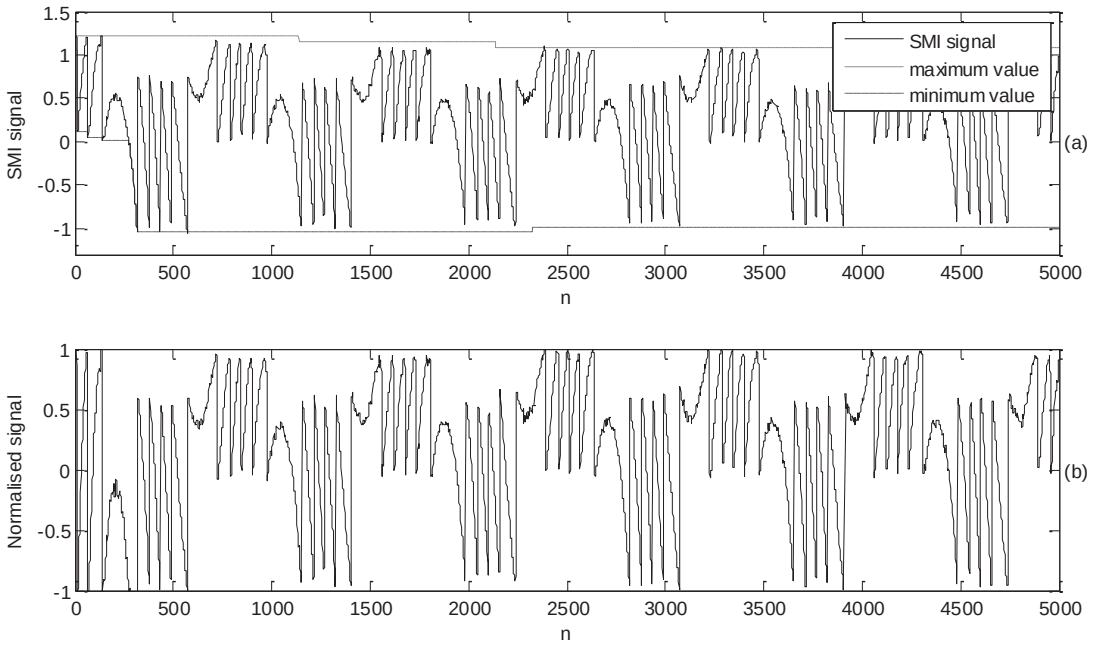


Figure 4-13: Real-time processing results of extreme value detection and normalisation.

From the real-time processing result shown in Figure 4-13, it can be seen that the detected extreme values are updated flexibly along the incoming signal, thus leads to a much better normalisation result as shown in Figure 4-13(b).

### 4.2.4 Phase unwrapping

The phase unwrapping of the signal under the weak feedback level is very simple since there is no hysteresis effect. However, the signal SNR under the weak feedback level is poor because of the additive noises exist in the system. So normally, we prefer to conduct the measurement of alpha under the moderate feedback level for better accuracy.

According to the work in [51], the calculation of phase unwrapping is divided into left inclination and right inclination, which respectively correspond to positive direction and negative direction of the target movement, as shown in Figure 4-14. Characteristic points P and V denote the peak and valley of each fringe. J points are called jumping points where SMI signal exhibits sudden change.

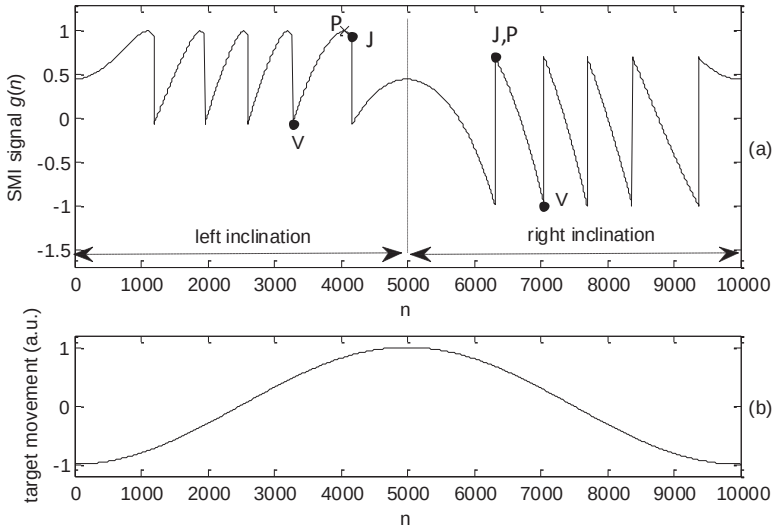


Figure 4-14: (a) Simulated SMI signal; (b) corresponding target movement of (a).

When feedback strength parameter $C$<1, i.e. under weak feedback level:

$$\phi_F(n) = (-1)^{i_{VP}} \arccos[g(n)] \tag{4.2}$$

When 1< $C$ <4.6, i.e. under weak feedback level, for the waveform in right inclination, the phase is calculated as:

$$\phi_F(n) = (-1)^{i_{VP}} \arccos[g(n)] + 2\pi(i_V + 1) \tag{4.3}$$

For the waveform in left inclination, the phase is calculated as:

$$\begin{cases} \phi_F(n) = -\arccos[g(n)] + 2\pi i_V, \text{ for VP and PV region} \\ \phi_F(n) = +\arccos[g(n)] + 2\pi i_J, \text{ for PJ region} \end{cases} \quad (4.4)$$

Where $i_{VP}$ $i_V$ and $i_J$ are updated as:

$i_{VP} = i_{VP} + 1$, when at P points or V points

$i_V = i_V - 1$, when at V points in right inclination

$i_V = i_V + 1$, when at V points in left inclination

$i_J = i_J + 1$, when at J points in left inclination

To implement above PUM on DSP devices, the come-in SMI signal needs to be segmented and stored into a ROM, so the characteristic point detection program can analyse the waveform by constantly accessing the memory, and then sends back the detection results. Finally, the phase signal is synthesised based on the stored SMI signal and the detected indexes of characteristic points. Obviously, such processing scheme is actually an intermittent off-line processing and requires data exchange with the storage all the time, which is inefficient on both processing speed and resource utilization. Therefore, to achieve real-time processing on DSP devices, the structure of PUM algorithm need to be simplified and refined.

#### 4.2.4.1 Simplified PUM

By looking into the principle of PUM, there are actually only two key points, one is the sign of $\arccos[g(n)]$ in $\phi_F(n)$, i.e. Equation 4.4, another is the cumulative multiples of $2\pi$ (i.e. $i_V$ and $i_J$). Firstly, $+\arccos[g(n)]$ is only applicable at PJ. For the rest of the waveform, $\phi_F(n)$ is calculated as $-\arccos[g(n)]$ plus the multiples of $2\pi$. Thus Equation 4.3 and 4.4 can be combined together. Secondly, the cumulative trend (add or subtract) of $2\pi$ component should be increment in left inclination and decrement in right inclination, which practically can be triggered by the falling edges and the raising edges in a SMI signal. This supersedes

the updating rule of $i_V$ which discriminates left inclination and right inclination. Thus, the PUM is simplified as:

$$\begin{cases} \phi_F(n) = +\arccos[g(n)] + 2\pi i_V, \text{ for PJ part} \\ \phi_F(n) = -\arccos[g(n)] + 2\pi i_J, \text{ for the rest} \end{cases} \quad (4.5)$$

Where $i_J$ is updated as:

$i_J = i_J - 1$, raising edge at J

$i_J = i_J + 1$, falling edge at J

For implementation, the raising edge and the falling edge at J points can be easily detected with the differential value of SMI signal; the location of PJ is determined by a falling edge-triggered peak detection, details are given in Section 4.2.4.2.

Compared to the original PUM, the benefits of above simplification are: (1) no need to discriminate between the left inclination and the right inclination; (2) no need to determine the indexes of characteristic points before phase unwrapping.

In summary, although for off-line processing, the simplification is not significant in terms of basic principles or calculation accuracy, for real-time sequential signal processing on DSP devices, e.g. FPGA, the simplification is crucial since it lifts the limitations in off-line processing scheme and improves the processing efficiency.

#### 4.2.4.2 FPGA implementation

As indicated by Equation 4.5, region PJ need to be treated specially during the phase unwrapping. In moderate feedback regime, PJ region only exists in the left inclination part [45,46,54] and the duration is too short compared to a whole fringe, thus its influence used to be ignored in rough PUMs [75,76]. For alpha estimation using the frequency-domain based method in [25] which involves Fourier transform, based on our experience, reliable results are obtained only when the signal resolution reaches approximately 1000 sample points per fundamental period. In this case, the PJ region normally only occupies less than

30 points under the moderate feedback level, which suggests P can be located within 30 points ahead of J, as shown in Figure 4-15 ($L$=0.45$m$, $\Delta L$=1.3$\lambda_0$, $f$ =100Hz, $\alpha$=3, $C$=2). That is, the knowledge of J is required in order to locate P. However, the appearance of J is not predictable in real-time, unless introducing a 30-point delay to P detection so that the two detections can proceed simultaneously.

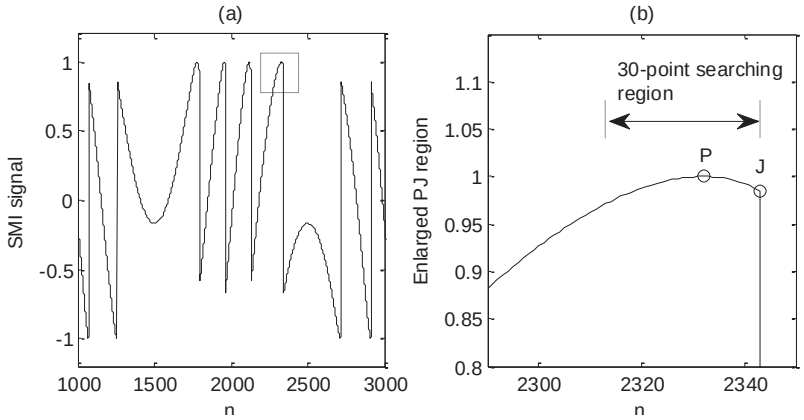


Figure 4-15: (a) A segment of SMI signal; (b) the enlarged view on the dashed area in (a).

Based on the above real-time PUM scheme, the final design of FPGA implementation is given in Figure 4-16. Firstly, to import simulated signal and collect the simulation results, From Workspace block and To Workspace block are employed (some of them are packed inside subsystems for tidiness). Block arcos calculates the inverse cosine values of input signal "g". Since the FPGA board (Spartan-3E) does not support CORDIC (coordinate rotational digital computer) based computation of arccos and arcsin, a LUT-based design is developed instead, which is faster and more efficient in execution. The "J_detect" block detects the raising edge and the falling edge (i.e. J points) based on the differential value of input signal, which is required by block "2kpi" for updating $i_J$ and also block "P_search_area" for determining the P searching region. Block "P_detect" detects the maximum value within the P searching region and reports the position of P to block "PJ_region", where the information of J and P are combined. Finally, the outputs of the former blocks are synthesized via the block "phase_systhesis" by following the PUM algorithm in Equation 4.5.

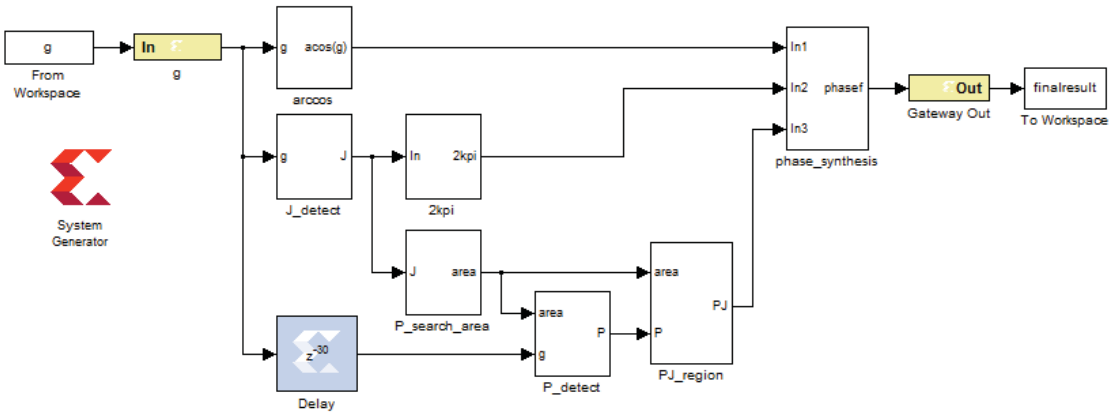


Figure 4-16: FPGA design of the real-time phase unwrapping unit.

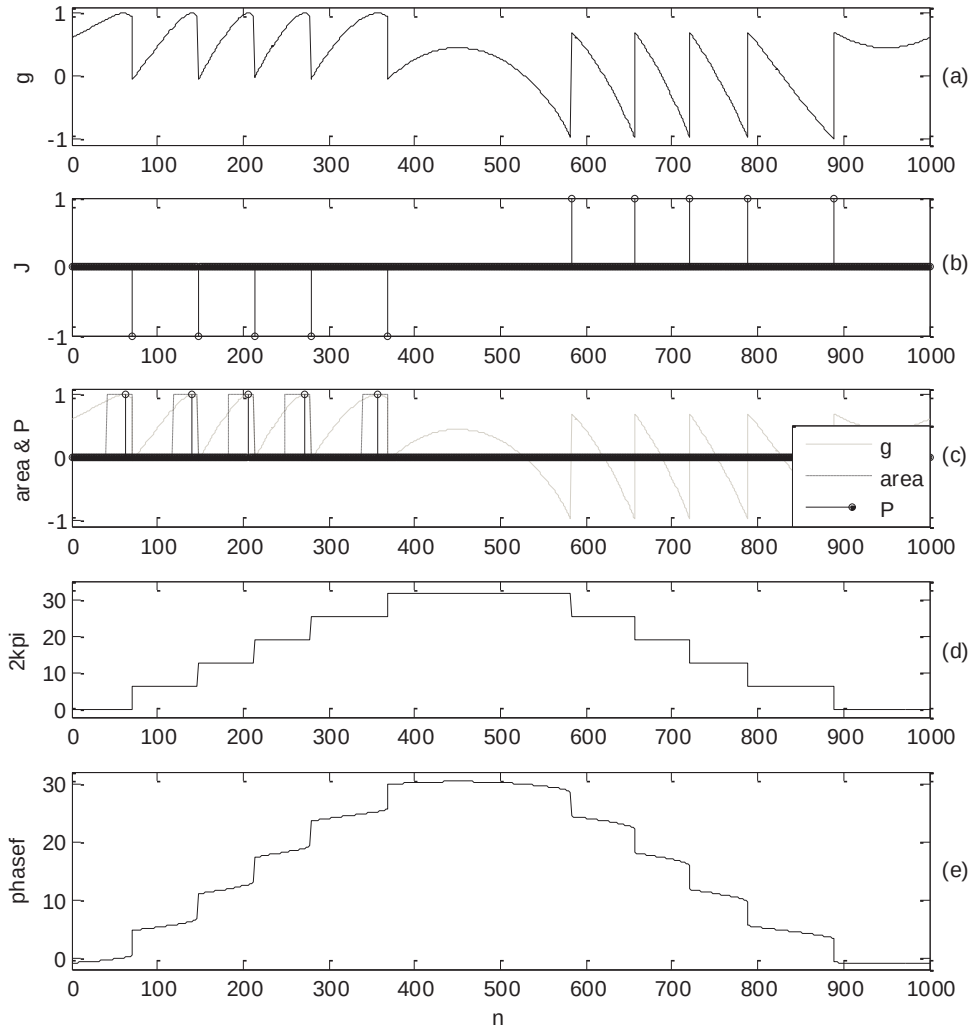


Figure 4-17: Real-time processing result of the phase unwrapping module: (a) input SMI signal; (b) detected edges; (c) 30-point searching region indication and detected P points; (d) the output of block "2kpi"; (e) the final output of synthesized phase signal.

To test the effectiveness of the design, a simulated SMI signal ($L$=0.45$m$, $\Delta L$=1.4$\lambda_0$, $f$ =100Hz, $\alpha$=2.5, $C$=3) was fed into the import port, the output of each module was monitored and plotted in Figure 4-17. According to the verification results, all the characteristic points were correctly detected thus lead to an accurate phase unwrapping result. Therefore, the phase unwrapping unit is proved to be fully functional and the design is successful.

### 4.2.5 Spectrum calculation

Spectrum calculation is the foundation of the frequency-domain based alpha estimation, which consists of two steps:

(1) Generate the temporary phase signals $\phi_1(n)$ and $\phi_2(n)$ from $\phi_F(n)$ as $\phi_1(n) = \sin[\phi_F(n)]$, $\phi_2(n) = \cos[\phi_F(n)]$;

(2) Generate the spectra of $\phi_1(n)$, $\phi_2(n)$ and $\phi_F(n)$.

The FPGA design scheme is simple and straightforward, as shown in Figure 4-18.

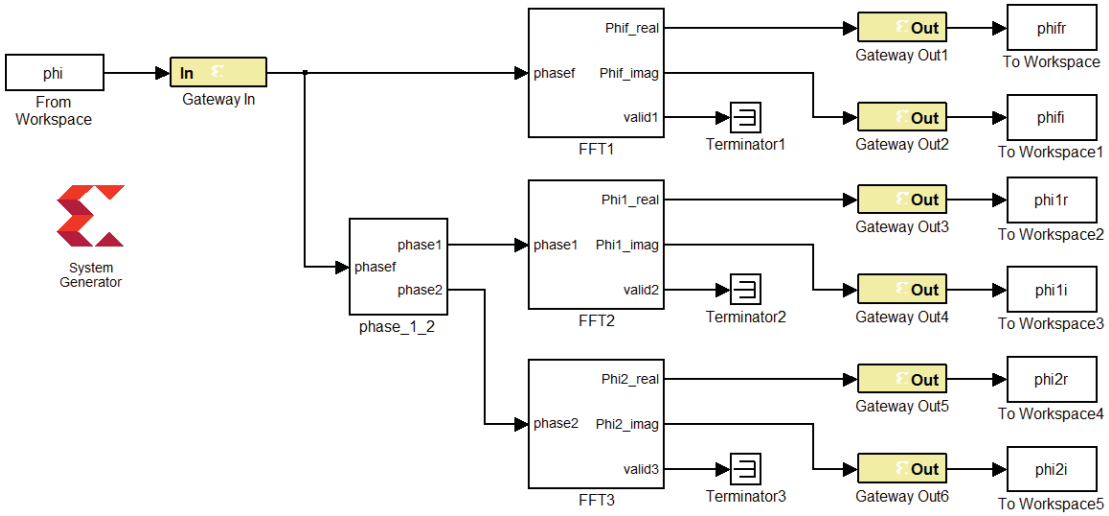


Figure 4-18: FFT module group design.

Firstly, the "phase_1_2" module computes the sine and cosine values of the input phase signal ($\phi_F$, denoted as "phasef" in Figure 4-18), which is the outcome of phase unwrapping unit. As mentioned in the last section, although there are existing CORDIC blocks in Xilinx

Blockset library which are capable of computing trigonometric functions, but they are inefficient and have strict limitations for input signal which make them hard to be coordinated. Therefore, we still use LUTs here to obtain $\phi_1(n)$ and $\phi_2(n)$ (denoted as "phase1" and "phase2" respectively in Figure 4-18).

FFT block are available from the Xilinx Blockset library, they are integrated with abundant IO ports so that they are easy to coordinate and configure. To keep the design diagram tidy, most of the IO ports and their related blocks are packed inside the subsystem, only few main communication ports are left out, they are: signal input port, real and imaginary components of FFT output data stream, output valid indicator. The output valid indicator "valid1", "valid2" and "valid3" are reserved for diagnoses and calculation complete indication, which will be used in the following alpha calculation unit.

As usual, to verify our design on FFT modules, an ideal phase signal is fed into the system from Matlab workspace; meanwhile the outputs are monitored and recorded. The simulation results are plotted in Figure 4-19.

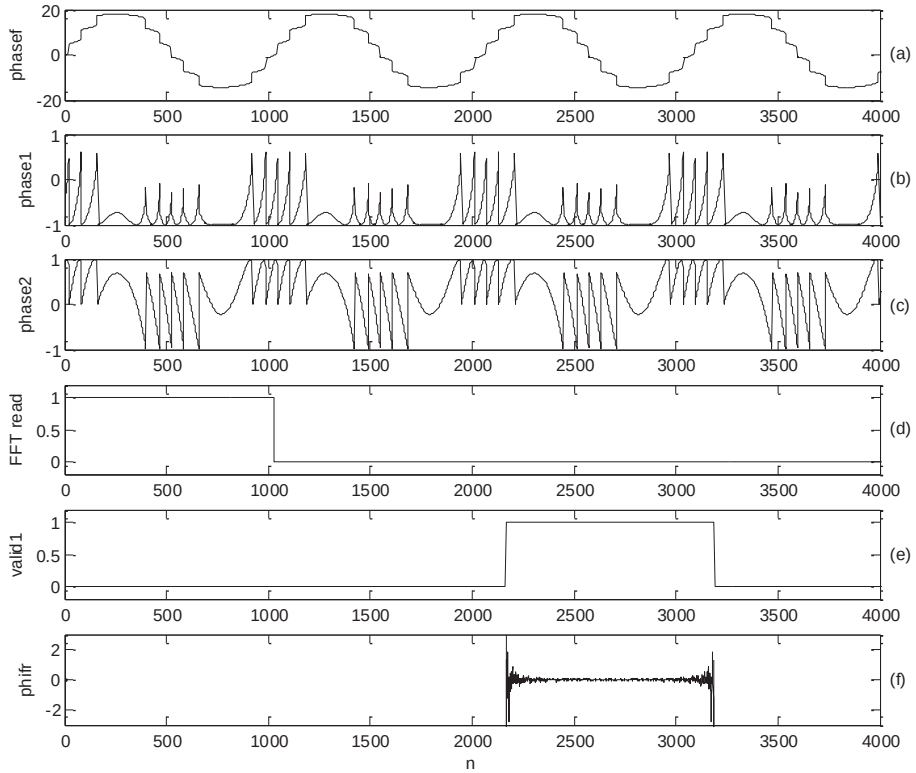


Figure 4-19: Simulation results of FFT module testing.

As shown in the Figure 4-19(a), (b) and (c), the trigonometric function computing module "phase_1_2" is non-stop, just like other previously designed modules. However, an FFT block requires a long time to process the input sequence, which can be observed from the time difference between the data reading period in (d) and the output valid period in (e). Please note that all the spectra were successfully generated, only "phifr" (the real component of "phasef"'s spectrum) is plotted in Figure 4-19 for demonstration.

Since the internal resources of an FPGA are very limited, the data precision is often compromised due to this reason. To ensure the data precision in this design is acceptable, the spectra obtained in the previous simulation are directly used to complete the estimation of alpha, and the results are plotted in Figure 4-20. As mentioned in previous chapters, under ideal circumstances, the estimation results should be identical at each frequency component. In this case, the precision of our design is very satisfactory according to the test results.

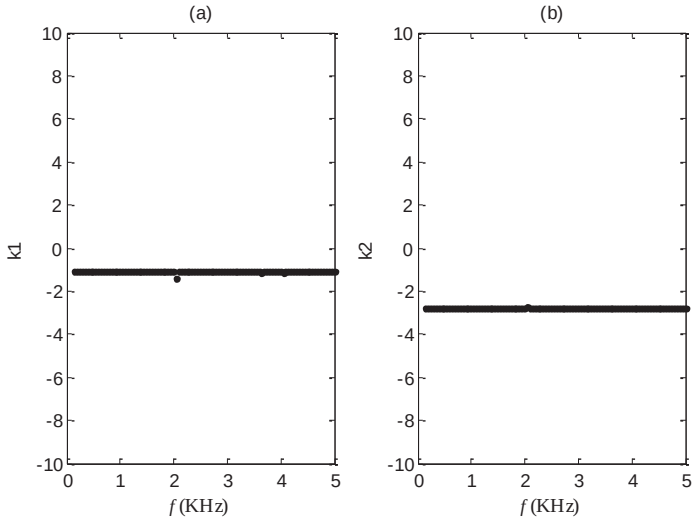


Figure 4-20: Calculation results of $k_1$ and $k_2$ which determines the final value of alpha.

### 4.2.6 Alpha calculation and optimization

The alpha estimation and result optimization module implements most of the calculations in the frequency-domain based alpha estimation algorithm.

For illustration purpose, the expressions of $k_1$, $k_2$ and their relation with $\alpha$ are relisted here

$$k_1 = \frac{\Psi_F^I \Psi_2^R - \Psi_F^R \Psi_2^I}{\Psi_1^I \Psi_2^R - \Psi_1^R \Psi_2^I}, \quad k_2 = \frac{\Psi_1^R \Psi_F^I - \Psi_1^I \Psi_F^R}{\Psi_1^I \Psi_2^R - \Psi_1^R \Psi_2^I} \tag{4.6}$$

$$\alpha = k_2 / k_1, \quad C = \sqrt{k_1^{\,2} + k_2^{\,2}} \tag{4.7}$$

where $\Psi_F = \sum_{f \subset \Omega} \Phi_F(f)$, $\Psi_1 = \sum_{f \subset \Omega} \Phi_1(f)$, $\Psi_2 = \sum_{f \subset \Omega} \Phi_2(f)$; $\Phi_F(f)$, $\Phi_1(f)$ and $\Phi_2(f)$ denotes the FFT results of phase signals $\phi_1(n)$, $\phi_2(n)$ and $\phi_F(n)$ respectively; $\Omega$ represents a frequency interval on spectrum; superscripts "R" and "I" denote the real and imaginary part of a complex number.

Through the last section, we have obtained the spectra of phase signals $\phi_1(n)$, $\phi_2(n)$ and $\phi_F(n)$, which are output sequentially in natural order. Considering the case that letting the frequency interval $\Omega$ equals to the resolution of FFT, then every frequency component on those spectra will lead a set of $k_1$ and $k_2$. In FPGA environment, this means one set of $k_1$ and $k_2$ is calculated per computing cycle from the FFT results, which has the following expression:

$$k_1(n) = \frac{\Psi_F^I(n)\Psi_2^R(n) - \Psi_F^R(n)\Psi_2^I(n)}{\Psi_1^I(n)\Psi_2^R(n) - \Psi_1^R(n)\Psi_2^I(n)}, \quad k_2(n) = \frac{\Psi_1^R(n)\Psi_F^I(n) - \Psi_1^I(n)\Psi_F^R(n)}{\Psi_1^I(n)\Psi_2^R(n) - \Psi_1^R(n)\Psi_2^I(n)} \tag{4.8}$$

Thus after processing the spectra samples within the valid frequency range (typically 15~125 times of the target vibration frequency), two sequences of $k_1$ and $k_2$ are obtained. The FPGA implementation scheme is shown in Figure 4-21. The results of $k_1$ and $k_2$ are simultaneously calculated in block "k1k2_calculator" by using Equation 4.8.

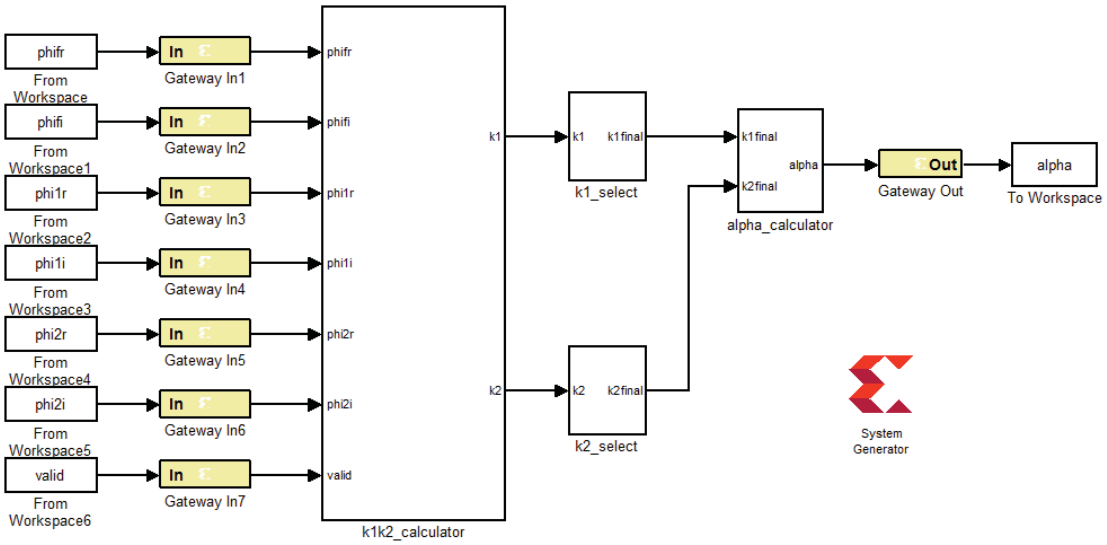


Figure 4-21: Alpha estimation and result optimization module design.

As mentioned in the previous chapters, in ideal circumstance, all the values in sequence $k_1$ (or in $k_2$) should be identical. While in non-ideal circumstances, we need to select an appropriate value from the calculation results. In Section 3.2.4 we propose to choose the most repeated value as the final output by means of Myriad estimation. Unfortunately, considering the data sequence is too large (theoretically there will be hundreds of results), the Myriad estimation will consume huge resources to complete the calculation, which is very inefficient and time-consuming. Alternatively, an easy but effective approach is proposed here based on averaging and result feedback.

Figure 4-22 is the unfolded scheme of module "k1_select" (or "k2_select", they are identical), which capable of rejecting the outliers in input result sequence and then able to calculate the average value. The raw data sequence comes in from the input port "k1". The "MCode" block "k1k2select" is a data pre-select block. After the average result is comparatively stable, it filters out the outliers in raw data sequence based on the feedback from final output value. The block "k1k2select" has two output ports, one gives the current data value, and another indicates whether the current result should be used. Once the value passed the quality check, then it will join the averaging conducted in block "average calculator". Finally,

after the average result reaches stability, block “k1k2select” will enable the final result output and allow giving feedback thus improves the accuracy further.

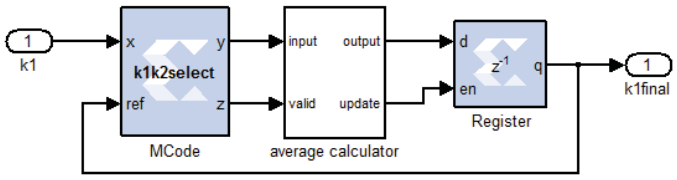


Figure 4-22: Result optimization blocks “k1_select”.

To test the performance of the result optimization block, a simulated noisy SMI (SNR=25dB) was processed through the alpha estimation algorithm, and the raw results of $k_1$ are plotted in Figure 4-23(a). Then the result sequence was sent into the result optimization block, the output port “y” in “MCode” block and the final output “k1final” were monitored and reported in Figure 4-23(b). By comparing the $k_1$ sequences before and after the pre-select block (“MCode” block), clearly the outliers in Figure 4-23(a) are rejected with the guidance of feedback reference. The final output value of $k_1$ in Figure 4-23(b) is 1.199, and the true value is 1.114. Considering the severe dispersion of the raw results, the performance of the result optimization block is satisfactory.

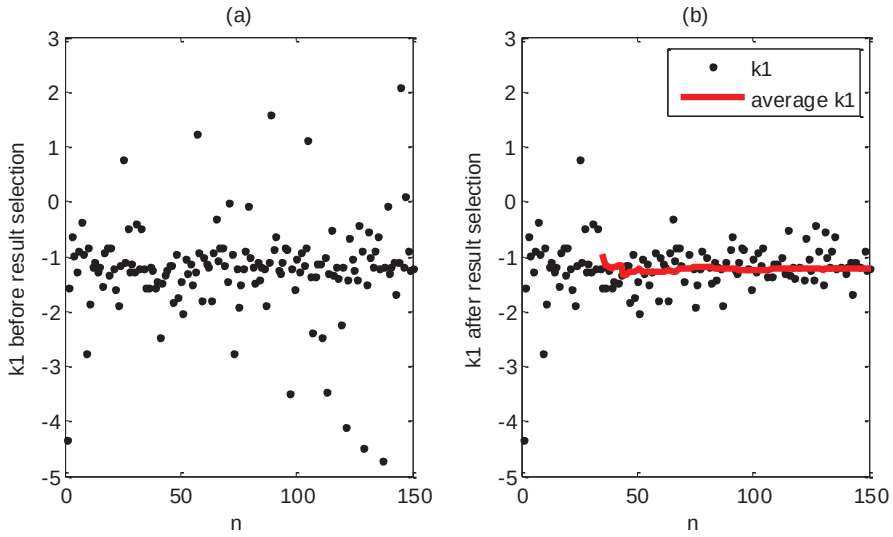


Figure 4-23: Result sequence before and after the block “k1k2select”.

Finally in the “alpha_calculator” block, $\alpha$ is calculated by “k2final”/“k1final”.

As usual, the overall error of the module will be tested through ideal signals. The calculated spectra of an ideal SMI signal were sent into the input ports of the module, and the real-time results of $k_1$, $k_2$ and $\alpha$ are collected and plotted in Figure 4-24. The final estimation result of $\alpha$ is 2.498, which is extremely close to the true value 2.5 (error < 0.1%).

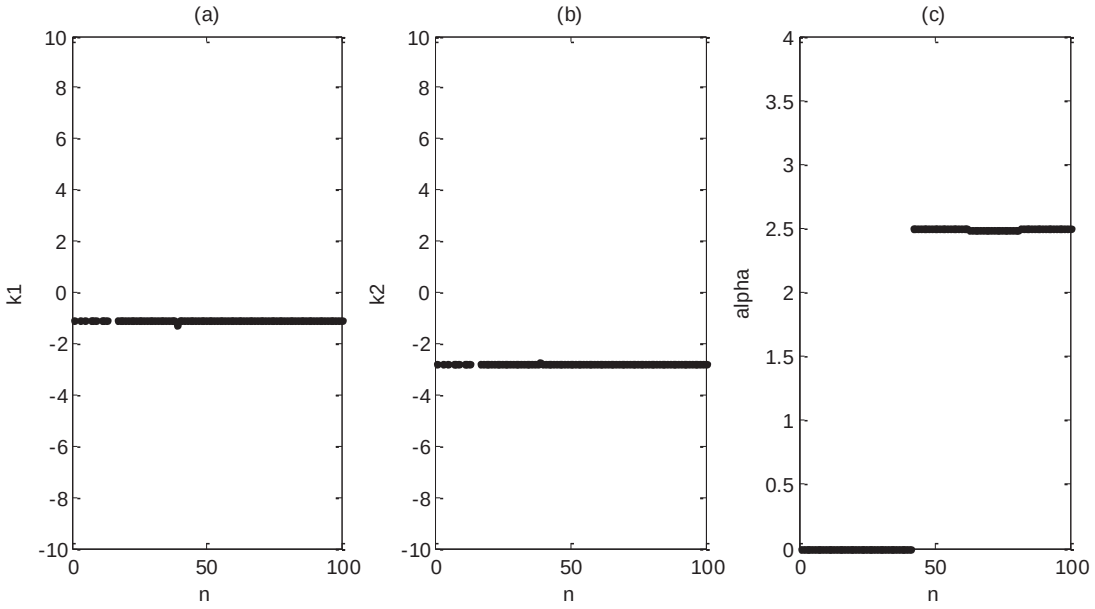


Figure 4-24: Overall error test results of the alpha estimation and result optimization module.

### 4.2.7 LCD display

The last step of this FPGA based measurement design is to display the results of $\alpha$ on the LCD (liquid crystal display) screen. The LCD on the Spartan-3e FPGA board has a Character Generator ROM (CG ROM) which contains the font mapping for each of the pre-defined character that can be displayed, the mapping table is given in Figure 4-25 [81]. Taking character "$\alpha$" as an example, according to the mapping table, the corresponding upper nibble and lower nibble should be "1100" and "0000" respectively. Then those nibbles are sent to LCD's ROM by the HDL program module which is written by following the FPGA-LCD communicating protocol. Complete LCD character display command set is available in the Spartan-3E user guide Table 5-3 [81].

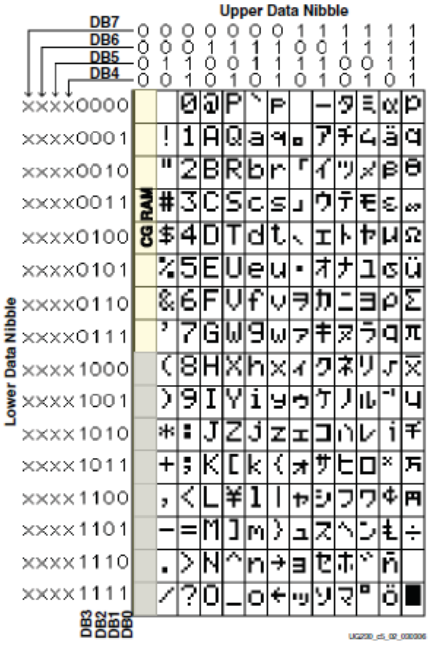


Figure 4-25: LCD character mapping table.

Take the input $\alpha$ = 3.45 for instance, since "$\alpha$=" and decimal point "." are fixed format in display, we only need to transfer the value of $\alpha$ into three digits, one for integer and the rest for fraction. All the digits are extracted by performing simple multiplications and divisions. To extract the integer bit "3", we take the integer remainder of dividing 3.45 by 10, thus the upper data nibble of the integer digit is "0011" and the lower nibble is "0011". The first fraction digit "4" is extracted by multiplying 3.45 by 10 and then taking the integer remainder of dividing 34.5 by 10, which makes the upper nibble "0010" and the lower nibble "0100" for the second digit. Similarly, the last digit "5" is the integer remainder of dividing 345 by 10, which is represented by the upper nibble "0010" and the lower nibble "0101".

By packing the HDL program into a Black Box in Xilinx Blockset, the LCD display program can be added to our design as a normal module. To test the display module, the Black Box coded with LCD driver was connected to the final output port of the alpha calculation module from the previous section. The test result is shown in Figure 4-26.


Figure 4-26: Test result of LCD driver module.

## 4.3 Overall test

To test the overall accuracy of the whole FPGA design, a piece of simulated ideal SMI signal ($\alpha$=5, $C$=2) was fed into the input port. The real-time input signal and the output results of $\alpha$ are recorded and plotted in Figure 4-27, where the final estimation result of $\alpha$ is 5.05, thereby the overall error of the design is approximately 1% (or $\pm$0.05).

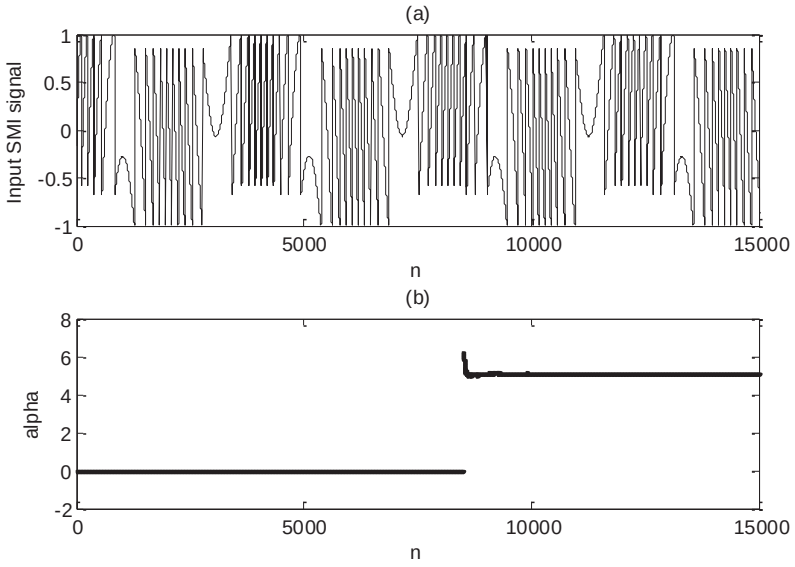


Figure 4-27: Overall error test results of the whole design.

Then the whole FPGA design is transferred to a bit-stream file by Xilinx ISE and downloaded into the FPGA board. The FPGA based SMI system is completed and the values of $\alpha$ can be read from the LCD, as shown in Figure 4-28. Each device has been introduced in Section 2.1.1.

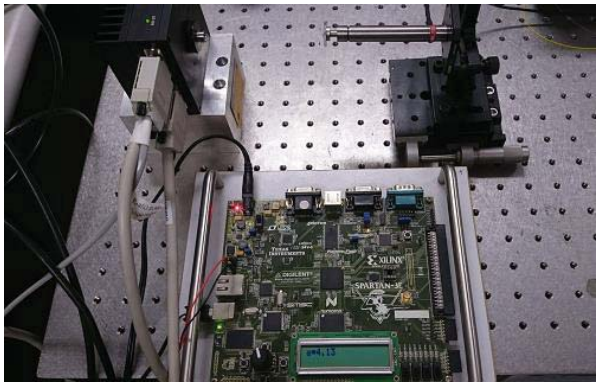

Figure 4-28: Measurement system based on FPGA.

When the system is working, the SMI signal detected by PD passes through the trans-impedance amplifier, the acquired signal is shown in Figure 4-29. Firstly, the signal was processed with Matlab, the final estimation result of $\alpha$ is 4.16. Then, the experimental signal was sent into FPGA, the displayed result on LCD is $\alpha$=4.13 (as shown in Figure 4-30), which coincide with the results obtained by off-line processing on Matlab. Therefore, the performance of this FPGA design is reliable, and this design meets the requirements. Note the slight difference on the calculated results of alpha is due to the different data precision formats adopted by Matlab and FPGA. In Matlab, data precision format is double (64-bit) in all the calculations. However in FPGA, lower data precision formats are used for calculation due to the limited resources (e.g. 16-bit in the phase unwrapping block and 32-bit in the FFT block). Then, the error caused by lower data precision in early stages is inherited and even amplified throughout the calculations.

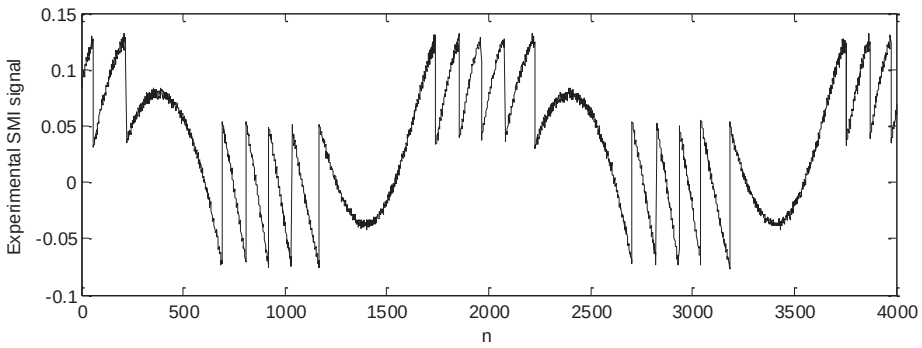


Figure 4-29: Obtained experimental SMI signal in test.


Figure 4-30: Measurement result of $\alpha$ on LCD.

## 4.4 Summary

In this chapter, an FPGA based real-time $\alpha$ measurement system using the frequency-domain based method is presented. The signal pre-processing design includes a 9-point adaptive Myriad filter and an adaptive normalization unit. The alpha estimation design includes three modules: phase unwrapping module, spectrum calculation module, and alpha estimation and result optimization module. For signal input and result output, driving modules for analog capture circuit and LCD are created. Each designed module was verified separately with simulated and experimental signals. The overall test result on FPGA shows good agreement with the calculation done by Matlab.

# Chapter 5. Conclusion

Self-mixing interferometry (SMI) has been an active and highly promising research area for non-contact sensing and measurement. Measuring the linewidth enhancement factor ($\alpha$) by using SMI technique is a significant application. However, the performance of measurement is always suffered from the noises and distortions exist in the system. In this thesis, how to acquire a clean SMI signal and how to improve the performance of $\alpha$ measurement are investigated. Furthermore, in order to make the measuring system more compact and can achieve real-time measurement, an FPGA based system is designed and implemented.

In this chapter, the research contributions are summarised in Section 5.1, and based on studies in this thesis, future research works are proposed in Section 5.2.

## 5.1 Research contributions

- A new filtering method based on Myriad algorithm is proposed specially for eliminating the transient oscillation in SMI signals. The proposed method can effectively remove the oscillation while preserve the original waveform of the signal.
- By incorporating the proposed normalization method and result optimization method, an improved frequency-domain based alpha measurement method is developed. This method can effectively reduce the error propagation among the calculation process thus improve the measurement accuracy.
- A real-time measurement system for alpha using the frequency-domain based method is implemented on FPGA. The module design includes: signal acquisition module (analog to digital), signal pre-processing module (filtering and normalization), calculation module (phase and spectrum calculation) and result display module. Both software and hardware simulations were conducted to verify

the design. The system was also tested by using experimental SMI signals and the measurement results shows good agreement with the off-line calculated results.

## 5.2 Suggested future work

In further work on SMI signal pre-processing and alpha measurement, the following research topics would be helpful:

- Advanced signal processing can be further studied and applied on experimental SMI signals to improve SNR.
- The experimentally obtained SMI signals may contain low frequency envelope. The frequency range of the envelope has overlapped with the spectrum of an SMI signal. In this case, it is difficult to remove the envelope by using normal filtering methods. Both hardware design and digital signal processing can be further studied to remove the envelope.
- The factors influencing alpha can be further investigated by employing the system designed in this thesis.

# References


[1] Lax, M., *Classical noise. V. Noise in self-sustained oscillators.* Physical Review, 1967. **160**(2): p. 290.

[2] Henry, C.H., *Theory of the linewidth of semiconductor lasers.* Quantum Electronics, IEEE Journal of, 1982. **18**(2): p. 259-264.

[3] Osiński, M. and J. Buus, *Linewidth broadening factor in semiconductor lasers--An overview.* Quantum Electronics, IEEE Journal of, 1987. **23**(1): p. 9-29.

[4] Henry, C.H., *Theory of the phase noise and power spectrum of a single mode injection laser.* Quantum Electronics, IEEE Journal of, 1983. **19**(9): p. 1391-1397.

[5] Tkach, R.W. and A.R. Chraplyvy, *Phase noise and linewidth in an InGaAsP DFB laser.* Lightwave Technology, Journal of, 1986. **4**(11): p. 1711-1716.

[6] Daino, B., et al., *Phase noise and spectral line shape in semiconductor lasers.* Quantum Electronics, IEEE Journal of, 1983. **19**(3): p. 266-270.

[7] Ahmed, M., M. Yamada, and M. Saito, *Numerical modeling of intensity and phase noise in semiconductor lasers.* Quantum Electronics, IEEE Journal of, 2001. **37**(12): p. 1600-1610.

[8] Vahala, K. and A. Yariv, *Semiclassical theory of noise in semiconductor lasers - Part I.* Quantum Electronics, IEEE Journal of, 1983. **19**(6): p. 1096-1101.

[9] Kikuchi, K., *Calculated field spectra of semiconductor lasers near threshold.* Electronics Letters, 1985. **21**(16): p. 705-706.

[10] Kikuchi, K. and T. Okoshi, *Measurement of FM noise, AM noise, and field spectra of 1.3 µm InGaAsP DFB lasers and determination of the linewidth enhancement factor.* Quantum Electronics, IEEE Journal of, 1985. **21**(11): p. 1814-1818.

[11] Schimpe, R., B. StegmÃ¿ller, and W. Harth, *FM noise of index-guided GaAlAs diode lasers.* Electronics Letters, 1984. **20**(5): p. 206-208.

[12] Schimpe, R. and W. Harth, *Theory of FM noise of single-mode injection lasers.* Electronics Letters, 1983. **19**(4): p. 136-137.

[13] Kobayashi, S. and T. Kimura, *Injection locking in AlGaAs semiconductor laser.* Quantum Electronics, IEEE Journal of, 1981. **17**(5): p. 681-689.

[14] Nilsson, O., S. Saito, and Y. Yamamoto, *Oscillation frequency, linewidth reduction and frequency modulation characteristics for a diode laser with external grating feedback.* Electronics Letters, 1981. **17**(17): p. 589-591.

[15] Goldberg, L., et al., *Spectral characteristics of semiconductor lasers with optical feedback.* Quantum Electronics, IEEE Journal of, 1982. **18**(4): p. 555-564.

[16] Patzak, E., et al., *Spectral linewidth reduction in semiconductor lasers by an external cavity with weak optical feedback.* Electronics Letters, 1983. **19**(22): p. 938-940.

[17] Harder, C., K. Vahala, and A. Yariv, *Measurement of the linewidth enhancement factor α of semiconductor lasers.* Applied Physics Letters, 1983. **42**(4): p. 328-330.

[18] Kikuchi, K. and T. Okoshi, *Estimation of linewidth enhancement factor of AlGaAs lasers by correlation measurement between FM and AM noises.* Quantum Electronics, IEEE Journal of, 1985. **21**(6): p. 669-673.

[19] Shin, G.H., M. Teshima, and M. Ohtsu, *Novel measurement method of linewidth enhancement factor in semiconductor lasers by optical self-locking.* Electronics Letters, 1989. **25**(1): p. 27-28.

[20] Hui, R., et al., *Novel measurement technique of alpha factor in DFB semiconductor lasers by injection locking.* Electronics Letters, 1990. **26**(14): p. 997-998.

[21] Liu, G., X. Jin, and S.L. Chuang, *Measurement of linewidth enhancement factor of semiconductor lasers using an injection-locking technique.* Photonics Technology Letters, IEEE, 2001. **13**(5): p. 430-432.

[22] Shin, Y.S., et al., *Simple methods for measuring the linewidth enhancement factor in external cavity laser diodes.* Optics communications, 2000. **173**(1): p. 303-309.
[23] Yu, Y., G. Giuliani, and S. Donati, *Measurement of the linewidth enhancement factor of semiconductor lasers based on the optical feedback self-mixing effect.* Photonics Technology Letters, IEEE, 2004. **16**(4): p. 990-992.
[24] Jiangtao, X., et al., *Estimating the parameters of semiconductor lasers based on weak optical feedback self-mixing interferometry.* Quantum Electronics, IEEE Journal of, 2005. **41**(8): p. 1058-1064.
[25] Yu, Y. and J. Xi, *Influence of external optical feedback on the alpha factor of semiconductor lasers.* Optics letters, 2013. **38**(11): p. 1781-1783.
[26] Toffano, Z., A. Destrez, and L. Hassine, *New linewidth enhancement determination method in semiconductor lasers based on spectrum analysis above and below threshold.* Electronics Letters, 1992. **28**(1): p. 9-11.
[27] Henry, C., R. Logan, and K. Bertness, *Spectral dependence of the change in refractive index due to carrier injection in GaAs lasers.* Journal of Applied Physics, 1981. **52**(7): p. 4457-4461.
[28] Henning, I.D. and J.V. Collins, *Measurements of the semiconductor laser linewidth broadening factor.* Electronics Letters, 1983. **19**(22): p. 927-929.
[29] Tessler, N., et al. *Temperature and output power dependence of carrier overflow and internal loss in InGaAs/InGaAsP multiple quantum well lasers*. in *Semiconductor Laser Conference, 1994., 14th IEEE International*. 1994.
[30] Agrawal, G.P., *Intensity dependence of the linewidth enhancement factor and its implications for semiconductor lasers.* Photonics Technology Letters, IEEE, 1989. **1**(8): p. 212-214.
[31] Bosch, T. and S. Donati, *Optical feedback interferometry for sensing application.* Optical engineering, 2001. **40**(1): p. 20-27.
[32] Bosch, T. *An Overview of Self-Mixing Sensing Applications*. in *Optoelectronic and Microelectronic Materials and Devices, 2004 Conference on*. 2004.
[33] Ozdemir, S.K., et al., *Self-mixing laser speckle velocimeter for blood flow measurement.* Instrumentation and Measurement, IEEE Transactions on, 2000. **49**(5): p. 1029-1035.
[34] Lodi, V. and S. Donati, *Injection modulation in coupled laser oscillators.* Quantum Electronics, IEEE Journal of, 1980. **16**(8): p. 859-864.
[35] Churnside, J.H., *Laser Doppler velocimetry by modulating a CO 2 laser with backscattered light.* Applied optics, 1984. **23**(1): p. 61-66.
[36] Miles, R.O., et al., *An external cavity diode laser sensor.* Lightwave Technology, Journal of, 1983. **1**(1): p. 81-93.
[37] Dandridge, A., R. Miles, and T. Giallorenzi, *Diode laser sensor.* Electronics Letters, 1980. **16**(25): p. 948-949.
[38] Takahashi, H., et al., *Laser diode interferometer for vibration and sound pressure measurements.* Instrumentation and Measurement, IEEE Transactions on, 1989. **38**(2): p. 584-587.
[39] de Groot, P.J., G.M. Gallatin, and S.H. Macomber, *Ranging and velocimetry signal generation in a backscatter-modulated laser diode.* Applied optics, 1988. **27**(21): p. 4475-4480.
[40] Lang, R. and K. Kobayashi, *External optical feedback effects on semiconductor injection laser properties.* Quantum Electronics, IEEE Journal of, 1980. **16**(3): p. 347-355.
[41] Servagent, N., F. Gouaux, and T. Bosch, *Measurements of displacement using the self-mixing interference in a laser diode.* Journal of optics, 1998. **29**(3): p. 168.
[42] Giuliani, G., et al., *Laser diode self-mixing technique for sensing applications.* Journal of Optics A: Pure and Applied Optics, 2002. **4**(6): p. S283.

[43] Yu, Y., et al. *Measuring multiple parameters in a self-mixing optical feedback system*. in *Optoelectronic and Microelectronic Materials and Devices, 2004 Conference on*. 2004. IEEE.

[44] Wang, M. and D.M. Guo. *Laser Diode Self-mixing Interference Based on Phase Measurement Method*. in *Key Engineering Materials*. 2008. Trans Tech Publ.

[45] Plantier, G., C. Bes, and T. Bosch, *Behavioral model of a self-mixing laser diode sensor.* Quantum Electronics, IEEE Journal of, 2005. **41**(9): p. 1157-1167.

[46] Yanguang, Y., et al., *Optical Feedback Self-Mixing Interferometry With a Large Feedback Factor C: Behavior Studies.* Quantum Electronics, IEEE Journal of, 2009. **45**(7): p. 840-848.

[47] Wang, W.M., et al., *Self-mixing interference inside a single-mode diode laser for optical sensing applications.* Lightwave Technology, Journal of, 1994. **12**(9): p. 1577-1587.

[48] Acket, G.A., et al., *The influence of feedback intensity on longitudinal mode properties and optical noise in index-guided semiconductor lasers.* Quantum Electronics, IEEE Journal of, 1984. **20**(10): p. 1163-1169.

[49] Yanguang, Y., et al., *Toward Automatic Measurement of the Linewidth-Enhancement Factor Using Optical Feedback Self-Mixing Interferometry With Weak Optical Feedback.* Quantum Electronics, IEEE Journal of, 2007. **43**(7): p. 527-534.

[50] Yu, Y., J. Xi, and J.F. Chicharo, *Measuring the feedback parameter of a semiconductor laser with external optical feedback.* Optics express, 2011. **19**(10): p. 9582-9593.

[51] Fan, Y., et al., *Improving the measurement performance for a self-mixing interferometry-based displacement sensing system.* Applied Optics, 2011. **50**(26): p. 5064-5072.

[52] Yu, Y., J. Xi, and J.F. Chicharo. *Improving the performance in an optical feedback self-mixing interferometry system using digital signal pre-processing*. in *Intelligent Signal Processing, 2007. WISP 2007. IEEE International Symposium on*. 2007. IEEE.

[53] Norgia, M., A. Magnani, and A. Pesatori, *High resolution self-mixing laser rangefinder.* Review of Scientific Instruments, 2012. **83**(4): p. 045113.

[54] Donati, S., G. Giuliani, and S. Merlo, *Laser diode feedback interferometer for measurement of displacements without ambiguity.* Quantum Electronics, IEEE Journal of, 1995. **31**(1): p. 113-119.

[55] Fan, Y., et al., *Dynamic stability analysis for a self-mixing interferometry system.* Optics express, 2014. **22**(23): p. 29260-29269.

[56] Fan, Y., et al. *Analysis on the transient of a self-mixing interferometry sensing system*. in *TENCON 2015-2015 IEEE Region 10 Conference*. 2015. IEEE.

[57] Teysseyre, R., et al., *Laser dynamics in sawtooth-like self-mixing signals.* Optics letters, 2012. **37**(18): p. 3771-3773.

[58] Shinohara, S., et al. *Compact optical sensor with a self-mixing laser diode for non-contact measurement of ultrasonic vibration*. in *Industrial Electronics Society, 2000. IECON 2000. 26th Annual Confjerence of the IEEE*. 2000. IEEE.

[59] Bes, C., G. Plantier, and T. Bosch, *Displacement measurements using a self-mixing laser diode under moderate feedback.* IEEE Transactions on Instrumentation and Measurement, 2006. **55**(4): p. 1101-1105.

[60] Norgia, M., G. Giuliani, and S. Donati, *Absolute distance measurement with improved accuracy using laser diode self-mixing interferometry in a closed loop.* Instrumentation and Measurement, IEEE Transactions on, 2007. **56**(5): p. 1894-1900.

[61] Ahmad, M.O. and D. Sundararajan, *A fast algorithm for two dimensional median filtering.* Circuits and Systems, IEEE Transactions on, 1987. **34**(11): p. 1364-1374.

[62] Yin, L., et al., *Weighted median filters: a tutorial.* Circuits and Systems II: Analog and Digital Signal Processing, IEEE Transactions on, 1996. **43**(3): p. 157-192.

[63] Gao, Y., et al., *Removing the impulsive noise contained in a self-mixing interferometry system using outlier detection.* Optical Engineering, 2014. **53**(12): p. 124108-124108.
[64] Gonzalez, J.G., D.L. Lau, and G.R. Arce. *Towards a general theory of robust nonlinear filtering: selection filters*. in *Acoustics, Speech, and Signal Processing, 1997. ICASSP-97., 1997 IEEE International Conference on*. 1997. IEEE.
[65] Kalluri, S. and G.R. Arce, *Adaptive weighted myriad filter algorithms for robust signal processing in α-stable noise environments.* Signal Processing, IEEE Transactions on, 1998. **46**(2): p. 322-334.
[66] Gonzalez, J.G. and G.R. Arce, *Optimality of the myriad filter in practical impulsive-noise environments.* Signal Processing, IEEE Transactions on, 2001. **49**(2): p. 438-441.
[67] Pitas, I. and A.N. Venetsanopoulos, *Nonlinear digital filters: principles and applications*. Vol. 84. 2013: Springer Science & Business Media.
[68] Arce, G.R., J.G. Gonzalez, and P. Zurbach. *Weighted myriad filters in imaging*. in *Signals, Systems and Computers, 1996. Conference Record of the Thirtieth Asilomar Conference on*. 1996. IEEE.
[69] Gonzalez, J.G. and G.R. Arce. *Weighted myriad filters: a robust filtering framework derived from alpha-stable distributions*. in *Acoustics, Speech, and Signal Processing, 1996. ICASSP-96. Conference Proceedings., 1996 IEEE International Conference on*. 1996. IEEE.
[70] Gonzalez, J.G. and G.R. Arce, *Statistically-efficient filtering in impulsive environments: weighted myriad filters.* EURASIP Journal on Advances in Signal Processing, 2002. **2002**(1): p. 1-17.
[71] Kalluri, S. and G.R. Arce, *Robust frequency-selective filtering using weighted myriad filters admitting real-valued weights.* Signal Processing, IEEE Transactions on, 2001. **49**(11): p. 2721-2733.
[72] Pander, T. *Impulsive Noise Filtering In Biomedical Signals With Application of New Myriad Filter*. in *Biosignal'2010: Proc. of the Int. Conf*. 2010.
[73] Kalluri, S. and G.R. Arce. *Adaptive algorithms for weighted myriad filter optimization*. in *Acoustics, Speech, and Signal Processing, 1997. ICASSP-97., 1997 IEEE International Conference on*. 1997. IEEE.
[74] Bernal, O.D., U. Zabit, and T. Bosch, *Study of laser feedback phase under self-mixing leading to improved phase unwrapping for vibration sensing.* Sensors Journal, IEEE, 2013. **13**(12): p. 4962-4971.
[75] Merlo, S. and S. Donati, *Reconstruction of displacement waveforms with a single-channel laser-diode feedback interferometer.* IEEE journal of quantum electronics, 1997. **33**(4): p. 527-531.
[76] Zabit, U., T. Bosch, and F. Bony, *Adaptive transition detection algorithm for a self-mixing displacement sensor.* Sensors Journal, IEEE, 2009. **9**(12): p. 1879-1886.
[77] Harris, F.J., *On the use of windows for harmonic analysis with the discrete Fourier transform.* Proceedings of the IEEE, 1978. **66**(1): p. 51-83.
[78] Brown, S. and J. Rose, *Architecture of FPGAs and CPLDs: A tutorial.* IEEE Design and Test of Computers, 1996. **13**(2): p. 42-57.
[79] Rose, J., A.E. Gamal, and A. Sangiovanni-Vincentelli, *Architecture of field-programmable gate arrays.* Proceedings of the IEEE, 1993. **81**(7): p. 1013-1029.
[80] Xilinx, *Xilinx DSP Design Flow Industry Course.* 2011.
[81] Xilinx, *Spartan-3E FPGA Starter Kit Board User Guide.* 2008.